OKINAWA INSTITUTE OF SCIENCE AND TECHNOLOGY
GRADUATE UNIVERSITY

Thesis submitted for the degree

Doctor of Philosophy

Fracton States of Matter: From Holography to Frustrated Magnetism

by

Han Yan

Supervisor: **Nic Shannon**
Co-Supervisor: **Sugawara Hirotaka**

21 April, 2020

Declaration of Original and Sole Authorship

I, Han Yan, declare that this thesis entitled *Fracton States of Matter: From Holography to Frustrated Magnetism* and the data presented in it are original and my own work.

I confirm that:

- No part of this work has previously been submitted for a degree at this or any other university.
- References to the work of others have been clearly acknowledged. Quotations from the work of others have been clearly indicated, and attributed to them.
- In cases where others have contributed to part of this work, such contribution has been clearly acknowledged and distinguished from my own work.
- None of this work has been previously published elsewhere, with the exception of the publications listed in the **Preprints and Publications** section.

Date: 21 April, 2020

Signature: 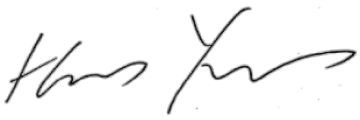

Abstract

The discipline of modern condensed matter physic has a lot ambitions: to discover all possible quantum phases of matter, to study the exotic properties and applications of different matter states, and to realize them in experiments. A recent exciting development in this field is the discovery of the fracton states of matter. Featuring immobile excitations and gauged/ungauged subsystem symmetries, it is a phase of quantum many-body systems that transcend the traditional scenarios of Landau-Ginsberg symmetry breaking and topological quantum states. This thesis is devoted to a few aspects of the fracton states of matter. First, we study a unique property of the fracton models: they mimic the quantum-informational features of gravity. This can be shown in the context of holographic principle or AdS/CFT duality: a fracton model in AdS space can be shown to satisfy the major properties of holography: the boundary entanglement entropy satisfies Ryu-Takayanagi formula, and the bulk reconstruction follows the Rindler reconstruction. Furthermore, the fracton model in hyperbolic space is known to be similar to various other toy models of holography including holographic tensor-networks and bit-threads model. The intriguing similarity between fracton models and gravity, as well as its implications, are discussed at length. In the second half of the thesis, we explore possible experimental routes to realize the fracton phases. Here we focus on frustrated magnets on the pyrochlore lattice, one of the most versatile and experimentally fruitful framework to realize spin liquids. By analyzing the symmetry and the coarse-grained limit of the model, we find it possible to realize various versions of rank-2 U(1) gauge theory, and some of them are simple enough to be experimentally realistic. We also propose ways to introduce quantum dynamics via frustration of higher spins.

Acknowledgment

First and foremost, I am enormously indebted to my supervisor Nic Shannon and co-supervisor Hirotaka Sugawara for their great mentorship. Nic has always been tremendously resourceful, kind, and supportive to me. Besides proposing exciting scientific ideas and providing very helpful guidance in condensed matter theory, he also encourages me to be independent and develop my own ideas. More importantly, he shows me a great example of how to be a decent, principled person.

Likewise, Hirotaka has always been the most supportive, and also knowledgeable when it comes to high energy theory. I enjoyed the luxury to have two supervisors covering both condensed matter physics and high energy physics. Owing to them, over my doctoral course I could enjoy the so much beauty of physics – both amazements of fundamental theory regarding quantum gravity and elementary particles, as well as the wonders of "emergence" in quantum many-body systems.

I am sincerely thankful to my collaborators: Ludovic Jaubert, Owen Benton, Mathieu Taillefumier, Romian Sibille, Judit Romhanyi, Rico Pohle, Ke Liu, Andreas Thomasen. With them I had a lot fun doing research, and also learned so much physics. In particular, the numerical simulation results in Chapter 4 and 5 are obtained by Ludovic, and some of the analysis in Chapter 4 is done in collaboration with Owen. I am also very thankful to Leilee Chojnacki, who helped me checking the English of the thesis. I also appreciate daily interactions with other people in our unit and university: Yasha Neiman, Karlo Penc, Yutaka Akagi, Karim Essafi, Olga Sikora, Hiroaki Ueda, Yurika Kubo, Christina Lee, Andrew Smerald, Matthias Gohlke, Geet Rakala, Tokuro Shimokawa, Soshi Mizutani, and Kimberly Remund. Also, I want to express my thanks to our reserach unit assistants Megumi Ikeda and Shiho Saito, whose effectiveness and sweetness have made all our research lives infinitely easier. They are not only colleagues but also friends I hold dearly in life.

Last but not least, I want to thank my family for always supporting me to chase my passion, and thank Maéva Techer for her love and support.

Acknowledge to institutions

This work in funded by Theory of Quantum Matter Unit at Okinawa Institute of Science and Technology, and the Japan Society for the Promotion of Science (JSPS) Research Fellowships for Young Scientists.

Preprints and Publications

Preprints

Geodesic string condensation from symmetric tensor gauge theory: a unifying framework of holographic toy models, arXiv:1911.01007, **Han Yan**

How many spin liquids are there in $Ca_{10}Cr_7O_{28}$? arXiv:1711.03778, Rico Pohle, **Han Yan**, Nic Shannon

Publications

Rank-2 U(1) spin liquid on the breathing pyrochlore lattice, Physical Review Letters 124, 127203 (2020) **Han Yan**, Owen Benton, Ludovic D.C. Jaubert, Nic Shannon
※Highlighted as Editors' selection, and by APS Physics Magazine article "Synopsis: A Recipe for Finding Fractons" (Physics 13, s40).

Identification of hidden order and emergent constraints in frustrated magnets using tensorial kernel methods, Physical Review B 100, 174408 (2019) Jonas Greitemann, Ke Liu, Ludovic DC Jaubert, **Han Yan**, Nic Shannon, Lode Pollet
※Featured on OIST news "Man versus machine: can AI do science?"

Hyperbolic fracton model, subsystem symmetry, and holography II: the dual eight-vertex model, Physical Review B 100, 245138 (2019) **Han Yan**

Hyperbolic fracton model, subsystem symmetry, and holography, Physical Review B 99, 155126 (2018), **Han Yan**
※Highlighted as Editors' selection, and featured on OIST news "Theories Past and Present Show Quantum Connections"

Half moons are pinch points with dispersion, Physical Review B Rapid Communication 98, 140402(R), **Han Yan**, Rico Pohle, Nic Shannon
※Highlighted as Editors' selection, and featured on OIST news "Half Moons and Pinch Points: Same Physics, Different Energy"

Experimental signatures of emergent quantum electrodynamics in $Pr_2Hf_2O_7$, Nature Physics

14, 711(2018), Romain Sibille, Nicolas Gauthier, **Han Yan**, Monica Ciomaga Hatnean, Jacques Ollivier, Barry Winn, Geetha Balakrishnan, Michel Kenzelmann, Nic Shannon, Tom Fennell
※Featured on OIST news "Seeing the Light? Study Illuminates How Quantum Magnets Mimic Light"

Competing Spin Liquids and Hidden Spin-Nematic Order in Spin Ice with Frustrated Transverse Exchange, Physical Review X 7, 041057 (2017), Mathieu Taillefumier, Owen Benton, **Han Yan**, Ludovic D. C. Jaubert, Nic Shannon

Theory of multiple–phase competition in pyrochlore magnets with anisotropic exchange, with application to $Yb_2Ti_2O_7$, $Er_2Ti_2O_7$ and $Er_2Sn_2O_7$, Physical Review B 95, 094422 (2017), **Han Yan**, Owen Benton, Ludovic D. C. Jaubert, Nic Shannon

From pinch points to pinch lines: a new spin liquid on the pyrochlore lattice, Nature Communications 7, 11572 (2016), Owen Benton, Ludovic D. C. Jaubert, **Han Yan** and Nic Shannon
※Featured on OIST news "A New Spin on Reality"

Articles

Neutron scattering signatures of a quantum spin ice, Swiss Neutron News 53, 12-22 (2019), arXiv:1911.00968, Romain Sibille, Nicolas Gauthier, **Han Yan**, Monica Ciomaga Hatnean, Jacques Ollivier, Barry Winn, Geetha Balakrishnan, Michel Kenzelmann, Nic Shannon, Tom Fennell

Contents

1 Introduction **1**

1.1 The quests of this thesis 3

1.2 Brief review of the AdS/CFT correspondence 5

1.3 Spin liquid and emergent U(1) gauge theory 8

1.4 Rank–2 U(1) gauge theory 13

1.5 Outline of the thesis 19

2 Hyperbolic Fracton Model and Holography **21**

2.1 Introduction 22

2.2 Summary of the main results 23

2.3 Fracton model on the Euclidean lattice 24

2.4 The Hyperbolic Fracton Model 30

2.5 Rindler Reconstruction of the Hyperbolic fracton model 34

2.6 Mutual information of the hyperbolic fracton model 36

2.7 Naive black holes in the hyperbolic fracton model 42

2.8 Generalizations: higher dimension and quantum version 43

2.9 Comparison with the holographic tensor-networks 46

2.10 Outlook 47

3 The Dual Eight-Vertex Model and Bit Threads **49**

3.1 Introduction 49

3.2 Dual Eight Vertex Model on the Square Lattice 50

3.3 Connection to rank-2 U(1) theory 53

3.4 Hyperbolic Dual Eight-Vertex Model 54

3.5 Bit-Thread Realization 55

3.6 Bulk-Boundary Isometry for Diluted Fracton Excitations 58

3.7 Non-Local Black Hole Microstate Degree of Freedom 61

3.8 Outlook 63

4 Unifying holographic toy models with rank-2 U(1) field theory **65**

4.1 Bit-thread type holographic toy models as a universal picture 66

4.2 Rank-2 U(1) Theory and Its Flat-Space Dynamics 68

4.3 Entanglement structure from Gauge symmetry: conventional U(1) as an example 69

4.4 Entanglement structure of R2-U1 in AdS space: geodesic string condensation 71

4.5 The case of scalar charged R2-U1 73

4.6 Discussion 74

5 Pyrochlore Spin System **77**

5.1 Introduction 77

5.2 The pyrochlore lattice spin model with anisotropic exchange 80

5.3 Analysis of the classical phase diagram at T=0 89

5.4 Application to materials 107

5.5 Conclusion 108

6 Rank-2 U(1) spin liquid on breathing pyrochlore lattice **111**

6.1 Introduction 111

6.2 Rank–2 U(1) gauge theory 113

6.3 Rank 2 U(1) Gauss's law on the breathing pyrochlore model 115

6.4 Experimental signatures 121

6.5 Application to materials. 127

6.6 Summary 128

7 Conclusion and Outlook **131**

7.1 Fracton states of matter and holography 131

7.2 Experimental Routes toward fracton states of matter 132

List of Figures

1.1 Anatomy of anti-de Sitter (AdS) spacetime 6

1.2 Ryu-Takayanagi (RT) formula of entanglement entropy and Rindler reconstruction 7

1.3 Different lattices with geometric frustration. 9

1.4 Spin ice configurations. 10

1.5 Spin ice charge excitations. 11

1.6 Vector-charge dipole (or quadrupole) operators. 17

2.1 The fracton model on the Euclidean lattice 25

2.2 Ground states for the fracton model on the Euclidean lattice. 26

2.3 Fracton excitations and their bound states 27

2.4 Speculated connections between fracton model and holography 28

2.5 Hyperbolic lattice for the fracton model 32

2.6 The ground states and fracton excitations in the hyperbolic fracton model 33

2.7 Rindler reconstruction of the hyperbolic fracton model 35

2.8 Counting the entropy of a subsystem 38

2.9 Mutual information as a classical analog of entanglement entropy obeys the Ryu-Takayanagi formula 40

2.10 Possible configurations for disconnected boundary subregion 41

2.11 A naive black hole in the hyperbolic fracton model 42

2.12 Building block of 3D classical fracton model 44

2.13 Subsystem symmetry of the fracton model in AdS_3 space. 45

2.14 An example of subregions A, B with non-vanishing mutual information 47

3.1 Vertex configurations in eight-vertex model. 51

3.2 Mapping between the spin configurations and the vertices. 51

3.3 Ground state degeneracy in the two dual models. 52

3.4 Dual eight-vertex model on the hyperbolic disk at $T = 0$. 55

3.5 Bit-Thread Realization and Ryu-Takayanagi formula for mutual information. 56

3.6 An example of RT-formula violation of the mutual information. 57

3.7 Two examples of isometry violation. 59

3.8 Examples of isometry at finite energy. 60

3.9 A black hole in the hyperbolic fracton model. 61

3.10 Black hole microstate information for observer covering a subregion of the boundary. 63

4.1 Universal picture of holographic toy models 66

4.2 The operator B of rank-2 U(1) theory in the flat space 71

4.3 Different quadrupoles. (a) Quadrupole with non-vanishing value of $\int dv\rho x^2$ and forbidden in the traceless scalar-charged R2-U1. (b) Quadrupole with vanishing value of $\int dv\rho x^2$ and allowed in the traceless scalar-charged R2-U1. 74

5.1 Pyrochlore lattice 78

5.2 Labeling of sub-lattice sites on a tetrahedron. 81

5.3 The "Lego–brick" rules describing how the ground states of a single tetrahedron can be connected to tile the pyrochlore lattice. 88

5.4 Classical ground state phase diagram in the absence of fluctuations. . . . 92

5.5 Classical ground-state phase diagram including fluctuation. 93

5.6 Finite-temperature phase diagram for a pyrochlore magnet with anisotropic exchange interactions. 94

5.7 Spin-configuration in the 4-sublattice non-collinear FM phase 96

5.8 Example of a spin configuration within the one–dimensional manifold of states transforming with the E irrep of T_d. 97

5.9 Spin configuration in the 4-sublattice non-coplanar antiferromagnet Ψ_2. 98

5.10 Spin configuration in the 4-sublattice coplanar antiferromagnet Ψ_3. . . . 100

5.11 Spin configuration in the 4-sublattice Palmer–Chalker phase Ψ_4. 101

5.12 Structure of the ground state manifold at the boundary. 102

6.1 Breathing pyrochlore lattice. 116

6.2 Structure of the 4–fold pinch point associated with rank–2 U(1) gauge theory. 123

6.3 Analytical resutls of correlation function $\langle E_{ij}(\mathbf{q})E_{kl}(-\mathbf{q})\rangle$ 123

6.4 Monte-Carlo resutls of correlation function $\langle E_{xy}(\mathbf{q})E_{xy}(-\mathbf{q})\rangle$ 124

6.5 4-Fold Pinch Points in spin structure factor 125

6.6 Finite–temperature phase diagram of breathing pyrochlore lattice model. 127

6.7 Spin structure factor found in classical Monte Carlo simulation 128

List of Tables

4.1 Comparison of the holographic entanglement properties. 67

4.2 From gauge symmetry to the entanglement structure. 70

5.1 Relationship between the parameters of the anisotropic nearest–neighbour exchange model in the local coordinate frame. 84

5.2 Order parameters $\mathbf{m}_\lambda$ in global coordinate frame. 89

5.3 Order parameters $\mathbf{m}_\lambda$ in local coordinate frame. 91

5.4 Coefficients a_λ of the scalar invariants $|\mathbf{m}_\lambda|^2$. 93

5.5 Estimates of the parameters for anisotropic near-neighbour exchange, taken from experiments. 107

Chapter 1

Introduction

Teaser

In childhood, we have all struggled with problems of Euclidean geometry. The five axioms of Euclidean geometry, stated in Euclid's renowned masterpiece *Elements*, were formulated around 300 BC. In principle, all the knowledge of Euclidean geometry is already contained in these five axioms. Nothing more needs to be said. Yet more than two thousand years later, there are still so many perplexing results reaching far beyond our intuition.

Quantum physics is very similar to Euclidean geometry in this sense. The axioms of quantum physics are very simple: the state of a quantum system is defined by a vector in a complex Hilbert space, evolves unitarily in a closed system, has observables as Hermitian operators, and overlap with other state vector by their scalar product. Were we god-like existence, blessed with infinite intelligence and computational power, we would have already known everything about quantum physics. However, the implications behind such simple axioms are so vast and profound, that even until now, we, mortal and flawed, cannot comprehend some of its most relevant aspects.

We have certainly triumphed in relativistic theory of point-like particles — the quantum field theory. The pinnacle of this discipline is the construction and experimental test of the Standard Model. The technique of second quantization has also made great contribution of condensed matter physics.

However, when perturbative theory fails, we are often in trouble. There are many aspects of quantum physics that are not fully understood.

Quantum gravity — The quantum field theory of gravitons suffers problem of renomrlization. That is, the field theory will generate infinite terms as the energy scale increases. As a consequence, we cannot write down a sensible action for the gravitons at the UV limit [1]. More fundamentally, the following argument convinces us quantum gravity is out of the scope of conventional quantum field theory.

Consider a subspace of a fixed volume in space. If it is a field theory living in the spacetime, then the degrees of freedom of the subspace is proportional to its volume (with proper UV regularization to cut off the singularities), as on each point live some degrees of freedom. For a well-defined, renormalizable quantum field theory, this is true up to arbitrary energy scale.

But if it is a gravitational system, as we examine the higher energy states, it is not the case. Because higher energy means higher mass, eventually the subsystem becomes a black hole, whose entropy is proportional to the horizon area, instead of its volume. That is, a conventional quantum field theory is inconsistent with our knowledge of gravity, because it drastically fails to capture the gravitational effects at high energy. In a quantum gravitational system, there are many fewer degrees of freedom than that that in a quantum field theory.

In the last two decades, the seminal works of holographic principle and anti-de Sitter/conformal field theory correspondence (AdS/CFT) have offered us great hope to understand this issue [2–11]. The conjecture states that a gravitational theory describing a region of space is equivalent to a non-gravitational theory living on its boundary. If such conjecture is true, then we in principle have a quantum version of gravity and can compute many things.

Intriguingly, some toy models based on tensor-networks [12–18] and bit-threads [19–21] satisfy many of the major properties of AdS/CFT [22, 23]. Though built upon very simple elements, they exhibit entanglement structure that look sufficiently similar to that of gravity.

It is thus an interesting quest to seek for a more universal understanding of such toy models, and clarify their connection to gravity.

Quantum many-body systems — In the discipline of condensed matter physics, one of the major themes is to understand phases of matter and their associated physical properties. Traditionally, the classical states of matter are unified under the framework of symmetry-breaking. The systematic mechanism of Landau-Ginsburg symmetry analysis can take care of most problems of phase transitions, except those with topological features [24].

However, quantum many-body systems are a completely different story. Given a system, the number of quantum states is exponentially larger than the number of the classical ones (product states). Hence, the landscape of new phases is vast and extends far beyond that of the classical scenario.

There are a lot we can ask. For example, what kind of ground states are genuinely different from a classical product state? This question can be answered by using the concept of local unitary transformation (LU) [25]. Some quantum states, though are not product states and involve some short range entanglement, can be transformed into a product state via LU. Hence they are not too different from a classical state. From the point of view of renormalization, as we "zoom out" of the system, the short

range entanglements effectively disappear and we end up with a number of product states at the coarse-grained level. However, some ground states involve long-range entanglement or topological entanglement, which cannot be removed by LU. Hence they will never be transformed into a classical product state.

They are the genuinely new phases of matter introduced by quantum effects. Later, we will introduce the spin ice model, which is an example of such quantum phase. Such topological orders are normally described by effective gauge theories. They are in particular sensitive to the topology of the lattice, hence named topological order.

The symmetry-breaking and topological-order scenarios have been the fundamental ideas to understand quantum phases of matter. However, recently a new class of matters dubbed "fracton topological orders" was discovered and studied intensively in the past few years [26–34]. It is in neither of the two above scenarios, hence attracts great interests, and also presents challenges on how to understand it in terms of field theory.

1.1 The quests of this thesis

In this thesis, we would like to discuss an interdisciplinary topic between quantum gravity and condensed matter physics: what kind of many-body system has emergent gravitational behaviors, and what are the possible routes to realize them in experiments?

The fracton states of matter [26, 29, 30] play a central role in this topic. As a state of matter with exotic excitations and low energy effective descriptions, they have been studied intensively in the past few years, in the context of quantum information and condensed matter physics. A few earlier works and also more recent examinations [32, 33, 35–37] show that the photonic sector of the gapless fracton states has a similar gauge structure to that of linearized diffeomorphism. The fracton charge excitations also have effectively attractive forces [35].

Motivated by these results, we would like to explore a different aspect of fracton—gravity similarities: their quantum informational properties, in particular, their entanglement structures.

Besides the highly theoretical investigations, it is also a meaningful inquiry to look for realistic approach to realize the fracton states. As a theory of spin liquids, one of the most likely mechanism to realize the fracton states is frustrated magnetism. This will be the second topic of this thesis.

To summarize, we are motivated to answer the following two questions:

I. How does fracton states of matter mimics the entanglement structure of gravity?

II. How can we realize it in a experimentally realistic frustrated magnet model?

Let us define the two quests clearer.

Quest I: It is well-established that many gauge theories "emerge" as collective phenomena in many-body systems, and dictate their topological features at low energy. However, less is known about how many-body systems can mimic gravity, except for some works building emergent gauge bosons that mimic gravitons.

The developments in holography and AdS/CFT [2–5] have taught us that there is another profound side of gravity: its quantum-informational properties [22, 23]. As practitioners of the idea "emergence", it is natural for us to ask: what kind of many-body systems captures the informational aspects of gravity?

In this thesis, I will show that the fracton states in the AdS space satisfy a few major informational properties of gravity in the context of holography. These properties include the bulk geometric correspondence to the boundary entanglement (Ryu-Takayanagi formula) [22, 23], the boundary-bulk reconstruction pattern (Rindler reconstuction), and the microstate encoding of black holes.

A major advance following these works is a unifying framework of different bit-thread/tensor-network type holographic toy models [13, 14, 16, 17]. The discovery of fraction toy models provide a bulk theory for these toy models: the Lifshitz gravity or rank-2 U(1) gauge theory. Such special version of gravity illuminates both the strength of the toy models as well as what they fail to capture. Another exciting possibility is to design experiments of fracton states on hyperbolic surface, as laboratory realizations of holography.

Quest II: On the condensed matter theory front, my focus is on realizing the effective gauge structure of fracton states in frustrated spin systems.

The frustrated spin system is a great playground to realize the exotic spin liquid states, which are often lattice versions of gauge theories [38–41].

In a series of works, my collaborators and I have developed a powerful tool-set to identify the underlying Gauss's law and gauge structure in pyrochlore spin systems. It leads to the discovery of several spin liquids with exotic gauge structures including double U(1) and matrix tensor gauge. The mechanism of gauge-symmetry breaking and restoring between these different phases is also well understood. These efforts reveal an exciting landscape of designable exotic spin liquids, both as intriguing theoretical models and as experimental guidelines.

The tool-set allows us to reverse engineer the problem: from the desired gauge structure, namely rank-2 U(1), one can find out the proper Hamiltonian to realize it. Very fortunately, the interactions required are very simple, thus giving a lot hope for it to be realized in experiments.

The rest of the introduction will briefly introduce the theoretical tools we rely on. First, we will review the concept of AdS/CFT, especially the informational properties derived from it: the Ryu-Takayanagi formula for entanglement entropy, the AdS-Rindler reconstruction etc. The comparison of fracton states and gravity will be done in the context of holography, so these properties will be heavily used.

Then we will introduce the frustrated magnetism, and introduce its canonical example: spin ice. It is one of the simplest cases of emergent U(1) gauge structure, with both in-depth theoretical understanding as well as a few experimental realizations and candidates. This will prepare us for the final introduction of the more complicated rank-2 U(1) classical spin liquid as a fracton state.

1.2 Brief review of the AdS/CFT correspondence

The holographic principle states that a gravitational theory describing a region of space is equivalent to a non-gravitational theory living on its boundary. For readers unfamiliar with holography, we present a brief summary of the essential results relevant to this work. More thorough introductions can be found in Ref.[42–45].

1.2.1 Black hole information paradox

This profound principle was firstly motivated by the black hole entropy. As a purely classical, exact solution to Einstein's equations of general relativity, a black hole should have zero entropy. However, this violates the second law of thermodynamics, since we lose information on whatever objects pass the horizon when falling into the black hole. This is partially resolved by the Bekenstein-Hawking black hole entropy [46, 47], which states that a black hole actually has entropy proportional to the area of its horizon

$$S_{BH} = \frac{A}{4G_N}\,, \tag{1.1}$$

where A is the horizon area, and G_N is the Newtonian constant. The entropy can be interpreted as counting the microstates of a black hole. Hence Eq. (1.1) indicates that the number of degrees of freedom for a black hole is proportional to its horizon area, instead of its volume, as in conventional quantum field theories. This echoes the holographic principle, which states that the degrees of freedom are living on the boundary instead of in the bulk.

1.2.2 AdS/CFT Correspondence

The AdS/CFT correspondence is a more concrete realization of holography. It is a duality between a gravitational theory in $d+1-$dimensional AdS space and $d-$dimensional

CFT on its boundary.

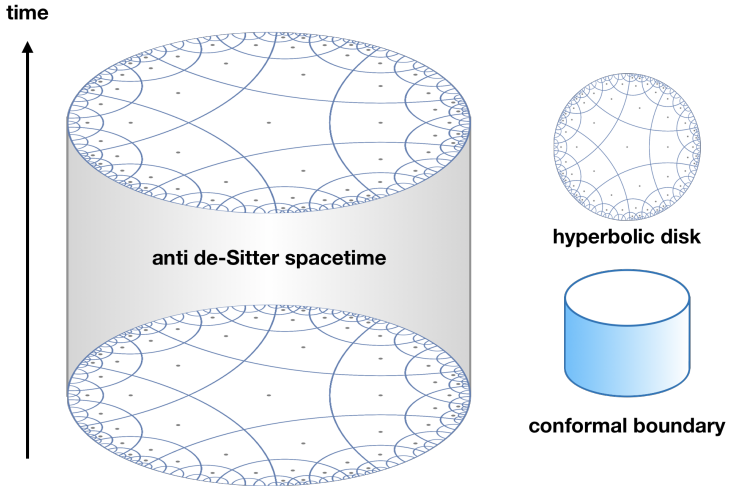

Figure 1.1: Anatomy of anti-de Sitter (AdS) spacetime. It can be viewed as a stack of constant-negative-curvature spatial slices in temporal direction. Each slice here is a hyperbolic disk. Note that the temporal direction is not simply straight upward. The boundary of the AdS spacetime, as shown on the bottom right panel, is where a conformal field theory (CFT) lives. Figure reproduced from Ref. [48].

An AdS space is a space with constant negative curvature, equipped with the metric

$$ds^2 = \frac{R^2}{u^2}(-dt^2 + d\vec{x}^2 + du^2) \,, \tag{1.2}$$

which can be seen as AdS spatial slices stacked in the temporal direction. In Fig. 1.1, an AdS_3 space is illustrated as a stack of hyperbolic disks.

The first example of AdS/CFT proposed by Maddalena is the duality between type-IIB superstring theory in the bulk of $\mathrm{AdS}_5 \times \mathrm{S}_5$ and large-N $\mathcal{N} = 4$ super-Yang-Mills theory on the boundary [4]. It suggests that there should be no information loss with black holes in a gravitational system, since it is equivalent to some non-gravitational quantum physics in which information is preserved.

1.2.3 Ryu-Takayanagi Formula

The Ryu-Takayanagi formula reveals the deep connection between the geometry of the AdS spacetime and the entanglement of the boundary CFT states. Assuming that the CFT lives on the boundary of some asymptotic AdS space, for a region A on that boundary, there exists a corresponding minimal codimension-one surface γ_A such that (1)it is homologous to A in the asymptotic AdS bulk; i.e., its boundary coincides with the boundary of A, or $\partial\gamma_A = \partial A$; (2) its area is extremal (in our case minimal) among all surfaces satisfying (1). The union of A and γ_A encloses a volume denoted the *entanglement wedge* $W(A)$. The Ryu-Takayanagi formula indicates that the entanglement

entropy S_A of the CFT states between A and its complement A^c is proportional to the area of γ_A, ignoring higher-order bulk contributions [22, 23]:

$$S_A = \frac{\text{Area}(\gamma_A)}{4G_N} \,. \tag{1.3}$$

This is illustrated in Fig. 1.2a.

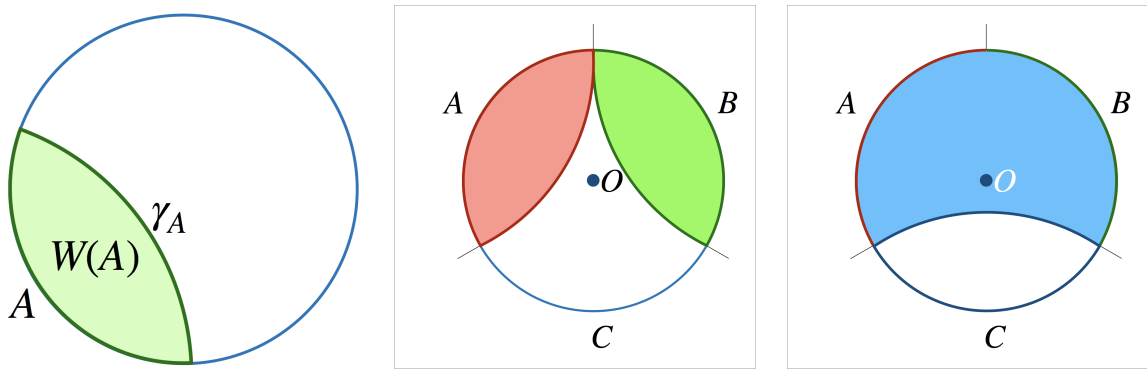

(a) RT formula **(b)** Rindler reconstruction **(c)** Another example of rindler reconstruction

Figure 1.2: Ryu-Takayanagi (RT) formula of entanglement entropy and Rindler reconstruction. (a) RT formula for entanglement entropy. The boundary subregion A and its complement A_c's entanglement entropy is proportional to the area of γ_A, the minimal surface in the bulk covering A. Given boundary states on A, bulk operators in the entanglement wedge $W(A)$ (shaded volume) can be reconstructed. (b),(c) An example of Rindler reconstruction. The bulk operator $\mathcal{O}$ cannot be reconstructed by boundary region A, B, or C individually as it lies outside each individual entanglement wedge (shaded volumes). However, it is included in the entanglement wedge of $A \bigcup B$, and can be reconstructed when the boundary states on both A and B are known. Figure reproduced from Ref. [48].

1.2.4 Subregion Duality and Rindler Reconstruction

Since AdS/CFT is a duality between the boundary and the bulk physics, it is crucial to understand how much boundary information is needed to reconstruct a bulk state or operator, and how the state is reconstructed. It is a subtle issue in the presence of temporal direction, which we do not intend to discuss. Fortunately, we only work on a spatial slice of the AdS_3 spacetime like most of the tensor-network models, when the laws of bulk reconstruction are significantly simplified: The bulk state can be constructed from a boundary segment A if and only if it is within the entanglement wedge $W(A)$, as shown in Fig. 1.2.

A good exercise to teach us about the non-trivial entanglement is to examine the tripartition A, B, C of the boundary and a bulk operator $\mathcal{O}$ at the center of the hyperbolic disk (Figs. 1.2b, 1.2c.). The entanglement wedge of any single one of regions A, B, or C

does not include the bulk site, meaning $\mathcal{O}$ cannot be reconstructed from these boundary states . However, the union of any two boundary segments has an entanglement wedge that covers $\mathcal{O}$, so given states on two of the three boundary segments, $\mathcal{O}$ can be reconstructed.

This example indicates the highly nontrivial entanglement structure of the boundary states. It is captured by the quantum error correction code [13]. and realized in the perfect tensor networks and random tensor-networks [14, 17].

1.3 Spin liquid and emergent U(1) gauge theory

Now let us switch from heaven to (rare)earth and discuss more experimentally oriented physics. In this section we will briefly explain what are quantum spin liquids and why are they interesting states of matter. We introduce the concept of frustrated magnetism – a promising mechanism to realize quantum spin liquids. We will then use classical and quantum spin ice as examples to show concretely how frustrated magnetism works.

Quantum spin liquid — Traditionally, the phases of matter are characterized by symmetry-breaking and long-range order as developed by Ginzburg and Landau [49]. However, in quantum many-body systems, quantum phases beyond such paradigm can occur.

They generally fall into the broad category of topological states of matter [25, 50], and feature stability against perturbation, exotic excitations (anyons etc.), and long-range entanglement. They are of tremendous interest for both theoretical understanding of nature as well as potential applications in quantum information [51].

Quantum spin liquids provide examples of topological states of matter. The first spin liquid was proposed by Anderson in 1973 [38], under the name "resonating valence bond" (RVB) state.

Nowadays, quantum spin liquids are usually considered quantum many-spin systems, in which zero-point quantum fluctuations play a non-trivial role of driving the system into a "quantum disordered" ground states even at zero temperature.

In particular, the spin liquids feature fractionalized excitations, and they can have non-trivial commutation relation due to the quantum entanglement. Such fractionalized excitations cannot be described within the framework of Landau-Ginsburg.

Like many examples of topological states of matter, quantum spin liquids are disordered in the eyes of local probes, but non-locally they have certain form of topological order not characterizable by symmetry,

The quantum spin liquid states also have massive many-body entanglement that dis-

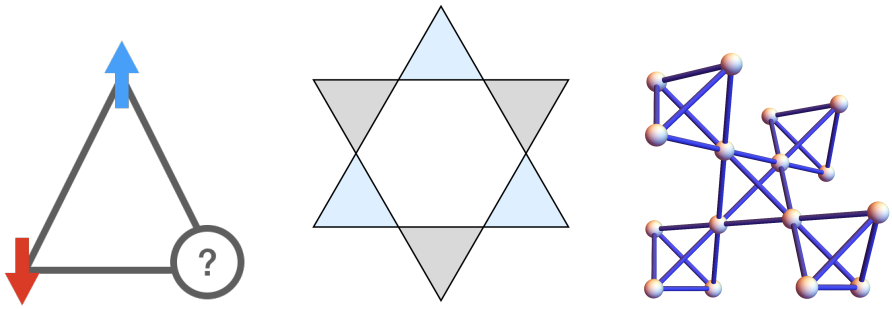

(a) Triangular lattice **(b)** Kagome lattice **(c)** Pyrochlore lattice

Figure 1.3: Different lattices with geometric frustration.

tinguish them from the more "classical" states of matter. The entanglement come from the superposition of extensively many states in the product state basis. These features make them highly interesting both theoretically and experimentally.

Frustrated magnetism — One exciting aspect about quantum spin liquids is that there is a experimental route toward their realization: frustrated magnetism [38, 39]. In this thesis we refer to geometric frustration exclusively.

Geometric frustration is a mechanism that the spin interactions on different bonds on the lattice cannot reach the minimal energy simultaneously due to limitations of the spin arrangements. The simplest example is a triangle with anti-ferromagnetic (AFM) interactions between Ising spins on its corners. As shown in Fig. 1.3a, we can minimize one bond by having an up-spin and a down-spin on two corners. But no matter the third spin is pointing up or down, one of its two bonds must have higher energy, hence "frustrated". So to minimize the total Hamiltonian, any spin configuration of two-up-one-down or two-down-one-up is sufficient, and there are six degenerate ground states.

Frustrated magnetism can happen on different lattices. In 2D, both the triangular and Kagome lattice AFMs (cf. Fig. 1.3) are frustrated lattices composed of the frustrated triangles, and have gone through intensive studies.

In 3D, the arguably most well-known playground for frustrated magnetism is the pyrochlore lattice (cf. Fig. 1.3c). It is composed of a network of corner-sharing tetrahera. The tetrahedra, having four faces of triangles, is a source of high amount of frustration. The name pyrochlore, meaning "fire green" in Greek, comes from the naturally formed mineral $(Na,Ca)_2Nb_2O_6(OH,F)$. The mineral turns green upon ignition.

The materials relevant to spin liquids on pyrochlore lattice normally have chemical formula $A_2B_2O_7$ [52–60].

Classical spin ice — The model of AFM interactions between Ising spins on a py-

rochlore lattice

$$\mathcal{H}_{\mathrm{SI}} = J_{zz} \sum_{i,j} S_i^z S_j^z, \tag{1.4}$$

is called classical spin ice [7, 52–70]. It is *not* a quantum spin liquid yet, since the system is classical. It should be classified as "collective paramagnets" or classical spin liquids as we will see the reason soon. But to understand it will be the first step to understand the quantum spin ice, which is a canonical example of quantum spin liquid.

Before we start, we should clarify the terminology a bit. Quantum/classical spin ice is a quantum/classical spin liquid. For readers unfamiliar with this discipline, it is a bit confusing how "ice" is a "liquid". In the former term, the word "ice" refers to the fact that its geometric structure is very similar to that of water ice locally – the protons in water ice form a lattice as different network of tetrahedra. In the later term, the word "liquid" refers to the fact that in such a state of matter, the spins are never ordered, just as molecules in a liquid never freeze to a fixed lattice. Quantum spin ice is a type of quantum spin liquid, whose lattice geometric structure is same to water ice locally.

Now, let us examine the anti-ferromagnetically coupled Ising spins on the corners of a tetrahedron, as shown in Fig. 1.4. Here, the Ising spins are aligned on the local [111]-axis, pointing in the direction from the center of the tetrahedron to the corner or in the opposite direction. For each single tetrahedron, any two-in-two-out spin configuration minimizes the total Hamiltonian, and there are six of such spin configurations [Fig. 1.4].

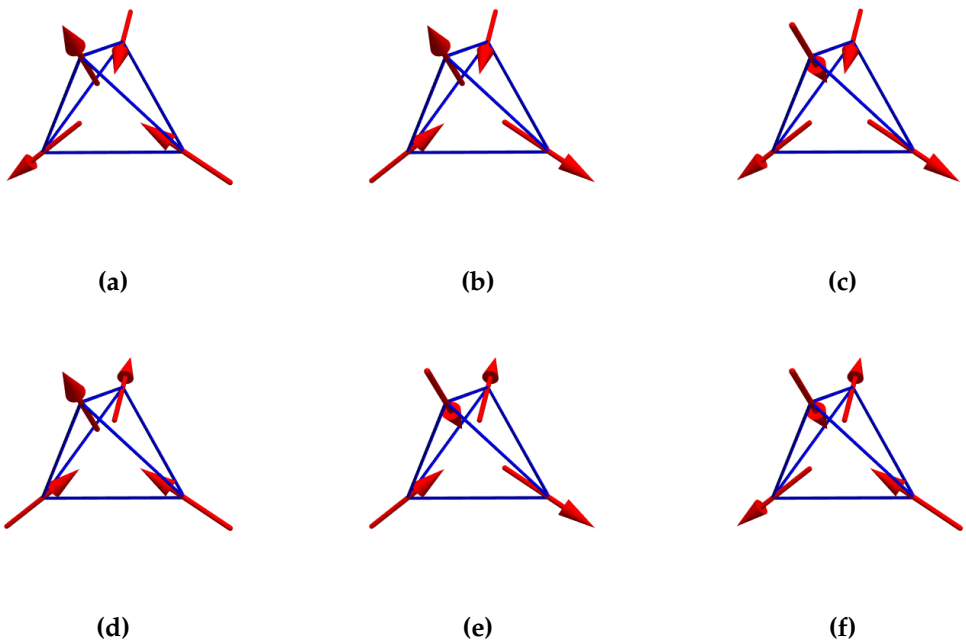

Figure 1.4: Spin ice ground state configurations (two-in-two-out) on a single tetrahedron. Each tetrahedron has six such degenerate ground states.

In a macroscopic system of pyrochlore lattice, the degeneracy is extensive. Such de-

generacy structure precisely maps to the how the protons disorder (located close/far to the oxygen ion) in water ice, hence was dubbed "spin ice". Spin ice has ground state degeneracy proportional to its volume [71]

$$S = \frac{Nk_B}{2} \log(\frac{3}{2}). \tag{1.5}$$

The two-in-two-our rule is essentially the Gauss's law of the classical spin ice system at a coarse-grained level,

$$\nabla \cdot \mathbf{E} = 0, \tag{1.6}$$

if we view each spin as a small vector electric filed. Equivalently, one can treat the spins as magnetic field and switch the notations accordingly, but the physics is description-invariant.

Taking entropy into account, the effective free energy at finite temperature [72] is

$$\mathcal{F}_{\text{CSI}} = \frac{\epsilon}{2}\mathbf{E}^2 + U(\nabla \cdot \mathbf{E})^2, \tag{1.7}$$

where the first term come from entropic contribution, i.e., the average of $\mathbf{E}$ over a volume is more likely to be zero. This is the Hamiltonian for electrostatics.

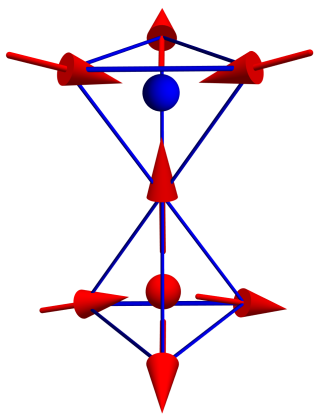

Figure 1.5: Spin ice excited state by flipping one spin. It creates two effective opposite charge excitations on the two tetrahedra.

Furthermore, higher energy excitations that violate the Gauss's law can be viewed as electric charges in the system. Since a single spin flip always creates two opposite charges in the neighboring tetrahedra, the charges are fractionalized excitations – a feature of topological systems. This is shown in Fig. 1.5. In the dual description, these excitations are magnetic monopoles [73].

As we can see, even as a classical system, spin ice is a very exotic case that is effectively equivalent to electrostatics. Each spin has equal probability to point either way, so that the local order parameters are always vanishing. However, it is different from the high-temperature paramagnet where all spins are uncorrelated and take completely

random configurations. Hence the name "collective paramagnets" or classical spin liquids. Experimentally, such physics is discovered in pyrochlore materials $Ho_2Ti_2O_7$ and $Dy_2Ti_2O_7$ [54].

Quantum spin ice — There is no quantum dynamics in the classical spin ice system: it is a statistic model with a partition function, but without equation of motion. Or, in the language of the effective field theory, there is not gauge field $\mathbf{A}$ conjugate to $\mathbf{E}$. On a lattice,

$$[A_i, E_j] = i\delta_{ij} \tag{1.8}$$

where i, j are labels of the lattice sites. So in the classical model a gauge invariant dynamical term $\mathbf{B} = \nabla \times \mathbf{A}$ does not exist.

To introduce such terms, we need to promote the system to a quantum one, and turn the classical spin liquid into a quantum spin liquid. A quantum spin liquid requires quantum dynamics in addition to the emergent Gauss's law. Broadly speaking, the dynamics play the role of $\mathbf{B}^2$ term in electrodynamics. They are to tunnel different classical spin liquid states between each other, leading to a long-range entangled quantum ground state and gapless photon excitations in this case.

For example, given the quantum XXZ model on the pyrochlore lattice [61–64]

$$\mathcal{H}_{\text{XXZ}} = \mathcal{H}_{\text{SI}} + \mathcal{H}_{\pm}, \tag{1.9}$$

where $\mathcal{H}_{\text{SI}}$ is the classical spin ice Hamiltonian, and

$$\mathcal{H}_{\pm} = -J_{\pm} \sum_{i,j} (S_i^+ S_j^- + S_i^- S_j^+). \tag{1.10}$$

If $J_{zz} \gg J_{\pm}$, then the low energy sector of the theory is restricted to the Hilbert space built from configurations that obey the ice rules.

Such a Hamiltonian cannot be solved analytically, but let us qualitatively explain the physics. Here, each of the classical two-in-two-out configuration is not the eigenstate or ground state of the Hamiltonian anymore, since it is not eigenstate of $\mathcal{H}_{\pm}$. So there is one quantum ground state (modulo the topological degeneracy) in this model instead of extensively-degenerate ones. The quantum ground state is essentially a superposition of the two-in-two-out states, with balanced weights such that it becomes an eigenstate of the Hamiltonian.

Inspired by the works of Rokhsar and Kivelson, [74], it is possible, by restricting states to the low-energy subspace satisfying the ice rules, and introducing some extra interactions in the Hamiltonian, to make the quantum spin ice model exactly soluble [65, 75]. In this case, the superposition could be an equal weight superposition, enabling one to made analytical calculations of the physics.

The other eigenstates, which are other superpositions of the two-in-two-out classical states, become the photon excitations and magnetic monopole excitations. The states

breaking the ice rule become electrically charged excitations following a similar logic. The photon sector, in the long-range limit, is described by the Hamiltonian

$$\mathcal{H}_{\text{QSI}} = \frac{\epsilon}{2}\mathbf{E}^2 + \frac{1}{2\mu}\mathbf{B}^2, \tag{1.11}$$

which is a lattice realization of U(1) electrodynamics.

Such a quantum ground state is genuinely quantum topological order in the following senses. First it does not break the symmetry of the system, even under arbitrary small perturbations. This cannot happen in a classical system — small perturbations can always lift the extensive degeneracy of the ground states until there is only one left. Second, such type of states have long range entanglement, from the fact that essentially all product states obeying the Gauss's law are superimposed to form the entangled state.

Quantum spin ice is an elegant example for quantum spin liquid induced by frustrated magnetism. It is one of the cleanest and most experimentally relevant example we know of a compact U(1) lattice gauge theory [76, 77]. It harbors both electric charges and magnetic monopole excitations envisioned by Dirac in 1931 [78]. In some sense, it is a mini toy universe, in which scientists have created their own version of light.

More generally, many quantum spin liquids can be described by different gauge theories. Apart from the simplest U(1) electromagnetism, there are many more exotic possibilities. We will introduce one in the next section.

1.4 Rank–2 U(1) gauge theory

We have learned that the quantum spin ice as a quantum spin liquid is described by the conventional electromagnetism. More generally, other different gauge theories can also describe different kinds of spin liquids. The quantum versions can further more be symmetry enriched. Hence there is an exciting, vast landscape of quantum states from spin liquids for us to explore theoretically and try to realize experimentally.

In this section, we will focus on a particularly interesting class of gauge theories that can act as effective physics for spin liquids. They are the rank–2 U(1) [R2–U1] versions of electrodynamics [36, 79–81].

Initially motivated as algebraic spin liquids, they are then shown to be a special limits of Lifshitz gravity [82]. More recently, the charge excitations in these theories, dubbed "fractons", have attracted tremendous interest, since they are linked to the fracton topological orders [34, 36, 83–86]. The fracton topological orders are a very intriguing class of three-dimensional lattice models that have extensive, robust quantum ground state degeneracy that is proportional to the exponential of the linear size of the system, something far beyond our conventional understanding of topological orders.

Here, following [36, 79], we derive the relationship between electric, magnetic and gauge fields within R2-U1 theories. The first example we use is the vector-charged, traceless version of the R2-U1. We start with the classical electrostatics which is realized in the second part of the thesis. It is a classic statistical system, and corresponds to the classical spin ice. We then introduce the dynamics to make it a full quantum theory. After the example, we go through other versions of R2-U1.

The Gauss's laws — There are several different forms of R2-U1 theory, as discussed in Refs. [36, 79]. These versions differ in terms of the definitions of the charge and also the generalized Gauss's laws. In each case, the starting point is a symmetric rank-2 tensor,

$$E^{ij} = E^{ji}, \tag{1.12}$$

which acts as the electric field in the system.

We first review the case of vector-charged, traceless R2-U1, which is the most relevant to our study. Brief introductions to other versions will follow.

In this version, beside the symmetric property, we further impose the condition that this tensor is traceless

$$E^i_i = 0. \tag{1.13}$$

The next step is to specify a divergence condition on the electric field tensor, which will play the role of Gauss's laws for the emergent electrodynamics/electromagnetism. For this purpose, we first define the charge. In this case it is a vector (the cases of scalar charge are discussed later in this section)

$$\rho^j = \partial_i E^{ij}. \tag{1.14}$$

In the low energy sector, the system is charge free, and Eq. (1.14) becomes a generalized zero-divergence condition

$$\partial_i E^{ij} = 0, \tag{1.15}$$

which plays the role of the Gauss's laws.

The gauge and magnetic fields — As in conventional electrodynamics, the conjugate of **E** is the rank-two gauge field **A**, which also has to be symmetric to match the degrees of freedom,

$$A^{ij} = A^{ji}. \tag{1.16}$$

The Gauss's laws determine the form of gauge transformation. Consider a wave-function

$$|\Psi(\mathbf{A})\rangle\,. \tag{1.17}$$

We take a low energy configuration of **E** obeying the Gauss's laws (Eq. (1.15)) and construct a symmetrized operator that is equivalent to identity. Its action upon the wave function gives

$$\exp\left[\int dv\, -i(\lambda_i \partial_j E^{ij} + \lambda_j \partial_i E^{ij})\right] |\Psi(\mathbf{A})\rangle = |\Psi(\mathbf{A})\rangle\,. \tag{1.18}$$

By integration by parts and assuming vanishing boundary terms, we have also

$$\exp\left[\int dv\, i(\partial_i\lambda_j + \partial_j\lambda_i)E^{ij}\right]|\Psi(\mathbf{A})\rangle = |\Psi(\mathbf{A})\rangle\,. \tag{1.19}$$

Since E_{ij} conjugates with A_{ij}, it generates a transformation of $\mathbf{A}$. Thus

$$\exp\left[\int dv\, i(\partial_i\lambda_j + \partial_j\lambda_i)E^{ij}\right]|\Psi(\mathbf{A})\rangle = |\Psi(\mathbf{A} + \boldsymbol{\nabla}\otimes\boldsymbol{\lambda} + (\boldsymbol{\nabla}\otimes\boldsymbol{\lambda})^T)\rangle = |\Psi(\mathbf{A})\rangle\,. \tag{1.20}$$

That is, the low energy sector, the wave-function is invariant under gauge transformation

$$\mathbf{A} \to \mathbf{A} + \boldsymbol{\nabla}\otimes\boldsymbol{\lambda} + (\boldsymbol{\nabla}\otimes\boldsymbol{\lambda})^T, \quad \text{i.e.,} \quad A^{ij} \to A^{ij} + \partial^i\lambda^j + \partial^j\lambda^i. \tag{1.21}$$

Similarly, the traceless condition

$$\exp\left[\int dv\, -i\gamma\delta_{ij}E^{ij}\right]|\Psi(\mathbf{A})\rangle = |\Psi(\mathbf{A})\rangle \tag{1.22}$$

leads to another gauge transformation

$$A^{ij} \to A^{ij} + \gamma\delta^{ij}. \tag{1.23}$$

Finally, the magnetic field is obtained by finding the simplest gauge-invariant quantity built from $\mathbf{A}$. This means finding the shortest combination of the differential operators ∂_i and other tensors ϵ_{ijk}, δ_{ij} to act upon A_{ij}, which has to be invariant under the gauge transformation.

The simplest type of term one may consider first are terms of the form found in a conventional U(1) gauge theory, mimicking the curl of the gauge field. For example, one can consider

$$B^{ij}_{\text{test}} = \epsilon^i_{ab}\partial^a A^b_j. \tag{1.24}$$

However, this is not gauge invariant. Under gauge transformation, it becomes

$$B^{ij}_{\text{test}} \to B^{ij}_{\text{test}} + \epsilon^i_{ab}\partial^a(\partial^b\lambda_j + \partial^j\lambda_b + \delta^b_j\gamma), \tag{1.25}$$

and the second and third term from the gauge transformation do not vanish in general. A systematic examination of all possible terms is possible, either by hand or using machine algebra.

The correct form of magnetic field was first reported by Xu et al. in Ref. [36]. It has to have three derivatives acting on the gauge field

$$\begin{aligned} B^{ij} =& \frac{1}{2}[\epsilon^j_{ab}(\partial^a\partial_k\partial^i A^{bk} - \partial^a\partial^2 A^{ib}) \\ &+ \epsilon^i_{ab}(\partial^a\partial_k\partial^j A^{bk} - \partial^a\partial^2 A^{jb})]. \end{aligned} \tag{1.26}$$

One can check and see that removal of any term will destroy the gauge invariance.

Hence we can write down the Hamiltonian

$$\mathcal{H} = E_{ij}E^{ij} + B_{ij}B^{ij}. \tag{1.27}$$

Fracton excitations — From the Gauss's laws and the traceless and symmetric conditions of the electric field, we can derive

$$\int dv\, \vec{\rho} = \int dv\, \partial_i E^{ij} = 0 \quad \text{charge conservation} \tag{1.28}$$

$$\int dv\, \vec{x} \times \vec{\rho} = -\int dv\, \epsilon_{ijk} E^{jk} = 0 \quad \text{“angular momentum” conservation} \tag{1.29}$$

$$\int dv\, \vec{x} \cdot \vec{\rho} = -\int dv\, E^i_i = 0 \quad \text{dipole conservation} \tag{1.30}$$

$$\int dv \left[(\vec{x} \cdot \vec{\rho})\vec{x} - \frac{1}{2}x^2\vec{\rho} \right] = 0 \tag{1.31}$$

In conventional electromagnetism, there is only the charge conservation law. This means that the system cannot create a net charge by itself: only pairs of positive and negative charge can be created. A single charge can, however, propagate in the system, since this only changes the net dipole of the system, and does not violate the charge conservation law. An equivalent point of view is that a dipole operator does not violate the Gauss's laws, hence it is allowed. Dipole operators are exactly what move a charge around.

In the R2-U1 case, charge conservation is not the only conservation law imposed by the Gauss's laws. The extra Gauss's laws also impose conservation of certain multipoles. These new conservation laws then restrict the mobility of the vector charges.

For example, the "angular momentum" conservation law (Eq. (1.29)) forbids the movement of a vector charge $\vec{\rho}$ perpendicular to itself. Consider a vector charge $\vec{\rho}$ moving from location $\vec{x}$ to $\vec{x} + \Delta\vec{x}$, where $\Delta\vec{x}$ is perpendicular to $\vec{\rho}$, then we have

$$\vec{x} \times \vec{\rho} \neq (\vec{x} + \Delta\vec{x}) \times \vec{\rho}, \tag{1.32}$$

since $\Delta\vec{x} \times \vec{\rho} \neq 0$. Therefore, the charge excitation is forbidden to move perpendicularly to itself.

In a similar spirit, the dipole conservation law (Eq. (1.30)) forbids the movement of a vector charge $\vec{\rho}$ parallel to itself. Consider a vector charge $\vec{\rho}$ moving from location $\vec{x}$ to $\vec{x} + \Delta\vec{x}'$, where $\Delta\vec{x}'$ is now parallel to $\vec{\rho}$. Then we have

$$\vec{x} \cdot \vec{\rho} \neq (\vec{x} + \Delta\vec{x}') \cdot \vec{\rho}, \tag{1.33}$$

since in this case $\Delta\vec{x}' \cdot \vec{\rho} \neq 0$. Consequently, in the vector-charged, traceless version of R2-U1, a vector charge excitation is fully fractonic, i.e., it cannot move in any direction of the system.

Another helpful way to understand the immobility of charge excitations is to examine the multipolar charge operators and check whether they violate the Gauss's laws or not. For example, there are two types of vector-charge dipole (or quadrupole) operators, as illustrated in Fig. 1.6a.

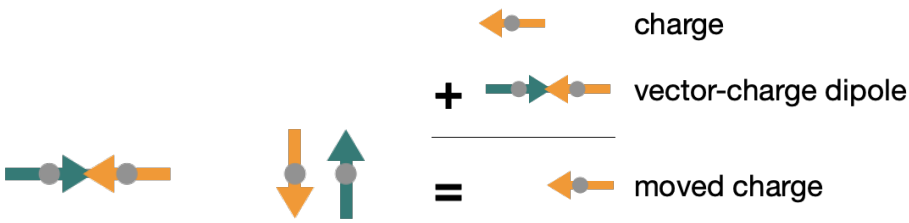

(a) quadrupole moments formed by dipoles of vector charges

(b) a mtrix element with ta

Figure 1.6: (a) Quadrupole moments formed by dipoles of vector charges. (b) A matrix element with the character of a quadrupole is needed to move a vector charge $\boldsymbol{\rho}$. The resulting motion is parallel to the vector charge.

Given these vector-charge dipole configurations, one can explicitly compute for them the multipole quantities

$$\int dv\, \vec{x} \times \vec{\rho} \quad \text{and} \quad \int dv\, \vec{x} \cdot \vec{\rho} \tag{1.34}$$

and find that both configurations have non-zero values for one of these quantities. Therefore, they are forbidden at the low energy sector. Note that they are exactly the multipolar operators that move a single vector charge, this means a single vector charge is immobile in the system.

Different versions of R2-U1 One can study the physics of other versions of R2-U1 following the example above. We list the other most symmetric three versions, which are combinatoric choices of scalar charge/vector charge and traceless/traceful.

Vector charged, traceful — The Gauss's laws for this version are

$$\partial_i E^{ij} = 0 \tag{1.35}$$

without requiring E^{ij} to be traceless. The corresponding gauge symmetry is

$$A^{ij} \to A^{ij} + \partial^i \lambda^j + \partial^i \lambda^j \tag{1.36}$$

The magnetic field is then defined as

$$B^{ij} = \epsilon_{iab}\epsilon_{jcd}\partial^a \partial^c A^{bd} \tag{1.37}$$

The conservation laws for the vector charges are

$$\int dv\, \vec{\rho} = \int dv\, \partial_i E^{ij} = 0 \quad \text{charge conservation} \tag{1.38}$$

$$\int dv\, \vec{x} \times \vec{\rho} = -\int dv\, \epsilon_{ijk} E^{jk} = 0 \quad \text{“angular momentum” conservation} \tag{1.39}$$

$$\tag{1.40}$$

so that a vector charge can move in the same direction it points.

Scalar charged, traceless — The Gauss's laws are

$$\partial_i \partial_j E^{ij} = 0 \qquad E^i_i = 0 \tag{1.41}$$

The corresponding gauge symmetry is

$$A^{ij} \to A^{ij} + \partial^i \partial^j \lambda + \delta^{ij} \gamma \tag{1.42}$$

The magnetic field is

$$B^{ij} = \frac{1}{2} \left(\epsilon^i_{ab} \partial^a A^{bj} + \epsilon^j_{ab} \partial^a A^{bi} \right) \tag{1.43}$$

The conservation laws for the vector charges are

$$\int dv\, \rho = \int dv\, \partial_i \partial_j E^{ij} = 0 \quad \text{charge conservation} \tag{1.44}$$

$$[\int dv\, \boldsymbol{x} \rho]^k = -\int dv\, \partial_j E^{kj} = 0 \quad \text{dipole conservation} \tag{1.45}$$

$$\int dv\, \boldsymbol{x}^2 \rho = \int dv\, E^k_k = 0 \quad \text{quadrupole conservation} \tag{1.46}$$

$$\tag{1.47}$$

so that a scalar charge is a fracton.

Scalar charged, traceful — The Gauss's laws are

$$\partial_i \partial_j E^{ij} = 0 \tag{1.48}$$

The corresponding gauge symmetry is

$$A^{ij} \to A^{ij} + \partial^i \partial^j \lambda \tag{1.49}$$

The magnetic field is

$$B^{ij} = \epsilon^i_{ab} \partial^a A^{bj} \tag{1.50}$$

The conservation laws for the vector charges are

$$\int dv\, \rho = \int dv\, \partial_i \partial_j E^{ij} = 0 \quad \text{charge conservation} \tag{1.51}$$

$$[\int dv\, \boldsymbol{x} \rho]^k = -\int dv\, x^k \partial_i \partial_j E^{ij} = 0 \quad \text{dipole conservation} \tag{1.52}$$

so that a scalar charge is also a fracton.

The rank-2 U(1) theories are interesting in many aspects. First, the electromagnetic sector describe tensorial spin liquid without any symmetry-breaking [36]. Such effective theories for condensed matter system do not need to respect Lorentz symmetry, so they are less familiar to physicists. Second, some of the charge excitations are forbidden to move due to multi-polar charge conservation laws. These excitations, also known as fractons, also exist in the gapped models of fracton topological order, subsystem symmetry protected states, and subsystem symmetry-breaking states. Some of these states can be obtained by Higgsing the photons of rank-2 U(1) theory in specific ways [87, 88]. Hence, the rank-2 U(1) theories are the gateways toward a new landscape of novel quantum states of matter. To understand their properties better, and realize them in experiments, will be very significant progress in condensed matter physics.

1.5 Outline of the thesis

The scientific content of this thesis can be divided into two parts. The first part is to deepen our understanding of fracton state of matter, that is, the connection between fracton states of matter and holographic toy models. In Chapter 2, we describe the basic properties of a simple, classical fracton model, and how it can be defined on the hyperbolic lattice, or a spatial slice of AdS_3. We show that this model satisfies some of the major properties of holographic entanglement properties. In Chapter 3, we make connections between the hyperbolic fracton model and the bit-thread picture. To be more exact, the classical hyperbolic fracton model is equivalent to a fixed, even distribution of classical bit-threads. These two chapters connect several different aspects of the holographic entanglement entropy and fracton models.

The second part of the thesis is concerned with the experimental realization of the fracton states of matter. We will show how to realize a classical rank-2 U(1) spin liquid in the framework of frustrated magnet on a breathing pyrochlore lattice. The Chapter 5 provides the necessary theoretical analysis needed for the model building. We introduce the pyrochlore spin model with nearest-neighbor anisotropic interacting, and work out the full irreducible representation fields on the pyrochlore lattice. This will be needed to construct the rank-2 tensorial electric field. In Chapter 6, we show that the low energy effective theory of a breathing pyrochlore model is a vector charged, traceless rank-2 U(1) gauge theory. Besides the theoretical analysis, we also point out that this model is particularly attractive due to the simple interactions required, and very likely to be realized in experiments.

Finally, in Chapter 7, we summarize this thesis and take an outlook of future interesting problems.

Chapter 2

Hyperbolic Fracton Model and Holography

The first part of the thesis is composed of Chapters 2,3,4. In this part, we will examine the links between fracton states of matter and gravity. This chapter focuses on a toy model that is simple yet bears the essential non-trivial physics we are interested it. That is, a plaquette fracton model defined in two-dimensional anti-de Sitter space (AdS) satisfies several essential properties of holographic duality: the mutual information of a boundary bipartition obeys the Ryu-Takayanagi formula, and the bulk reconstruction obeys subregion duality. A few more observations regarding isometry at finite energy and black hole entropy also qualitatively agree with the holographic duality.

To understand the significance of these results, some knowledge in both condensed matter and high energy theory, in particular the anti–de Sitter/conformal field theory correspondence (AdS/CFT), is necessary. The first few sections are devoted to providing a concise introduction to these ideas.

We then study the plaquette fracton model in AdS_2, or hyperbolic space, in detail. After describing its basic properties, including the subsystem symmetries and fracton excitations, we examine how the holographic properties are satisfied. A few other aspects, including the black holes and certain generalizations, are also discussed.

Next, we study another model dual to the hyperbolic fracton model. It is based on the eight-vertex construction on the dual lattice. It has the advantage of visualizing the information in the system, thus reveals some deeper secrets of the hyperbolic fracton model. The most important one is that the dual eight-vertex model turns out to be a realization of the bit threads, a construction widely used in the study of holography. This link is crucial as it implies a somewhat universal picture of the toy models of holography. The dual model and the concept of subsystem charge also makes it easier to resolve other issues, including isometry at finite energy and the microstates of the black hole.

Simple though the toy model may be, a lot of non-trivial implications can be inferred from the results. We end this chapter with a careful look at these implications and show an emerging web of connections between different subjects in condensed matter theory and holography.

2.1 Introduction

The holographic principle [2, 3] and anti-de Sitter/conformal field theory (AdS/CFT) correspondence [4, 5] have profoundly changed our understanding of quantum gravity. AdS/CFT is a duality between quantum gravity in $(d+1)$-dimensional asymptotically AdS spacetime and a d-dimensional CFT on its boundary. It comprises a striking conjecture that a gravitational system is equivalent to a strongly coupled quantum field theory without gravity. Besides unveiling some of the deepest mysteries of quantum gravity in its subsequent developments [6–11], the AdS/CFT correspondence also serves as a powerful tool for studying strongly coupled quantum field theories including many-body systems [89].

Another remarkable development in AdS/CFT is the realization of the intimate relation between the geometry of spacetime and quantum entanglement. Ryu and Takayanagi conjectured that the entanglement entropy of a boundary segment is measured by the area of certain extremal covering surface in the AdS geometry [22, 23]. Their seminal idea, now known as the Ryu-Takayanagi (RT) formula, has sparked a series of insightful works along this direction (for example, see review Ref. [90]).

AdS/CFT has deep connections with various condensed matter theory problems. One example is the multiscale entanglement renormalization ansatz (MERA) tensor networks [12]. Their structure bears considerable similarity with the renormalization scale represented by the radial direction of AdS space. Such insight by Swingle leads to a fruitful field of building toy models of AdS/CFT with tensor networks [13, 14, 16, 17], which in return demystify some intriguing properties of holography. For instance, the perfect tensor networks [13, 14] incorporate the quantum error correction feature of AdS/CFT and help to clarify the conundrum of subregion duality.

Since conformally invariant or strongly coupled systems are common themes in many-body physics, the condensed matter systems often sit on the CFT side when AdS/CFT is applicable [89]. Examples of many-body systems on the bulk side are rare [91–93]. Therefore it is desirable to seek many-body systems that, instead of being described by some CFT, mimic the behavior of gravity and sit on the AdS side of holography. Studying such systems not only is of interest to the condensed matter community, but also may provide us insights in understanding gravity.

This chapter aims to show that the recently discovered fracton models [29, 30] mimic gravity and can sit on the AdS side as a toy model of holography.

The fracton phases cover several types of exotic states in many-body systems, and have attracted much attention in the condensed matter community recently. For example, gapped fracton topological orders have intriguing sub-extensive ground-state degeneracy and (partially) immobile excitations [31, 87, 88, 94–99] (also see review Ref. [34]). The gapless versions of them are described by the rank-2 U(1) gauge theories [32, 33, 35, 100]. The fracton topological orders can also be obtained by gauging the subsystem symmetries of the model [31, 101], which inspired study of fracton models protected by subsystem symmetries as well [102, 103].

In this chapter, we study a classical fracton model with subsystem symmetry on the hyperbolic disk, or a spatial slice of AdS_3 spacetime. We show that such a system satisfies the major properties of AdS/CFT, in a manner similar to the holographic tensor networks. These properties include the AdS-Rindler reconstruction and subregion duality, and the RT formula for mutual information as the classical analog of entanglement entropy. They are satisfied exactly for a connected boundary subregion up to lattice discretization. The corrections for more complicated boundary subregions are also discussed. The hyperbolic fracton model gives the proper entropy for a naively defined black hole as well.

The chapter is arranged as follows: Sec. 1.2 provides some essential knowledge of AdS/CFT relevant to our work, mainly for readers not familiar with this discipline; Sec. 2.2 provides a concise summary of the major results;

Sec. 2.3 introduces the fracton model on the Euclidean lattice, and discusses various hints implying that it could be holographic; Sec. 2.4 introduces the fracton model on the hyperbolic lattice;

Secs. 2.5, 2.6 and 2.7 contain the major results of this work. These sections show that the model satisfies some major properties of AdS/CFT, and discuss some possible deviations; Sec. 2.8 discusses how to generalize the classical model to three dimension and to a quantum version; Sec. 2.9 presents a comparison of the hyperbolic fracton model and the holographic tensor networks to make clear what holographic properties are still beyond the scope of current construction; finally, Sec. 2.10 gives an outlook on the implications and future problems related to this work.

2.2 Summary of the main results

In this chapter we will demonstrate that the *hyperbolic fracton model*, a classical fracton model defined on a hyperbolic disk (a spatial slice of AdS_3), satisfies several key properties of AdS/CFT correspondence. The main results are summarized here, with detailed proofs and discussions presented subsequently.

Rindler reconstruction — In the hyperbolic fracton model defined by Eq. (2.19), given

the state, or spin configuration on a connected boundary subregion, the bulk states within the *minimal convex wedge* of the boundary can be reconstructed. The minimal convex wedge is essentially the entanglement wedge on a discrete lattice, which approximates the continuous case.

Ryu-Takayanagi formula for mutual information: For a bipartition of the boundary into two individually connected subregions denoted A and A^c, their mutual information in the classical model is defined as

$$I(A,B) = S(A) + S(B) - S(A \cup B). \tag{2.1}$$

Here $S(A)$ is the Shannon entropy,

$$S(A) = \sum_i p_i \log p_i, \tag{2.2}$$

where p_i is the probability of state i and the sum runs over all states. Mutual information is the classical analog of entanglement entropy, and for our simple model, Eq. (2.1) obeys the Ryu-Takayanagi formula (RT formula):

$$I(A, A^c) = k_{\mathrm{B}} \log 2 \times |\gamma_A| \,, \tag{2.3}$$

where $|\gamma_A|$ is the area of the minimal covering surface in the bulk, or in this case the length of geodesic covering boundary subregion A. In Sec. 2.6.1 we will explain in more detail why the classical mutual information is a proper analogy of the quantum entanglement entropy originally considered by Ryu-Takayanagi.

Black hole entropy: A naively defined black hole in the model has entropy proportional to the area of the black hole horizon. Also with the presence of black hole, the available lowest energy boundary states increase as expected.

2.3 Fracton model on the Euclidean lattice

2.3.1 The model

In this section, we will introduce one of the simplest classical toy models with subsystem symmetries. The model is two-dimensional, and does not realize a fracton topological order (FTO) in the quantum limit. Fracton topological orders have only so far been found in three-dimensional models, often by gauging 2D subsystem symmetries of a 3D system [85, 86]. Nonetheless, our model does posses well-defined fracton excitations in the classical limit, and is the simplest model known to do so [104, 105].

The introduction is done in the flat space first, before being transplanted to the hyperbolic space. For such models, the concept of subsystem symmetry is important.

Subsystem symmetry means symmetry operations that commute with the Hamiltonian that acts not locally, nor globally, but on an extended subset of the system. In our model in flat space, the subsystem symmetry is a line-symmetry.

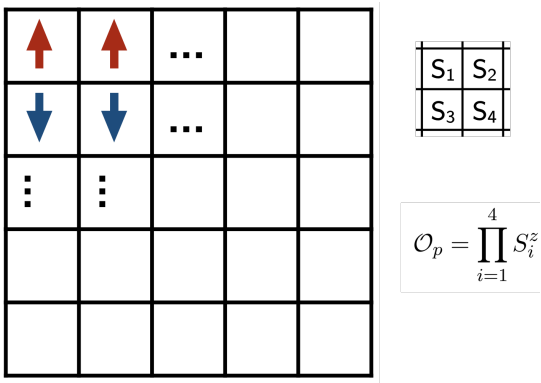

Figure 2.1: The fracton model on the Euclidean lattice defined by Eq. (2.5). On each center of the unit square sits an Ising spin. The right panel shows how operator O_p in Eq. (2.4) is defined. Figure reproduced from Ref. [48].

The model is defined on the square lattice with an Ising spin $S_i^z = \pm 1$ placed at the center of each square, as shown in Fig. 2.1. For every four-spin cluster sharing the same corner, we define an operator

$$\mathcal{O}_p = \prod_{i=1}^{4} S_i^z, \tag{2.4}$$

The Hamiltonian is the negative sum of such operators on all four-spin clusters,

$$\mathcal{H}_{\text{cl}} = -\sum_p \mathcal{O}_p. \tag{2.5}$$

This model is a two-dimensional version of the "plaquette model" that has been discussed in a rich variety of contexts. As a fracton model it is discussed in Ref. [31]. It is also a self-dual model with subsystem symmetries discussed in Refs. [101–103]. It is dual to an exactly solvable square-lattice eight-vertex model [106], whose implication will be discussed in the next chapter. The classical model has also been studied as a spin glass statistical physics problem [104, 105], and proposed as a string regularization known as the gonihedric Ising model [107–109].

2.3.2 Properties of the fracton model

Let us now examine the exotic feature of the ground states and excitations in this mode.

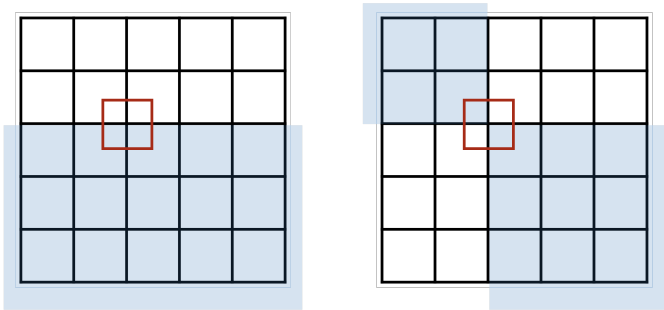

(a) Ground state **(b)** Another ground state

Figure 2.2: Ground states for the fracton model on the Euclidean lattice. (a) Starting from the ground state of all spins up, a new ground state can be constructed by flipping all spins on one side of a vertical or horizontal line of the lattice. In this figure flipping all spins in the blue region will create another ground state. (b) By repeating the procedure described in (a) for different lines consecutively, any ground state can be constructed. This figure shows a ground state constructed by two such flipping operations. Figure reproduced from Ref. [48].

Feature one: Sub-extensive ground state entropy —

The ground states are the classical spin configurations satisfying

$$\mathcal{O}_p = 1 \tag{2.6}$$

on every four-spin cluster. On a lattice of size $L_x \times L_y$ with open boundary condition, the ground state degeneracy and entropy are

$$\begin{aligned} \Omega &= 2^{L_x+L_y-1}\,, && (2.7)\\ S &= k_\mathrm{B}\log\Omega = k_\mathrm{B}\log 2\times(L_x+L_y-1) \\ &\sim k_\mathrm{B}\log 2\times(\text{Boundary area})\,. && (2.8) \end{aligned}$$

To see this, we can start from the all-spin-up configuration, which is obviously a ground state. We then flip all spins on one side of a straight line in the $x-$ or $y-$direction, as shown in Fig.2.2a. Equivalently we can also flip spins on one line but this former operation will prove move useful on the hyperbolic lattice. Since such operation only flip even number of spins on every four-spin cluster, the values of all operators $\mathcal{O}_p$ remain invariant. Or equivalently $\prod_{i \text{ in a line}} S_i^x$ commute with the Hamiltonian.

So after the flipping the system is in another ground state. By performing multiple such operations for different straight lines as shown in Fig.2.2b, all ground states can be constructed explicitly. From the construction we can see the Shannon entropy of the ground state ensemble scales with the number of straight lines, which is also the size of the boundary, hence comes Eq.(2.8). Actually, this already hints some similarity between the toy model and gravity.

One should not confuse the sub-extensive ground state entropy with the linear-sized sub-extensive *quantum* ground state entropy of three-dimensional fracton topological orders, even though they are intimately related. Here the sub-extensive ground state entropy is a counting of the independent subsystem symmetries.

Feature two: immobile fracton excitations —

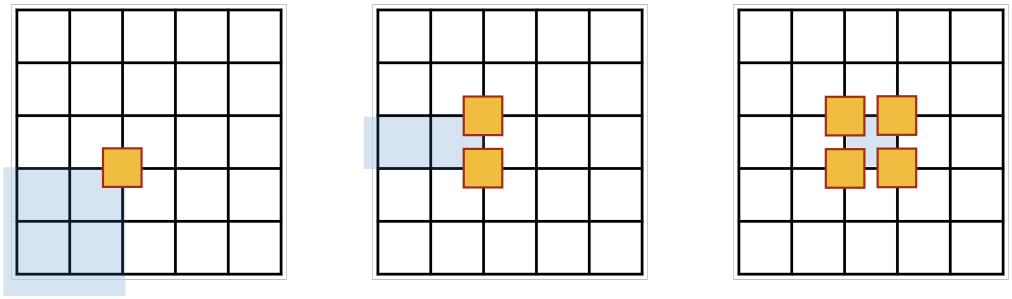

(a) One fracton state **(b)** Two-fracton bound state **(c)** Four-fracton bound state

Figure 2.3: Fracton excitations and their bound states. (a) A single fracton excitation. It is created by flipping spins in the blue region which is bounded by two cuts. It is "topological", in the sense that it is not movable by any local, finite number of spin flips without costing the system more energy (i.e., creating more fractons in the system). (b) A two-fracton bound state. It is created by flipping a semi-infinite line of spins in the blue region. It is also "topological". By local operations it can only move horizontally. (c) A four-fracton bound state. It is created by a single spin flip. It can move freely on the lattice, and is not "topological". Figure reproduced from Ref. [48].

The first excited state of the system is created by flipping the sign of only one operator $\mathcal{O}_p$, while keeping the others the same. Such construction is illustrated in Fig. 2.3a: From any ground state, one can pick two lines in the $x-$ and $y-$ direction respectively that intersect at the target position. The two lines split the lattice into four parts. Then flip the spins in one part of the four. A fracton will be created at the corner of the flipped spin region. In the limit of infinitely large lattice, the creation of a fracton becomes "topological" in the sense that it has to operate on an infinite number of spins. Any local operation, i.e., flipping finitely many spins in the bulk, will create at least four fractons.

Furthermore, the fracton excitation is immobile in the sense that it is impossible for a local operation to move it without creating new fractons and costing more energy. To move the fracton, a nonlocal operation of flipping a semi-infinite line of spins next to the fracton is necessary.

Feature three: Fracton bound states with enhanced mobility — A bound state of two fractons are created by the non-local operation of flipping a semi-infinite line of spins,

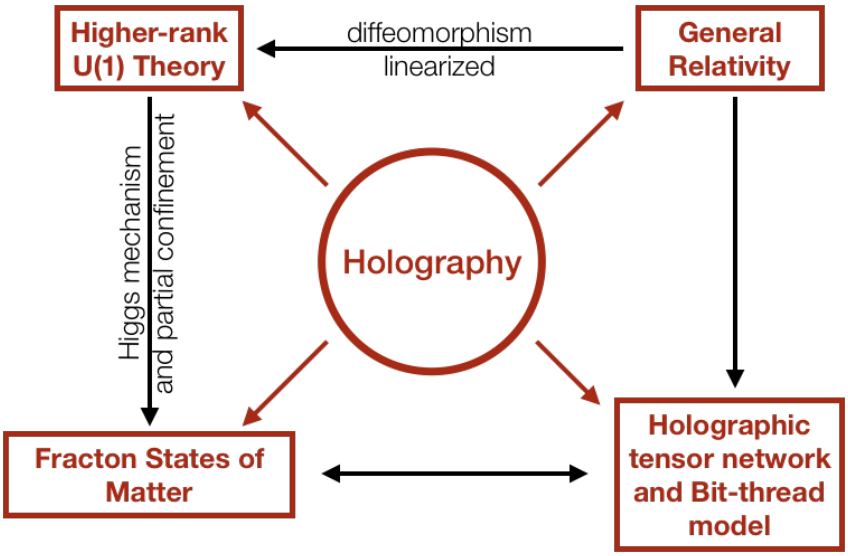

Figure 2.4: Speculated connections between fracton model and holography. A few hints are in this web of connection. The symmetric rank-two gauge theories have gauge structures similar to different subsets of linearized diffeomorphism. These theories on a lattice yield various gapped fracton models after Higgsing. Since gravity is holographic, this suggests that a fracton model on a hyperbolic lattice may also be partly holographic. To show this is actually true is the central task of the part I of the thesis.

as illustrated in Fig. 2.3b. Such a bound state can only move in a one-dimensional submanifold of the lattice: by extending or shrinking the semi-infinite line of flipped spins – which is a local operation – the bound state can move along the line. However it cannot move in the perpendicular direction, in a spirit similar to the localization of fractons.

Finally, a four-fracton bound state is locally created by a single spin flip shown in Fig. 2.3c. It is obviously free to move in the system.

The three features above are highly generic in many fracton models, including the gapped fracton topological orders, gapless rank-2 U(1) theories, and other fracton states of matter with subsystem symmetries.

2.3.3 Hints of Holography

Though the model show some very exotic features, its connection to holography is not obvious at all. Here we discuss some hints from properties of certain fracton models in two- and three-dimensional flat space. The overall speculated big picture of these connections is illustrated in Fig. 2.4.

Sub-extensive ground state entropy — The first hint is that the entropy of the system

at $T = 0$ is proportional to its boundary area, as already discussed in Eq. (2.8). This echoes the famous entropy of a black hole, which later motivated the idea of holography for gravitational system in general [3, 90, 110].

Indeed, we will find out in later sections that the structure of degenerate ground states, or subsystem symmetries, is vital for their holographic properties.

Similarity between linearized gravity and rank-two U(1) gauge theory — The second hint lies in the effective theories of the gapless rank-2 U(1) (R2-U1) symmetric tensor gauge theories [32, 33, 35, 87, 88]. The R2-U1s are pivotal in describing fracton states in general. As a gapless gauge theories, its charges are fractons whose mobility is constrained by multipole conservation laws. The gapless bosons are argued to resemble gravitons. By Higgsing scalar charged R2-U1s following specific recipes, gapped fracton topological orders can be obtained.

The fracton excitations in our toy model are qualitatively described by the scalar charged traceless R2-U1, except that there is no real dynamics in the classical model.

To see the similarity between R2-U1 and gravity, first let us review some basic knowledge of linearized Einstein gravity. Assuming the metric $g^{\mu\nu}$ of the spacetime has only small perturbation on top of the flat Mankowski spacetime,

$$g^{\mu\nu} = \eta^{\mu\nu} + h^{\mu\nu} \ , \tag{2.9}$$

where $\eta^{\mu\nu} = \mathrm{diag}(-1,1,1,1)$ is the Minkowski metric, and $h^{\mu\nu}$ is the small perturbation. In the linearized limit, its gauge symmetry is a subset of the differmorphism invariance [35, 111]

$$h^{\mu\nu} \to h^{\mu\nu} + \partial^\mu \xi^\nu + \partial^\nu \xi^\mu \ . \tag{2.10}$$

However h^{00} and h^{i0} end up as Lagrangian multipliers in the Lagrangian. The physical degrees of freedom are the spatial components h^{ij}, $(i,j = 1,2,3)$, whose canonical conjugates are denoted π^{ij}. We can write down the gauge constraints and gauge transformations for them. For the convenience of comparing to rank-two U(1) theories, we write them in two groups:

$$\begin{aligned} \partial_i \pi^{ij} &= T^{0j} \ , \\ h_{ij} &\to h^{ij} + \partial^i \xi^j + \partial^j \xi^i \ , \end{aligned} \tag{2.11}$$

and

$$\begin{aligned} \partial_i \partial_j h^{ij} - \partial^2 h^i_i &= T^{00} \ , \\ \pi^{ij} &\to \pi^{ij} + \partial^i \partial^j \alpha - \delta^{ij} \partial^2 \alpha \ . \end{aligned} \tag{2.12}$$

Now we turn to the rank-two U(1) theories. One version of them has a symmetric tensorial electric field

$$E^{ij} = E^{ji} \ , \tag{2.13}$$

with associated vector charge defined as

$$\partial_i E^{ij} = \rho^j \ . \tag{2.14}$$

As a result, the corresponding gauge field has symmetry [80]

$$A^{ij} \to A^{ij} + \partial^i \lambda^j + \partial^j \lambda^i \ . \tag{2.15}$$

If E^{ij} is identified as the conjugate momentum of A^{ij}, Eq. (2.14,2.15) are equivalent to Eq. (2.11).

Since h^{ij} and π^{ij} are conjugate with each other, we can also treat π^{ij} as the gauge field and h^{ij} as the momentum. This is partially captured by another version of the rank-2 U(1) theory, which has a symmetric, traceless tensorial electric field, and associated scalar charge, defined by

$$E^i{}_i = 0, \ \partial_i \partial_j E^{ij} = \rho \ . \tag{2.16}$$

Its gauge freedom is

$$A^{ij} \to A^{ij} + \partial^i \partial^j \lambda \ . \tag{2.17}$$

As Ref.[35] pointed out, the similarity between Eq. (2.16,2.17) and Eq. (2.12) implies some shared properties between gravity and rank-2 U(1) theories.

Other studies have also shown connections between fracton models and gravity. For example, Ref.[112] shows that linearized gravity harbors gapless topological order. More recently, the foliated field theory for fracton models has been proposed and found to correspond to a singular limit of tetradic Palatini gravity [113], indicating connections between fracton topological order and soft hairs in gravity.

2.4 The Hyperbolic Fracton Model

2.4.1 The Hyperbolic Lattice and the Hamiltonian

Given various hints of the similarity between gravity and fracton model, it is natural to ask if the fracton model exhibits holographic properties as well.

In order to obtain results in correspondence with the AdS/CFT conjecture, it is necessary to work in the anti-de Sitter space. This is because holography is the duality between quantum gravities in anti-de Sitter spacetime and quantum field theories on their boundaries. More specifically, we will investigate the fracton model on the hyperbolic disk (AdS_2). It is a two-dimensional space of constant negative curvature as a Cauchy slice of the AdS spacetime.

The 2D square-lattice fracton model introduced in Sec. 2.3 is not suitable for studying this type of holography. It does have the right number of degrees of freedom to be "holographic", in the sense that the boundary determines the bulk completely within the ground state sector. However, because it is defined on a square lattice in flat space, it cannot have the correct entanglement structure as the holography discussed in AdS/CFT. Therefore it will not satisfy key results such as the RT formula and the Rindler construction.

Nonetheless, the model in the hyperbolic space needs to preserve the most essential properties from the flat lattice model. That is, we would like to have the same four-spin interactions and subsystem symmetry along the "straight lines" – which are geodesics in the AdS_2. This leads to the pentagon tessellation, a symmetric, uniform tiling of the hyperbolic disk with pentagons. The hyperbolic lattice is illustrated in Fig. 2.5. On this lattice most features of the flat lattice model are preserved as we explain below. We also note that the fracton model on a curved space has been discussed in Refs. [95, 114, 115]. The choice of tessellation is not unique. With different tessellations we have different hyperbolic lattices, but as long as a model has the same structure of subsystem symmetries, it will share the same holographic entanglement properties discussed in this chapter. This will be discussed in a future publication [116].

The technical term for our choice of pentagon tiling is the $(5,4)$ tessellation of the hyperbolic disk (Fig. 2.5), where 5 refers to the number of edges of the pentagon, and 4 referes to the fact that each corner of a pentagon is shared by four pentagons in total. In other words, each face has 5 edges and each vertex has 4 edges. An Ising spin of value ± 1 is placed at the *center* of each pentagon in the lattice.

In the $(5,4)$ tessellation we define the same operator for four spins on pentagons sharing a corner

$$\mathcal{O}_p = \prod_{i=1}^{4} S_i^z \,, \tag{2.18}$$

where i runs over four spins, and $S_i^z = \pm 1$ are the Ising degrees of freedom. The Hamiltonian is

$$\mathcal{H} = -\sum_p \mathcal{O}_p \,, \tag{2.19}$$

$\mathcal{O}_p$ on different clusters are independent of each other.

When analyzing the fracton model on the flat lattice, the subsystem symmetry is described by operations of splitting the lattice by a straight line. The straight lines are essentially geodesics in the Euclidean geometry, composed of the edges in the square lattice. By construction, every spin is unambiguously on one side of the line.

On the hyperbolic disk, the geodesics become arcs on the disk that intersect the disk boundary perpendicularly on both ends. Thus the geodesics defined by the $(5,4)$ tessellation, i.e., those formed by the edges of the pentagons, play an important role in our analysis. They are referred to as *"pentagon-edge geodesics"*. All other conventional

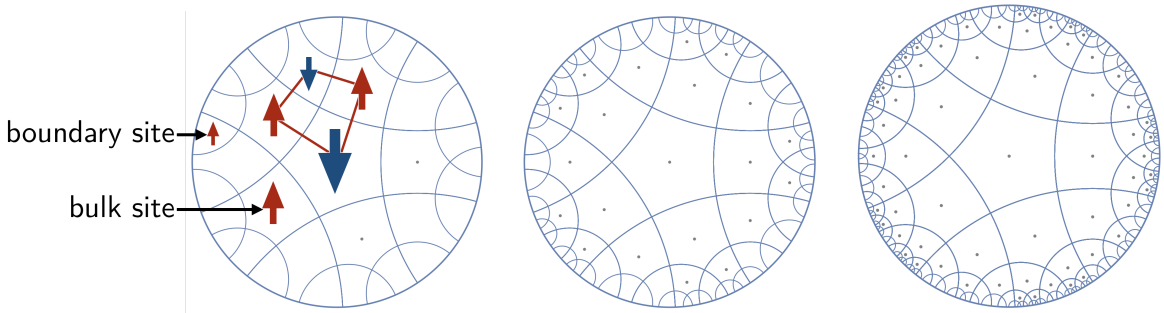

(a) Hyperbolic lattice 1 **(b)** Hyperbolic lattice 2 **(c)** Hyperbolic lattice 3

Figure 2.5: Hyperbolic lattice for the fracton model. (a): The lattice as the (5,4) tessellation of the hyperbolic disk. The spins sit at the center of the unit plaquettes (pentagons in the bulk or plaquettes on the boundary). The red square shows four pentagons that form the four-spin cluster interaction term O_p [Eq. (2.18)]. (b,c): Lattices of different sizes. They can be obtained by adding more pentagon-edge geodesics far from the center. Figure reproduced from Ref. [48].

geodesics are simply refereed to as *"geodesics"*. The pentagon-edge geodesics are the blue arcs in Fig. 2.5.

The hyperbolic lattice is infinite. To study it in a controlled way, we introduce a cutoff and unambiguously define the bulk and boundary degrees of freedom. This is done by removing infinitely many pentagon-edge geodesics far from the center, and only keep the ones within certain radius. Lattices of different sizes are shown in Fig. 2.5. It is a common treatment in AdS/CFT. On the CFT side, an ultraviolet cut-off is applied, and on the AdS side, the AdS space become finite-sized.

After the cutoff, finitely many pentagon-edge geodesics remain in the lattice, whose number is denoted as N_g. There are finitely many pentagons in the system. Their associated spins are the bulk degrees of freedom. Next to the boundary cut-off there are $2N_g$ faces that are not pentagons, each partially bounded by a segment of the boundary. We place an Ising spin on each of them as boundary degrees of freedom. The number N_g is thus a measure of the boundary size of the lattice. In Fig. 2.5, finite lattices of different sizes are illustrated.

2.4.2 Ground States and Fracton Excitations

The ground states and excitations of the hyperbolic fracton model can be explicitly constructed by simply replacing operations using the straight lines in the flat lattice with pentagon-edge geodesics.

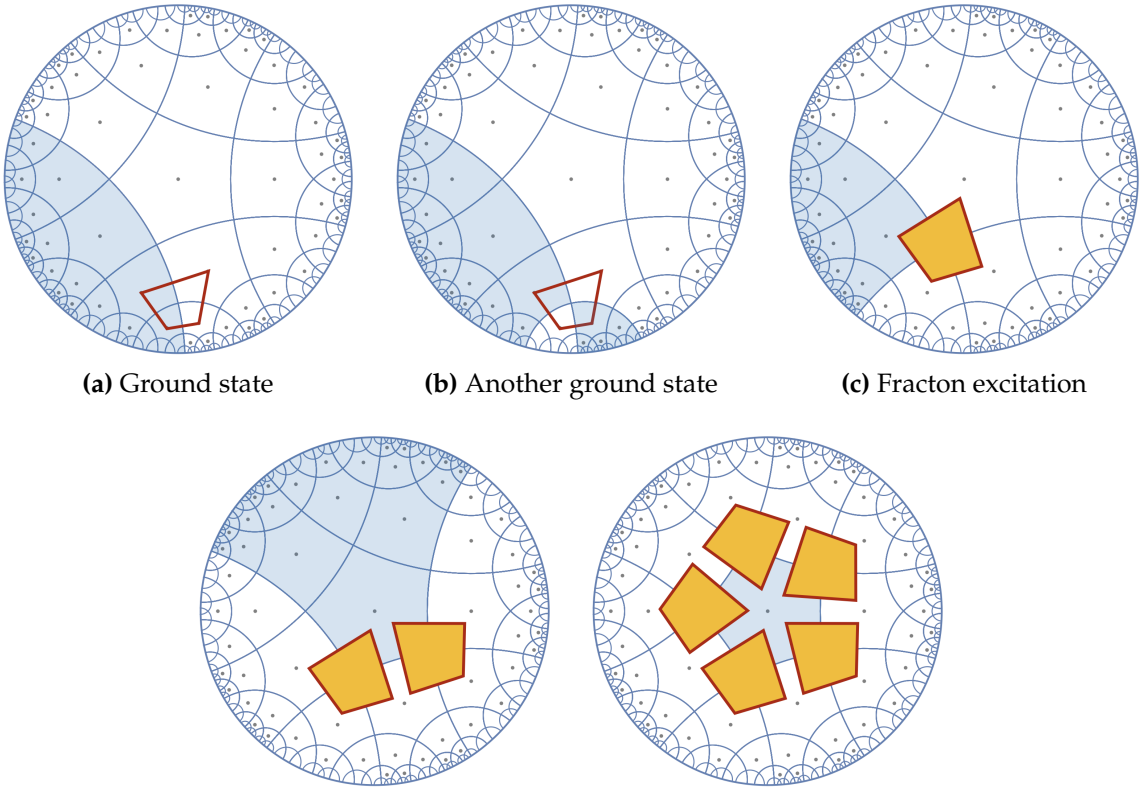

(a) Ground state **(b)** Another ground state **(c)** Fracton excitation

(d) Two fracton excitation **(e)** Five-fracton bound state

Figure 2.6: The ground states and fracton excitations in the hyperbolic fracton model. (a),(b): Constructions of different ground states by flipping all spins on one side of a chosen pentagon-edge geodesic. The four-spin cluster highlighted in red has its operator [Eq. (2.4)] value invariant. (c): A single-fracton excitation created by flipping a quadrant of the spins divided by two intersecting geodesics. It is a topological excitation since it involves flipping infinitely many spins. (d): Two-fracton excitation. Unlike the case of the Euclidean lattice, they are not movable by local operations. (e): Five-fracton bound state created by a single spin flip. It is free to move on the lattice. Figure reproduced from Ref. [48].

The ground state degeneracy and entropy for this model are respectively

$$\Omega = 2^{N_g+1}\,, \tag{2.20}$$

$$\begin{aligned} S &= k_B \log \Omega = k_B \log 2 \times (N_g + 1) \\ &\approx \frac{k_B \log 2}{2} \times (\text{boundary area})\,. \end{aligned} \tag{2.21}$$

From the ground state of all-spins-up, any other ground state can be constructed by the procedure of choosing a pentagon-edge geodesic and flipping the spins on one side of it several times. Since a pentagon-edge geodesic cuts the four-spin clusters in a two-left-two-right manner, the values of $\mathcal{O}_p$ remain invariant. Hence the system stays at the lowest energy state after this operation. Two examples are illustrated in Fig. 2.6a,2.6b.

A single fracton excitation is created by changing the sign of only one operator $\mathcal{O}_p$. To do so, choose two pentagon-edge geodesics intersecting at the target, which divide the lattice into four parts, then flip one of the four. The target cluster then has one spin flipped, while all the others have either zero, two, or four spins flipped. Hence a single fracton excitation is created as illustrated in Fig. 2.6c. It is a topological excitation in the limit $N_g \to \infty$ in the sense that local (i.e., finite number of) spin flipping can not create a single fracton. Same as the case of the flat lattice model, it is immobile in the system since no local operation can move it without creating more fractons.

Similar procedures can be taken to generate two-, three-, and four-fracton bound states, which are also topological. The two-fracton bound state is illustrated in Fig. 2.6d. However, they do not have enhanced mobility in a submanifold like the flat lattice case. This is the consequence of hyperbolic geometry. For example, for the two fracton bound states [Fig. 2.6d], two parallel geodesics as boundaries of the flipped spin region do not keep their distance constant, so there is not a well defined "direction" to propagate for the bound state. Similar logic applies to other bound states too.

The five-fracton bound state is the first local excitation, created by a single spin flip. It can move freely on the lattice by local spin flipping, similar to the four-fracton bound state on the flat lattice. A five-fracton excitation is shown in Fig. 2.6e.

2.5 Rindler Reconstruction of the Hyperbolic fracton model

After describing the basic features of the hyperbolic fracton model, let us start studying the holographic properties realized. The first key holographic property of this model is the *AdS-Rindler reconstruction* or *subregion duality*. In our classical model, its simplified version becomes:

Property 1. For a given spin configuration on a connected boundary segment, the bulk spins can be reconstructed if and only if the minimal convex wedge of the boundary segment covers the bulk sites.

Here, the minimal convex wedge is essentially the geodesic wedge modified by the discretization of the hyperbolic disk. In many scenarios they are degenerate. The precise definition of minimal convex wedge will be made clear as we progress. This property holds for the ground state, and also for excited states if the locations of fractons within the minimal convex wedge are known.

We start with the simple case in which the entanglement wedge is covered exactly by a pentagon-edge geodesic, [Fig. 2.7c].

Notice that the four-spin clusters next to the given boundary subregion always contain three boundary spins and one bulk spin. Knowing that the four-spin cluster satisfies $\mathcal{O}_p = 1$ (or -1 if it is known to be a fracton), the bulk site spin value is uniquely

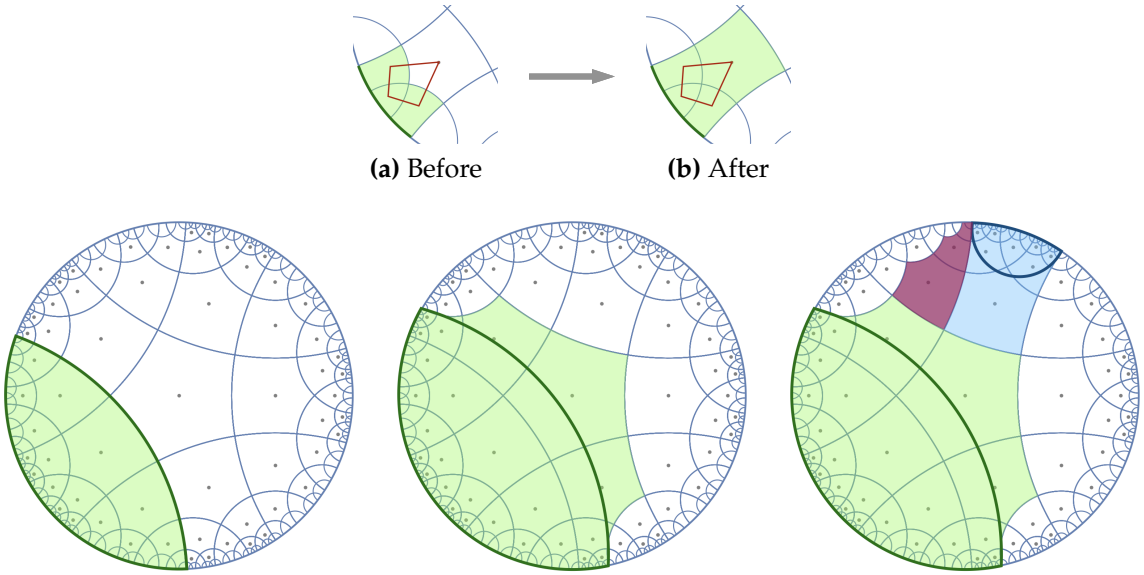

(a) Before **(b)** After

(c) Minimal convex wedge, case one **(d)** Minimal convex wedge, case two **(e)** Minimal convex wedge for disconnected bounday

Figure 2.7: Rindler reconstruction of the hyperbolic fracton model. (a) Before and (b) after views illustrate how the reconstruction works. Given three sites on the boundary (green) and the value of the four-spin cluster (red square) operator [Eq. (2.4)], the fourth one on the same cluster can be reconstructed. (c): For a given boundary segment (boundary arc in dark green), the bulk that can be reconstructed is its minimal convex wedge, the region highlighted in green. In this example the minimal convex wedge ends exactly on a pentagon-edge geodesic. (d): Another example of a minimal convex wedge as the reconstructible bulk. In this example its minimal convex chain is not a geodesic (arc in dark green). (e): An example of Rindler reconstruction for a disconnected boundary subregion. Each connected piece (in green or blue) individually has its own minimal convex wedge, but the collective minimal convex wedge is bigger than the sum of the two individual wedges. The extra segment is colored in magenta. Figure reproduced from Ref. [48].

determined by the three known boundary spins. Thus we can reconstruct all these bulk spins neighboring the boundary spins. This process is shown in Fig. 2.7a, 2.7b.

By doing this procedure to all four-spin clusters next to the boundary subregion, the bulk spins can be reconstructed inward layer by layer. Such procedure comes to an end when the wedge boundary is reached. Beyond the wedge, each four-spin cluster contains at least two unknown spins at the same time, making it impossible to determine their value. This is shown in Fig. 2.7c.

For a generic boundary subregion, its entanglement wedge can be slightly more complicated, as shown in in Fig. 2.7d. In this case, the reconstructible bulk sites are within the *minimal convex wedge*, defined as follows:

Definition 2.5.1. The **minimal convex wedge** for a boundary segment is the bulk re-

gion bounded by a continuous chain of the pentagon's edges that satisfies the following conditions: (1) the chain is homologous to the boundary segment, i.e., shares the same ends; (2) it is a convex; (3) it contains the minimal number of pentagon edges. The chain is named a **minimal convex chain**.

This definition seems to be complicated, but for a connected boundary segment, it is simply the geodesic wedge on the continuous hyperbolic space extended by the pentagons partially overlapping with it:

Property 2. The minimal convex wedge of a connected boundary segment consists of all the bulk sites whose pentagons have non zero overlap with the geodesic wedge in the continuous case.

The shape of minimal convex wedge is simply a consequence of the discretization of the hyperbolic disk, making the minimal bulk volume unit a pentagon.

We also consider the case of a boundary subregion consist of two disconnected components. In this case the entanglement wedge of the total boundary subregion can be larger than the union of entanglement wedges for each individual component. An example is shown in Fig. 2.7e.

For a large subregion of the boundary, the resulting entanglement wedge approximates the continuous limit. However, for more complicated situations of boundary subregion close to the phase transition point, or consisting of many disconnect components, the entanglement wedge is usually very complicated. Such deviation is similar to the situation of holographic tensor networks built from perfect tensors [13].

2.6 Mutual information of the hyperbolic fracton model

The second essential property of holography realized by the hyperbolic fracton model is the Ryu-Takayanagi formula (RT formula) for mutual information.

In the AdS/CFT duality, there exist a geometric descriptions on the bulk side for at least the static states of the boundary CFT at low energies. For such states, the Ryu-Takayanagi (RT) formula claims that the entanglement entropy S_A between a boundary subregion A and its complement A^c is equivalent to the area of its minimal covering surface γ_A in the bulk,

$$S_A = \frac{\text{Area}(\gamma_A)}{4G_N} , \tag{2.22}$$

where G_N is Newton's constant, and $\text{Area}(\gamma_A)$ is to the area of the covering co-dimension 2 surface(s). For a AdS_2 spacial slice, γ_A is a curve (or several curves) and $\text{Area}(\gamma_A)$ is the length of the curve(s). For the simplest case of connected A, γ_A is the geodesic ending on end points of A. We now show that its classical analog is valid for the hyperbolic fracton model.

To make the statement more accurate, a few comments are in order. First, a classical model has no quantum entanglement. So instead of the entanglement entropy, the quantity calculated here is the *mutual information*. It can be viewed as the classical analog of the entanglement entropy as we will explain later. Second, due to the discretization of the hyperbolic disk, the minimal covering curve should be modified to be the boundary of the minimal convex wedge in the bulk, which we have named *minimal convex chain*.

2.6.1 Mutual information as the classical analog of entanglement entropy

The mutual information, as suggested by its name, measures the amount of information shared between two subsystems. It is defined as

$$I_{\mathrm{cl}}(A;B) = S_{\mathrm{s}}(A) + S_{\mathrm{s}}(B) - S_{\mathrm{s}}(A \cup B)\ , \tag{2.23}$$

where A, B are the subsystems, and S_{s} is the Shannon entropy. $S_{\mathrm{s}}(A \cup B)$ is the entropy for the union of the two subsystems. The subscript "cl" is denote that that it is a classical concept.

The mutual information is the proper classical analog of the entanglement entropy for a quantum system. To see why, one can replace the classical Shannon entropy S_{s} by von Neumann entropy S_{v} for the corresponding subsystem's reduced density matrices. If $B = A^c$ is the complement of subregion A, then we have a quantity

$$I_{\mathrm{qu}}(A;A^c) = S_{\mathrm{v}}(A) + S_{\mathrm{v}}(A^c) - S_{\mathrm{v}}(A \cup A^c). \tag{2.24}$$

For a pure state

$$S_{\mathrm{v}}(A \cup A^c) = 0, \tag{2.25}$$

$$S_{\mathrm{v}}(A) = S_{\mathrm{v}}(A^c), \tag{2.26}$$

we end up with exactly twice the entanglement entropy between A and A^c,

$$I_{\mathrm{qu}}(A;A^c) = 2S_{\mathrm{v}}(A) = 2S_A\ , \tag{2.27}$$

which indicates that its classical analog I_{cl} is the correct choice, up to a factor of 2.

2.6.2 Mutual information between two connected subregions

Now let us calculate the mutual information for a bipartition of the boundary. We start with the simple case in which the subregion A is connected. We can show the following property is true:

Property 3. For both the vacuum and a given configuration of fractons (i.e., the positions of fractons are known), the mutual information for a bipartition of the boundary into connected subregions obeys the Ryu-Takayanagi formula

$$I_{\rm cl}(A;A^c) \approx k_{\rm B}\log 2|\gamma_A| \ . \tag{2.28}$$

where $|\gamma_A| = \text{Area}(\gamma_A)$ is a short hand notation.

To compute Eq.(2.23), we need to evaluate the entropies for A, A^c, and the entire system individually. The entropy of the entire system is already given in Eq.(2.21), which is proportional to the number of pentagon-edge geodesics plus one. The physics behind this formula is that, for each pentagon-edge geodesic the number of ground states is multiplied by two, from the operation of flipping spins on either side of the geodesic. This is shown in Fig.2.8.

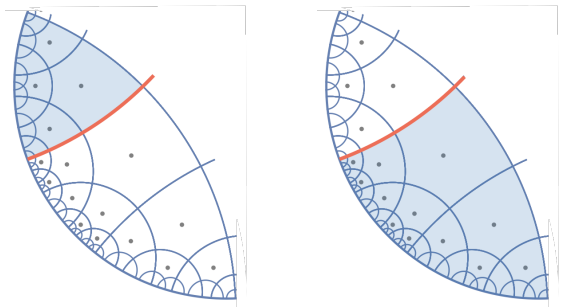

(a) **(b)**

Figure 2.8: Counting the entropy of a subsystem. Every pentagon-edge geodesic crossing the system multiplies the degeneracy by two. These new states can be explicitly constructed as illustrated by (a) and (b), where the blue region indicates the spins being flipped. Figure reproduced from Ref. [48].

The same physics applies to counting the ground state degeneracy of any connected subregion (for disconnected region it can be more complicated). In our case, it will be counting the pentagon-edge geodesics that attach to A with one or both ends. Thus the degeneracy and entropy for the ground states of a subregion A are

$$\Omega(A) = 2^{N_{\text{g-A}}+1} \ , \tag{2.29}$$

$$S_{\rm s}(A) = k_{\rm B}\log\Omega = k_{\rm B}\log 2 \times (N_{\text{g-A}}+1) \ , \tag{2.30}$$

where $N_{\text{g-A}}$ is the number of pentagon-edge geodesics that cross the region.

Let us denote the minimal convex chain as γ_A. As we discussed, depending on the shape of subregion A, γ_A may overlap with a pentagon-edge geodesics exactly, or has some "corners" as a minimal convex chain, as shown in Fig.2.7c,2.7d.

Case one: γ_A is a pentagon-edge geodesic: In the first case, we can classify the $N_{\rm g}$ number of pentagon-edge geodesics into four categories:

1. Those with both ends on A, whose number is denoted $N_{\text{g-A}}$;
2. Those with both ends on A^c, whose number is denoted $N_{\text{g-Ac}}$;
3. Those with one end on A and the other on A^c, whose number is denoted $N_{\text{g-}\gamma}$;
4. The geodesic γ_A. Its length is exactly $|\gamma_A| = N_{\text{g-}\gamma} + 1$.

These quantities satisfy the condition

$$N_{\text{g-A}} + N_{\text{g-Ac}} + N_{\text{g-}\gamma} + 1 = N_{\text{g}}. \tag{2.31}$$

For the ground state or any given configuration of fracton excitations, the entropy of states in region A is

$$S_{\text{s}}(A) = (N_{\text{g-A}} + N_{\text{g-}\gamma} + 1)k_{\text{B}} \log 2 \,, \tag{2.32}$$

as argued in Eq. (2.29,2.30). Similarly, for region A^c we have

$$S_{\text{s}}(A^c) = (N_{\text{g-Ac}} + N_{\text{g-}\gamma} + 1)k_{\text{B}} \log 2 \,. \tag{2.33}$$

Therefore the classical mutual information is

$$I_{\text{cl}}(A;B) = N_{\text{g-}\gamma} k_{\text{B}} \log 2 \approx k_{\text{B}} \log 2 |\gamma_A| \,, \tag{2.34}$$

Here we take the length of the edge of the pentagon to be 1. This calculation is illustrated in Fig. 2.9.

Note that here, compared to Eqs. (2.21, 2.40), a factor of $\frac{1}{2}$ is missing. But it is simply due to the fact that by definition I_{cl} is twice the entanglement entropy [Eq. (2.27)].

Case two: γ_A is not a pentagon-edge geodesic: Now let us consider more general situations when γ_A is not a pentagon-edge geodesic. The proof is basically the same, but we just write it down for completeness. We have the N_{g} pentagon-edge geodesics now classified into three categories:

1. Those with both ends on A, whose number is denoted $N_{\text{g-A}}$;
2. Those with both ends on A^c, whose number is denoted $N_{\text{g-Ac}}$;
3. Those with one end on A and the other on A^c, whose number is denoted $N_{\text{g-}\gamma}$.

Here a geodesic that starts and ends on A is considered to be in the first category, and vice versa for A^c. These numbers obey the modified constraint

$$N_{\text{g-A}} + N_{\text{g-Ac}} + N_{\text{g-}\gamma} = N_{\text{g}} \,. \tag{2.35}$$

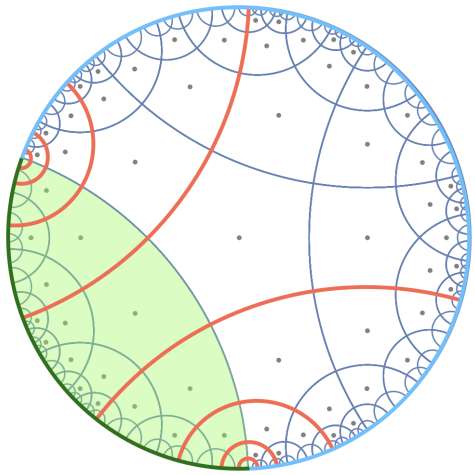

Figure 2.9: Mutual information as a classical analog of entanglement entropy obeys the Ryu-Takayanagi formula. It is measured by the number of pentagon-edge geodesics that are shared by A (dark green arc) and A^c (light blue arc). The subregion-crossing pentagon-edge geodesics are highlighted in orange, whose number is denoted $N_{\text{g-}\gamma}$. They are also the geodesics that intersect with the geodesic γ_A, which is the minimal curve that splits A and A^c. Their relation $|\gamma_A| = N_{\text{g-}\gamma} + 1$ leads to the Ryu-Takayanagi formula for mutual information in Eq. (2.28). Figure reproduced from Ref. [48].

The different entropies remain the same as defined in Eqs. (2.32, 2.33). Therefore the classical mutual information becomes

$$I_{\text{cl}}(A;B) = (N_{\text{g-}\gamma} - 1)k_{\text{B}} \log 2, \tag{2.36}$$

for large $N_{\text{g-}\gamma}$.

Let us denote the number of corners of γ_A as N_{cor}; then

$$I_{\text{cl}}(A;B) = (N_{\text{g-}\gamma} - 1)k_{\text{B}} \log 2 \approx k_{\text{B}} \log 2(|\gamma_A| - N_{\text{cor}}). \tag{2.37}$$

Here $-N_{\text{cor}}$ is a correction to the RT formula, which stays fixed as the lattice size grows. It is, however, in some sense "benign." The lattice discretized minimal convex chain γ_A has some sharp corners. As a consequence, its length becomes larger than the continuous covering geodesic. The $-N_{\text{cor}}$ reduces such deviation, resulting in a mutual information closer to the continuous case.

2.6.3 Mutual information between disconnected subregions

The situation becomes more complicated for a subregion with several disconnected components. Equation (2.23) can still be computed for each subregion by identifying its entanglement wedge and computing its entropy. Here we analyze the possible correction to the simplest case of disconnected subregion A.

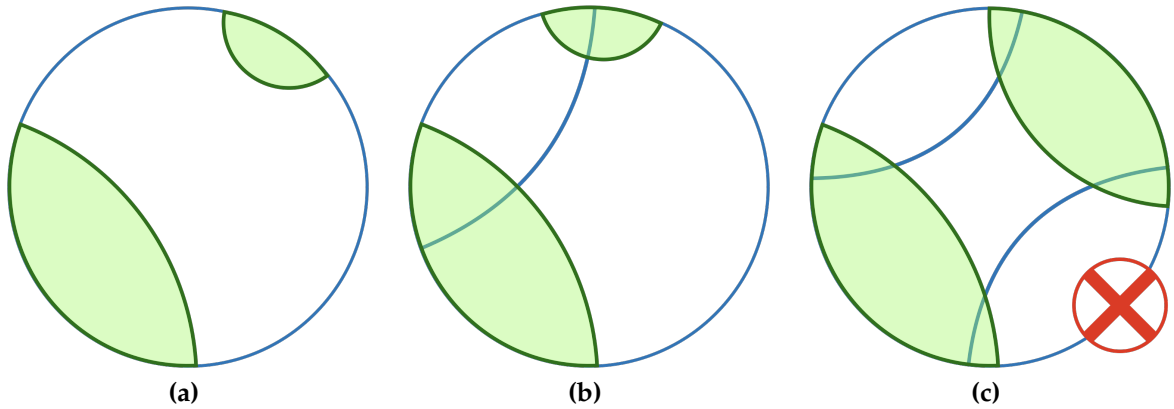

Figure 2.10: Possible configurations for disconnected boundary subregion. Here we limit ourselves to the case when the entanglement wedges (green region) are covered by pentagon-edge geodesics exactly. Blue arcs are pentagon-edge geodesics. Situation (a) and (b) are possible, and (b) will cause one bit of correction to the RT formula for the mutual information. The situation in (c) is impossible as the four pentagon-edge geodesics cannot form a square. Figure reproduced from Ref. [48].

The simplest case is defined as follows: for each component of A, its entanglement wedge is *case one* discussed above; i.e., it is covered by a pentagon-edge geodesic. The mutual information can be again computed by counting the pentagon-edge geodesics.

One issue may lead to some corrections to the mutual information: There are geodesics starting from one component of A and ending in another, instead of ending in A^c. This is shown in Fig.2.10. We have to consider the correction contributed by them.

First we note that between two components, there can be at most one pentagon-edge geodesic. That is, situations in Fig.2.10c do not exist. This is because there is a rectangle formed by these pentagon-edge geodesics, whose four angles are all $\pi/2$. Such rectangles cannot exist in the hyperbolic space.

So we only need to take care of the case with one pentagon-edge geodesic between the two components. Note that it still goes through the entanglement wedge of A^c and contributes one unit of entropy to S_{A^c}. So it contributes one unit of mutual information, but two units of the length of the minimal covering chain. Therefore, the final correction is one unit:

$$I_{\mathrm{cl}}(A; A_c) = (N_{\text{g-}\gamma} - 1)k_{\mathrm{B}} \log 2 \approx k_{\mathrm{B}} \log 2(|\gamma_A| - N_{\text{A-A}}), \tag{2.38}$$

where $N_{\text{A-A}}$ denotes the number of geodesics starting from one component of A and ending in another.

As the boundary subregion becomes more complicated, more corrections will enter the mutual information. In particular, for configurations close to the phase transition of entanglement entropy, the deviation can be big. Similar issues with the holographic tensor-networks are fixed by the random tensors [17]. It remains an open question

on how the modifications of the hyperbolic fracton model will amend such issue and yield exact RT formula for arbitrary boundary bipartition.

2.7 Naive black holes in the hyperbolic fracton model

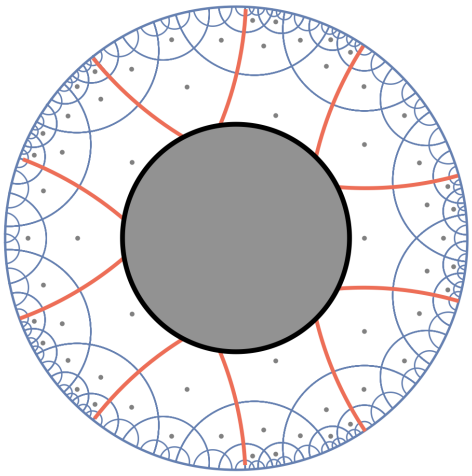

Figure 2.11: A naive black hole in the hyperbolic fracton model. There is no geometrical change of the hyperbolic disk, but some bulk sites are hidden behind the horizon, and not accessible by observers. The horizon is the solid black line. The pentagon-edge geodesics crossing the black hole are highlighted in orange. Figure reproduced from Ref. [48].

The black hole in this model has its entropy proportional to its horizon. Here we consider a very naive black hole constructed by simply cutting out some bulk pentagons included in a closed convex, but leaving the rest of the lattice unchanged. The spins of the pentagon inside the black hole, and all interactions associated with them, are considered hidden behind the horizon. An example is illustrated in Fig. 2.11. Our approach is adapted from Ref.[13], in which a black hole is constructed by removing some bulk tensors in the holographic tensor network. Though there is no change of geometry outside the horizon, this approach does show some resemblance to a black hole in an asymptotic AdS geometry, as we demonstrate below.

The horizon size of the black hole is approximately

$$\text{Horizon area} = N_{\text{BH}} \,, \tag{2.39}$$

where N_{BH} is the number of semi-infinite pentagon-edge geodesics extended from the black hole, highlighted in orange in Fig. 2.11. They used to be $N_{\text{BH}}/2$ complete geodesics.

The black hole entropy has several interpretations, including the entropy for its microstates, or its entanglement entropy with the outside. Here we use the definition proposed by Witten [5], tailored for our model:

Definition 2.7.1. The **black hole entropy** is the boundary or bulk ground state Shannon entropy increase from introducing the black hole.

This is a rather simple calculation: since $N_{\mathrm{BH}}/2$ pentagon-edge geodesics are cut into two pieces, the system has effectively $N_{\mathrm{BH}}/2$ more pentagon-edge geodesics for the topological spin-flipping operations to create new ground states. Therefore we have the following:

Property 4. The black hole entropy is

$$S_{\mathrm{BH}} = \frac{k_{\mathrm{B}} \log 2}{2} N_{\mathrm{BH}} = \frac{k_{\mathrm{B}} \log 2}{2} \times (\text{Horizon area}) \,, \tag{2.40}$$

which has the proper scaling behavior.

The appearance of a black hole means the boundary ground state degeneracy grows, similarly to the Hilbert space enlargement discussed in Ref. [13]. This is expected as only a very small portion of the boundary states correspond to the pure AdS geometry, and most states corresponds to some black hole state in the bulk.

2.8 Generalizations: higher dimension and quantum version

Two important questions naturally follow the major results of this work: The first question is how to generalize the model to higher dimension. The second one is whether there is a quantum version of the model. The answers to both questions are positive, as we explain below.

2.8.1 Three-Dimensional generalization

The three-dimensional generalization of our model is a cubic Ising model with eight-spin interaction terms.

In this model, each Ising spin sits at the *center* of the cube of the lattice, as shown in Fig.2.12. The operator $\mathcal{O}_c$ is

$$\mathcal{O}_c = \prod_{i=1}^{8} S_i^z, \tag{2.41}$$

where i runs over 8 cubes sharing the same corner, which forms the cube of the dual lattice. The Hamiltonian is again

$$\mathcal{H}_{\mathrm{cl}} = -\sum_c \mathcal{O}_c, \tag{2.42}$$

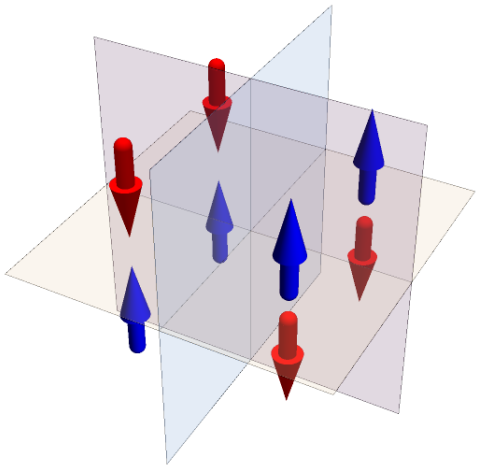

Figure 2.12: Building block of 3D classical fracton model [Eq.(2.42)]. The spins sit at the centers of the cube, and eight cubes sharing the same corner are used to construct the operator $\mathcal{O}$ in Eq.(2.41).The subsystem symmetry is flipping a line of spins in the $x-$, $y-$ or $z-$ direction. Figure reproduced from Ref. [48].

where c runs over all the eight-spin operators.

This classical model has the subsystem symmetries of flipping all spins on a line in the $x-$, $y-$ or $z-$ direction. An equivalent way to view them is to have two perpendicularly intersecting planes. The two planes divide the lattice into four parts, and flipping one quadrant of the spins leaves the energy invariant. This way has a more straight forward adaptation to the AdS_3 lattice.

This model has a natural generalization to the AdS_3 space. We do not need to visualize the entire lattice, which is rather difficult. Instead we can focus on the subsystem symmetries, and it would be sufficient to demonstrate the holographic properties.

In its AdS_3 lattice, the original 2D planes become spherical surfaces that intersect the boundary of AdS_3 perpendicularly. These intersecting 2D hypersurfaces form cells for the spins to sit in. Every cluster of eight cells share the same corner since three spherical surfaces intersect at the same point, which can be used to build the same Hamiltonian for each local 8-spin cluster.

Each geodesic is now determined by two intersecting spherical surfaces, and they split the entire lattice into four parts as shown in Fig.2.13, in analogy to each geodesic splitting the AdS_2 lattice into two parts. Flipping spins in one of the four parts keeps the energy of the system invariant, which is the subsystem symmetry in AdS_3 space. Again the number of independent subsystem symmetries is proportional to the number of geodesics, hence the boundary area.

The Rindler reconstruction and RT formula for mutual information holds as a consequence of the structure of the subsystem symmetries.

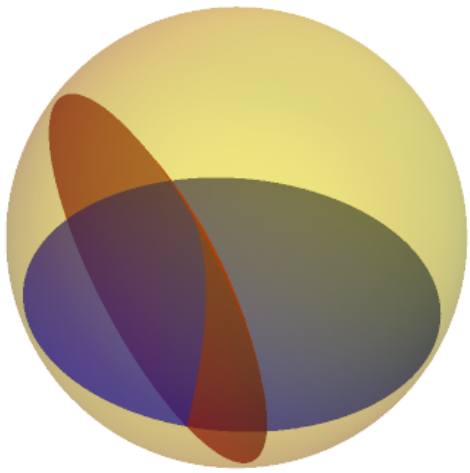

Figure 2.13: Subsystem symmetry of the fracton model [Eq.(2.42)] in AdS_3 space. The spherical surfaces (red and blue) in this representation are actually "flat" in the AdS_3 space. The two surfaces split the entire AdS_3 lattice into four parts. Flipping spins in one part of the AdS_3 lattice does not change the system's energy, and is a subsystem symmetry. Figure reproduced from Ref. [48].

2.8.2 Quantum Model with a Transverse Field

Next let us make some remarks on the quantum version of the model. The simplest case is to introduce a constant transverse field. For a small transverse field, we can assume that there will be a unique quantum ground state as the superposition of (almost) all classical ground states. The superposition does not necessarily have to have equal weight or phase.

The boundary state is then defined as a mixed state by tracing out all degrees of freedom in the bulk, and such mixed state can be viewed as an ensemble of all classical ground states on the boundary with a certain probability distribution. Assuming the probability distribution (or weight of the superposition) to be close to even among all classical states for a small transverse field, the entanglement entropy/mutual information will still obey the Ryu-Takayanagi formula up to some correction. If a bulk spin is fixed by hand to be up or down in the model, it can be reconstructed by looking at any element from the ensemble on a region whose entanglement wedge covers the bulk site. It is not too different from the classical model in the sense that on the boundary one always works with a classical ensemble.

We have to point out that this is an interesting difference from the large-N limit of gravity/CFT duality. There, the bulk is semiclassical and the boundary is quantum, which is the opposite of our construction. Whether such difference has any profound meaning is to be studied in the future.

2.9 Comparison with the holographic tensor-networks

A key question emerging from this work is , what features of gravity can be captured by the fracton models, and what cannot? To pave the way to the answer, it is useful to compare our model with holographic tensor networks regarding their holographic properties. These models are, after all, not exactly quantum gravity, so some properties of AdS/CFT duality are still not captured. Clarifying them can be helpful for future investigations and improvements.

Holographic tensor networks are a type of toy model of holography [13, 14, 16, 17]. They are built by tensors with special properties, and uniformly tiled on the discrete hyperbolic lattice. Two representatives are the perfect tensors and the random tensors. Essentially, these tensors saturate the upper bond of entanglement between any bipartition of their legs. This guarantees that the bulk information is not lost when "pushed" toward the boundary. It is closely related to the quantum-error-correcting properties of gravity, which manifest in the Rindler reconstruction and the RT formula for the entanglement entropy.

Let us focus on the holographic *state* defined by the tensor networks, i.e., simply a quantum state on the boundary without bulk inputs. For the holographic state, we care about the boundary state's entanglement properties, mainly the Renyi entropy for connected or disconnected subregions. The exact RT formula for any disconnected subregion is realized in the random tensor network in its large-N limit [17]. The hyperbolic fracton model, however, suffers from various corrections as we explained in previous sections.

Both the tensor network model and the hyperbolic fracton model have a trivial $n-$dependence for the $n-$th Renyi entropy. More fundamentally this is due to the fact that the entanglement spectrum is always flat in such models. In contrast, the CFT has a nontrivial $n-$dependence and a nonflat entanglement spectrum [117, 118]. A related issue is that the boundary state defined by the holographic code cannot be the ground state of a local Hamiltonian. Refinement of such undesirable properties will be an important progress.

Finally we point out an issue for the hyperbolic fracton model that does not exist in the tenser-network models. Let us consider two small boundary subregions denoted A and B, and examine their mutual information when A and B are far apart. The two subregions should not have any mutual information according to AdS/CFT, which is the case in the tensor-network models. In the hyperbolic fracton model, this is also true for most choices of A and B. However, there will be one bit of mutual information when A and B cover the two ends of the same pentagon-edge geodesic. Such a choice is illustrated in Fig. 2.14.

Such issue has to do with the subsystem symmetry being "rigid"; that is, the pentagon-edge geodesics are fixed in the model.

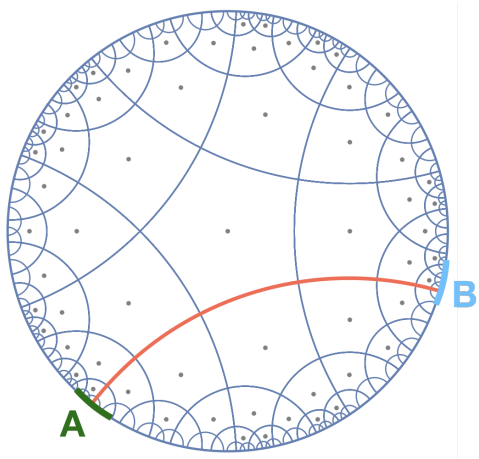

Figure 2.14: An example of subregions A, B with non-vanishing mutual information. Figure reproduced from Ref. [48].

The ground states of most gapped fracton models actually have a stabilizer map description as discussed in Refs. [29, 97, 99, 119, 120]. Many of the holographic tensor networks are also built from "perfect" stabilizer tensors, although the construction is different. The "perfect" stabilizer tensor may lend us some insight on how to modify the hyperbolic fracton model for improved realization of AdS/CFT properties.

2.10 Outlook

Modern physics has witnessed increasing interactions between high energy theory, many-body physics, and quantum information. This chapter adds another example at this trisection, by elaborating the holographic properties of a classical fracton model. After an introduction of the fracton model accompanied by a discussion of various hints of its similarity with gravity, we demonstrate that when defined on a hyperbolic disk, it satisfies some key properties of AdS/CFT, including the Rindler reconstruction/subregion duality and the RT formula for its mutual information. A naively defined black hole in this model also has the correct entropy. Some generalizations and comparisons with tensor-network toy models are also discussed.

This work expands the scope of the application of holography in condensed matter physics. Not only can one study a strongly coupled/critical system as the CFT side of AdS/CFT; there are also states of matter that exhibit meaningful physics on the AdS side. In particular, it may be interesting to examine other fracton models in AdS space, and classify them by their holographic properties.

A long-term ambition we initiate with this work is to concretely understand what exactly are the similarities and differences between various fracton models and quantum gravity. In return it may help us study how quantum gravity or related many-body models can perform quantum error correction encoding, which is one of the most

intriguing quantum information aspect questions of gravity. We may be able to partially achieve this by quantitatively examining the speculated web of connections in Fig. 2.4. Some works on fracton models [120] suggest that studying a quantum, lattice version of Higgsed linearized general relativity (or a higher-rank gauge theory) and constructing the tensor-network representation of its ground state are possible. A reasonable approach could be to explore its connections to holographic tensor networks discussed in Ref. [13, 17].

Some questions remain open even for the classical model, especially concerning the subregion duality and mutual information for more complicated, disconnected boundary segments.

The higher-rank gauge theory is also interesting in its own right, and it remains to be understood whether it is holographic without being Higgsed into gapped fracton models, at both the classical and quantum level. A recent development has already shown that some versions of the theory can be consistently defined on a constant-curvature manifold [114, 121].

Another direction for future investigation is to study other gapped fracton models protected by different types of subsystem symmetries, or the fracton topological orders obtained by gauging these symmetries. It is desirable to know what are the necessary and sufficient conditions for a model to be holographic, and also construct some of them explicitly.

To conclude, certain fracton models give rise to some interesting physics that mimics general relativity. In this chapter we pointed out the holographic aspect of this, and hope further investigation could provide useful insight for both the condensed-matter and high-energy theory communities.

Chapter 3

The Dual Eight-Vertex Model and Bit Threads

3.1 Introduction

In the previous chapter, a very simple classical fracton toy model in anti-de Sitter space was shown to satisfy a few major holographic properties [48]. These properties include the Ryu-Takayanagi formula for the boundary entanglement entropy[22, 23], and also the subregion duality [122]. Its construction has a lot of similarities to the holographic toy models built from tensor networks [12–18].

This chapter, as the second piece of the three on the hyperbolic fracton model, studies the dual eight-vertex model of the original model, which has the advantage of visualizing the mutual information and subsystem fluxes.

It helps to address a few key unanswered questions following the initial discovery. One question is whether the hyperbolic fracton model is equivalent to any other known holographic models/theories. This turns out to be true. The dual eight-vertex model is a discrete realization of the bit-thread model [19–21, 123, 124].

The bit-thread model was originally proposed as a powerful framework to understand holography. This model treats the non-local "flow of information" instead of local fields as the elementary physical quantity. From this perspective many holographic properties of entanglement entropy have an intuitive, pictorial derivation.

Another question is about holography beyond the ground states. This was not discussed much in the previous chapter. Here equipped with the bit-thread picture and the concept of subsystem charges, a detailed analysis is presented. We show that "isometry", the requirement from holography that the boundary uniquely determines the bulk, is violated only by a small amount at low energy levels, and all violating cases can be determined.

The bit-thread and subsystem charge language also help us to identify the black hole microscopic degrees of freedom (dofs), which is encoded non-locally on the horizon, and also the AdS boundary. Intriguingly even though the black hole set-up is very primitive, it yields qualitatively correct behavior of how a boundary observer can distinguish the microstates [125].

These two chapters form a relatively comprehensive investigation of the classical toy hyperbolic fracton model. In the outlook, we discuss future directions beyond this simple toy model, which could be an interesting program for condensed matter physics, and hopefully provide some insights in high energy theory, too.

This chapter is arranged as follows: Sec. 3.2 describes the dual eight-vertex model on the Euclidean lattice and Sec. 3.4 on the hyperbolic lattice.

The first major result of this chapter, Sec. 3.5 builds the duailty between the eight-vertex model and the Ising fracton model. It then explains what is the bit-thread model and how the eight-vertex model is a realization of it. It is then utilized to derive results documented in the two following sections: Sec. 3.6 analyzes the isometry properties of the excited states; Sec. 3.7 describes the black hole microscopic degrees of freedom in the model.

Finally Sec. 3.8 summarizes this chapter and gives an outlook of possible future directions.

3.2 Dual Eight Vertex Model on the Square Lattice

The main results of this chapter revolve around a physically equivalent model of the hyperbolic fracton model introduced in previous chapter— the dual eight-vertex model. Formulated in the language of arrows and vertices, it has the advantage of illuminating various connections between the hyperbolic fracton model and other established results in fracton phases and holography. In this section, we will describe the dual eight-vertex model, and discuss how it works as a straightforward demonstration of fracton-elasticity duality [100, 121, 126] and subsystem charge [101].

The square-lattice eight-vertex model is a canonical exactly solvable model [106, 127–130]. It is constructed by placing a binary arrow (left/right or up/down) on every edge of the square lattice, but only allowing vertex configurations of even number of arrows pointing in/out. The eight allowed vertex configurations are shown in Fig. 3.1. Under open boundary condition, each vertex can be independently assigned an energy cost E_i $(i = 1, ..., 8)$ in the most generic case. Specifying E_i completes the definition of the classical model.

The eight-vertex model can be reformulated as an equivalent spin model that involves up to four-spin interactions [106]. The classical fracton model (Eq. (2.5)) described in Chap. 2 is a special case of the more general equivalence. The prescription of the

vertex	1	2	3	4	5	6	7	8
winding number N_w	0	0	0	0	1	1	-1	-1
net flux C_n	0	0	0	0	4	-4	0	0
flux in x-direction C_x	0	0	0	0	2	-2	2	-2
flux in y-direction C_y	0	0	0	0	2	-2	-2	2

Figure 3.1: Vertex configurations in eight-vertex model and their winding numbers around the vertex center, total fluxes and fluxes in $x-$ and $y-$directions. Figure reproduced from Ref. [131].

duality is given below.

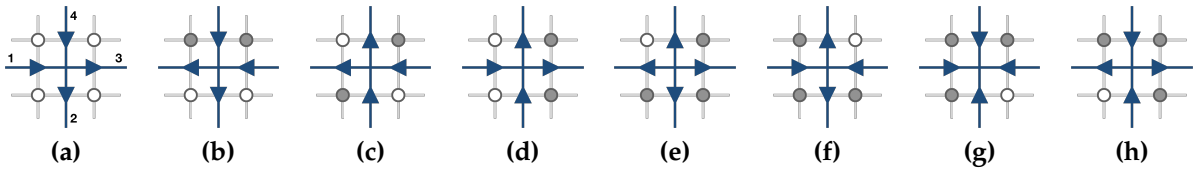

Figure 3.2: Mapping between the spin configurations and the vertices. (a-d): Spin configurations of ground states $\mathcal{O}_p = 1$ correspond to vertices with zero winding number. Their energy cost is $E_i = -1$. (e-h): Spin configurations of Fractons $\mathcal{O}_p = -1$ correspond to vertices with winding number ± 1. Their energy cost is $E_i = +1$. The correspondence is two-to-one, since flipping all spins maps to the same vertex. Figure reproduced from Ref. [131].

The eight-vertex model is defined on the dual square lattice of the original fracton model. The mapping between the arrow and spin configurations is illustrated in Fig. 3.2. Each edge of the dual lattice neighbors two spins of the original lattice, at the ends of the perpendicularly intersecting edge. The arrow of the dual edge points right or down if the two spins are aligned in the same direction, and left or up otherwise. Such assignment guarantees that any four-spin configuration is mapped to one of the eight vertices listed in Fig. 3.1. The mapping has a global two-fold degeneracy: the vertices remain the same after flipping all spins.

The dual Hamiltonian for the eight vertex model is

$$\mathcal{H}_{\mathsf{EV}} = -\frac{1}{2}\sum_{v}(\sigma_1\sigma_3 + \sigma_2\sigma_4). \tag{3.1}$$

Here v denotes all vertices in the dual lattice, and σ_i is the value of arrows on edge i, defined as

$$\sigma_i = \begin{cases} 1 & \text{if it points right or down;} \\ -1 & \text{if it points left or up.} \end{cases} \tag{3.2}$$

The assignment of subscripts $1, 2, 3, 4$ around a vertex is shown in Fig. 3.2a. Note that this is *not* equivalent to a collection of non-interacting, 1-dimensional spin chains, since the constraint of eight-vertex configuration is enforced.

The vertices of winding number zero (cf. Fig.3.1) correspond to the ground-state spin configurations of

$$\mathcal{O}_p = 1, \tag{3.3}$$

and have energy cost

$$E_i = -1 \ , i = 1, 2, 3, 4. \tag{3.4}$$

Those of winding number ± 1 correspond to the spin configurations of

$$\mathcal{O}_p = -1, \tag{3.5}$$

and have energy cost

$$E_i = +1 \ , i = 5, 6, 7, 8 \ , \tag{3.6}$$

which agree with the original fracton model (Eq. (2.5)). The prescription of the duality is concluded here.

The dual eight-vertex model has the advantage of illustrating various concepts of fracton models.

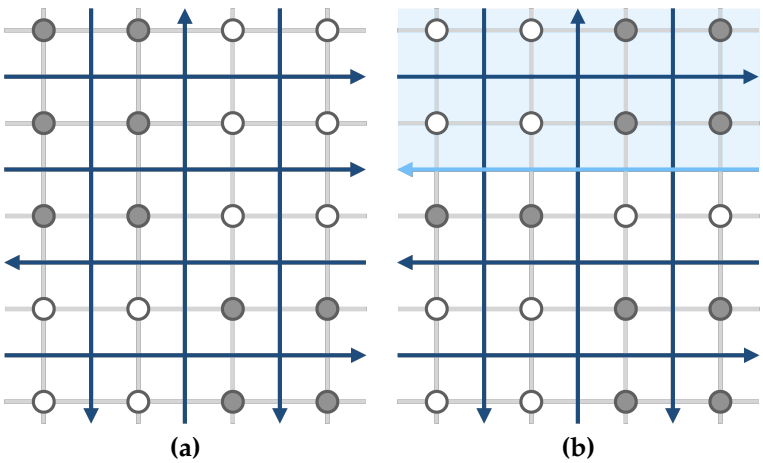

Figure 3.3: Ground state degeneracy in the two dual models. (a): A spin configuration of ground state, and its dual eight-vertex model state. In the eight-vertex model the ground state is such that all arrows on the same line align in the same direction. (b): Another spin configuration of ground state, obtained from (a) by flipping all spins in the light-blue shaded area. In the dual eight-vertex model it corresponds to flipping a line of arrows. Figure reproduced from Ref. [131].

Firstly let us examine the ground state degeneracies. In the dual eight-vertex model, the ground states become very simple: all arrows on the same straight line have to align in the same direction. The action of flipping all spins on one side of a straight line corresponds to flipping the arrows of the entire line. This is illustrated in Fig. 3.3. The

ground state ensemble is thus equivalent to a number of uncorrelated Ising spins on the boundary, which makes it apparent that its entropy is proportional to the boundary area.

Next we turn to the fracton excitations. The dual model illuminates a qualitative difference between the its effective theory — rank-two U(1) gauge theory (the traceless, scalar charged version [32, 33, 35]) — and conventional U(1) gauge theory in two-dimensional space. The rank-two U(1) gauge theory accounts for the topological excitations of non-zero *winding number* N_w of the underlying vector field, while the conventional U(1) gauge theory accounts for the non-zero net flux C_n.

As one can see in Fig. 3.2, the fractons (vertices $5, 6, 7, 8$ in Fig. 3.1), or "charge" of the rank-two electric field, are actually vertices with winding number ± 1. In contrast, in the conventional electromagnetism, the "charge" is the net flux of the underlying electric field, or just the charge as we know it (vertices $5, 6$).

The observation echoes the fracton-elasticity duality [100], where the underlying vector field is the lattice distortion, and disclinations corresponds to a non-zero winding of the distortion [132].

The dual eight-vertex model is also an elegant demonstration of the subsystem symmetries and charges discussed in [31, 101]. Each vertex with fracton excitation will introduce an $x-$ and $y-$ subsystem charge C_x and C_y on the $x-$ and $y-$direction line it is located. The charges are the flux in x and y listed in Fig. 3.1. They are related to the winding number by

$$N_w = \frac{C_x C_y}{4}. \tag{3.7}$$

Two different lines have their independent charges. The total charge of each line, which can be 0 or ± 2, must be conserved by local spin flipping. Therefore a single fracton is completely localized, since moving it will change the subsystem charges. A two-fracton bound state can move in $x-$direction if they give zero charge on the $y-$direction lines. A four-fracton bound state has zero subsystem charge on any line, hence is free to move.

3.3 Connection to rank-2 U(1) theory

In this section, we explain how the fracton model and eight-vertex model can be obtained from the electrostatic sector of a particular version of R2-U1 gauge theory.

The R2-U1 theory is set up as follows: we consider a "hollow", scalar-charged rank-2 U(1) gauge theory in 2D. "Hollow" means the diagonal terms in the electric field matrix are identical to zero. In this case, the tensorial electric field is

$$\mathbf{E} = \begin{bmatrix} 0 & E^{xy} \\ E^{xy} & 0 \end{bmatrix}, \tag{3.8}$$

which has only one degree of freedom. The charge is then defined as

$$\rho = (\partial_x \partial_y + \partial_y \partial_x) E^{xy}, \tag{3.9}$$

and the low energy sector corresponds to

$$(\partial_x \partial_y + \partial_y \partial_x) E^{xy} = 0. \tag{3.10}$$

E^{xy} are placed at the centers of plaquettes on the square lattice, same as the Ising spins in the original fracton model. On each site i, E_i^{xy} takes a $\mathbb{Z}_2$ value $0, 1$. As a consequence, the charge ρ also takes a $2 \times \mathbb{Z}_2$ value $0, 2$.

To build the correspondence between the Ising fracton model and the rank-2 U(1) theory, we map the $\mathbb{Z}_2$ value 0 to -1 in the spin model, and $\mathbb{Z}_2$ value 1 to 1. That is, the Ising spins S_i^z are then identified by the correspondence

$$\begin{aligned} E_i^{xy} = 1 &\to S_i^z = 1 \\ E_i^{xy} = 0 &\to S_i^z = -1 \end{aligned} \tag{3.11}$$

For each four spin cluster as shown in Fig. 3.2a we have

$$\partial_x E^{xy} = E_2^{xy} - E_1^{xy} \ (\mathbb{Z}_2 \text{ value}) \to -S_1^z S_2^z, \tag{3.12}$$

and

$$\rho^2 = \rho = \partial_x \partial_y E^{xy} + \partial_y \partial_x E^{xy} \ (\mathbb{Z}_2 \text{ value}) \to -2 S_1^z S_2^z S_3^z S_4^z. \tag{3.13}$$

Hence the electrostatic sector of the R2-U1 gauge theory and the Ising fracton model are identified.

The correspondence between the eight-vertex arrows and R2-U1 theory is built by

$$\partial_x E^{xy} = E_2^{xy} - E_1^{xy} \ (\mathbb{Z}_2 \text{ value}) \quad \to \quad \sigma_4, \tag{3.14}$$

$$\partial_x \partial_y E^{xy} \quad \to \quad -\sigma_4 \sigma_2, \tag{3.15}$$

$$\partial_y \partial_x E^{xy} \quad \to \quad -\sigma_1 \sigma_3, \tag{3.16}$$

so that

$$\begin{aligned} \rho^2 = \rho = \partial_x \partial_y E^{xy} + \partial_y \partial_x E^{xy} \ (\mathbb{Z}_2 \text{ value}) \\ \to -\sigma_4 \sigma_2 - \sigma_1 \sigma_3, \end{aligned} \tag{3.17}$$

which leads to Eq. (3.1).

This concludes our derivation, and demonstrates that the Ising fracton model is a special case of R2-U1 theory defined on a lattice with $\mathbb{Z}_2$ values.

3.4 Hyperbolic Dual Eight-Vertex Model

The eight-vertex model dual to the hyperbolic fracton model is obtained by simply upgrading the square lattice to the $(5, 4)$ tessellation of the hyperbolic disk. In the

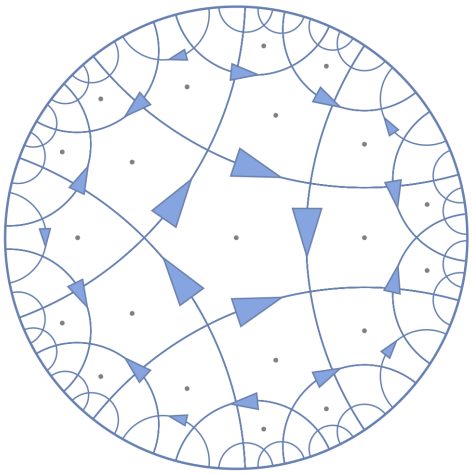

Figure 3.4: Dual eight-vertex model on the hyperbolic disk at $T = 0$. Each geodesic carries an independent binary arrow. This is a discretized realization of the bit-thread model. Figure reproduced from Ref. [131].

dual model, each pentagon's edge has an associated binary arrow, and vertices are still restricted to the eight configurations in Fig. 3.1. Here we assign the arrow directions in the following way: We start from the obvious fracton model ground state of all spins pointing up. We then define the corresponding vertex model configuration is that (1) all arrows on the same geodesic align in the same direction; (2) the arrow on the geodesic flows clock-wise. All other vertex states are fixed following these rules.

For the ground state, all edges on the same geodesic have aligned arrows. Flipping all spins on one side of a geodesic corresponding to flipping its arrow direction. Fig. 3.4 shows one example of ground state eight-vertex model configurations. For fracton excitations, the concept of subsystem charges for each geodesic is also still valid.

3.5 Bit-Thread Realization

When restricted to its ground states, the dual eight-vertex model becomes a collection of geodesics, each associated with a binary arrow. This is a simple discrete and classical realization of the *bit-thread model* proposed in Ref. [19] as a powerful conceptual tool to visualize holography.

In the bit-thread model, the elementary physical object is a divergence-free vector field in the bulk with pointwise bounded norm, referred to as the *flow*. Just as physicists visualize electric/magnetic fields, the flow lines can be viewed as threads. Each thread carries an independent bit of information (or two entangled qubits), and stretches from one boundary point to another. The full-fledged geometric theory of the bit-thread model is able to account for various properties of holographic entanglement entropy. For example, since the covering geodesic of boundary subregion A is the narrowest

bottleneck separating A and its complement A^c, it sets the upper bound of the entanglement entropy between them. Following the max-flow min-cut principle [19], this upper bound is saturated, so that the entanglement entropy obeys the RT formula.

In the eight-vertex model at zero temperature, each geodesic is a thread or discretized flow, and carries the binary arrow as one bit of classical information. The bit threads visualize the mutual information between two subregions. It is simply counted by how many geodesics the two subregions share, as both subsystems can measure the directions of these arrows.

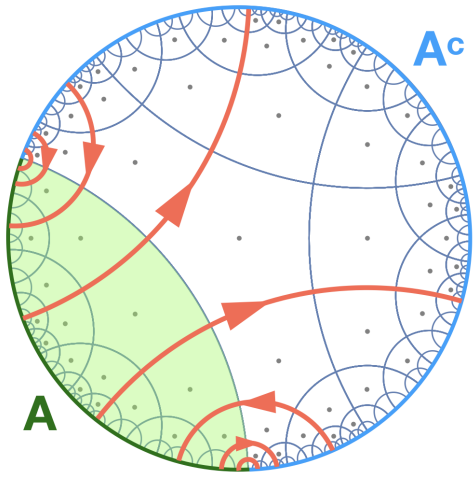

Figure 3.5: Bit-Thread Realization and Ryu-Takayanagi formula for mutual information. Each geodesic is a thread carrying a bit of information. The threads shared between two region (blue and green) saturates the bottleneck between them, i.e., the covering minimal surface. Hence the mutual information obeys the RT formula. Figure reproduced from Ref. [131].

The idea of the minimal covering surface being the bottleneck is clearly represented in the eight-vertex model. As shown in Fig. 3.5, the geodesics highlighted in orange are the threads carrying the mutual information from boundary segment A (green) to its complement A^c (blue). It is straightforward to identify that the minimal covering surface, or the geodesic homologous to A, is the bottle neck of the orange region-crossing threads, which is exactly the picture described in the bit thread model. The flow also satisfy the fine structure of entanglement contour proposed by Wen [133].

In our previous chapter, the RT-formula for a connected boundary subregion was demonstrated. In general, toy models of such type violate RT-formula for a disconnected boundary subregion. Here we can show that for a "nice" n-component boundary subregion, there is an upper limit $n^2 - n$ on the deviation of mutual information from RT-formula. The term "nice" means each component of the boundary region is covered exactly by a geodesic in the lattice (see Fig. 3.6 for an example).

In this case, each component i $(i = 1, ..., n)$ has a covering geodesic γ_i, and $|\gamma_i|$ bit threads crossing the geodesic. If none of the bit threads end up in the boundary subregion, i.e., all the bit threads end up in its complement, then the RT formula is still

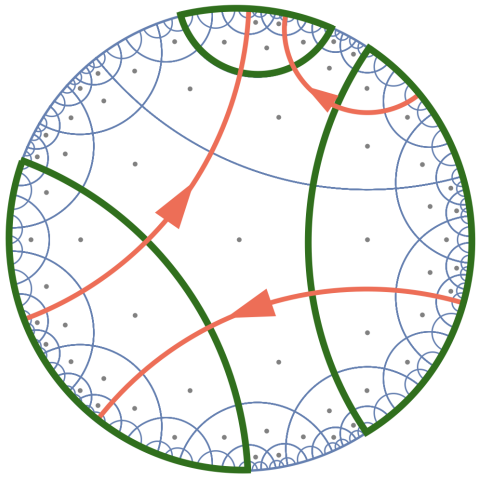

Figure 3.6: An example of RT-formula violation of the mutual information for disconnected boundary subregion. The boundary subregion is chosen to be "nice" as discussed in Sec. 3.5. Figure reproduced from Ref. [131].

satisfied. This situation actually happens depending on the choice of boundary subregion. But it may also happen that a bit thread connects subregion component i and j, so it does not contribute to the mutual information and lead to deviations from the RT-formula.

Note that on the lattice all geodesics intersect perpendicularly. Using the property of hyperbolic geometry that rectangles (four edges with four corners of $\pi/2$) cannot exist, it is obvious that between components i and j there can be at most one intersecting bit thread. So in the worst scenario we may have one bit thread between every two components, which contributes $n^2 - n$ deviation in total (see Fig. 3.6 for an example).

For generic disconnected boundary, the counting becomes much more complicated and often need to be examined case by case. But based on the "nice" case, it seems reasonable to guess that the deviation of mutual information from RT-formula will be at order $\mathcal{O}(n^2)$ for a $n-$component disconnected boundary subregion.

The bit-thread model realization is simple, yet bears some non-trivial implications. We know that the rank-2 U(1) theories are linearized limit of certain gravitational theory [134], and the toy fracton model here is a discretized version of the rank-2 U(1) theories. By studying the field theory and utilizing the duality established here, it might be possible to derive the full bit-thread model from (linearized) gravity. This would be an interesting result for holographers.

Finally, we noticed a recent development yields very similar results. In Ref.[135], Jahn et al. studied the holographic tensor network in the language of majorana dimers, and discovered that the tensor networks have the same picture as we described here — entangled EPR pairs are linked by bit threads that form the hyperbolic lattice. This is a very strong indication of hidden connections between fracton models and holographic tensor networks.

3.6 Bulk-Boundary Isometry for Diluted Fracton Excitations

The isometric property of the mapping between the bulk and the boundary states is crucial for toy models of holography [13, 15–17].

It is necessary to clarify the meaning of isometry in different contexts first. In geometry, an isometry is a mapping of metric spaces that preserves distances. In quantum information, an isometry V is a map from Hilbert space $\mathcal{H}_A$ to $\mathcal{H}_B$ such that $VV^\dagger = I$. Roughly speaking, this means the distinction between two states in $\mathcal{H}_A$ is always preserved when mapped into states in $\mathcal{H}_B$.

In the context of the classical fracton toy models, isometry means a mapping from the boundary states to the bulk states such that two different boundary states are always mapped into two different bulk states, so that the boundary state can unambiguously determine the bulk. It can be rigorously defined as:

Definition: Each spin/vertex configuration of the hyperbolic fracton model includes one boundary and one bulk state, and specifies a mapping from that boundary state to the bulk one. Hence a subset of all possible spin/vertex states defines a map from a subset of boundary states to the bulk states. This subset/mapping is *isometric*, if none of its two elements have the same boundary state.

That is to say, within the chosen subset of all possible spin/vertex states, the boundary state uniquely determines the bulk. Of course, the subset has to be a sensible choice – normally we would expect it to contain many low-energy states. For example, if it is the set of all the ground states, then isometry holds exactly.

If the subset includes certain configurations at higher energies, the isometry will eventually break down. Two examples are given in Fig. 3.7. This means the violation of holography, but is acceptable. Because for toy models, it is often the case that isometry (and thus holography) only holds at low energy. After all, the AdS geometry will be distorted beyond small perturbations by local high energy excitations, which is not captured by the toy models at all.

The question now becomes: how can we include more configurations at higher energy levels but maintain isometry? Or equivalently, if we include all states below a certain energy level, how much is the isometry broken?

To start with, including all single fracton excited states does not break isometry. This is almost obvious, but we still analyze it in the eight-vertex picture to pave way for more complicated situations. As we discussed in Sec. 3.2, each geodesic has its own subsystem charge. A fracton will introduce non-zero subsystem charges to the two geodesics γ_1 and γ_2 it sits on. So the subsystem charge is zero if there are zero or even number of fractons sitting on it, and ± 2 if there are odd number of fractons sitting on it. In the case of a single fracton excitation, by examining the boundary arrows, we can

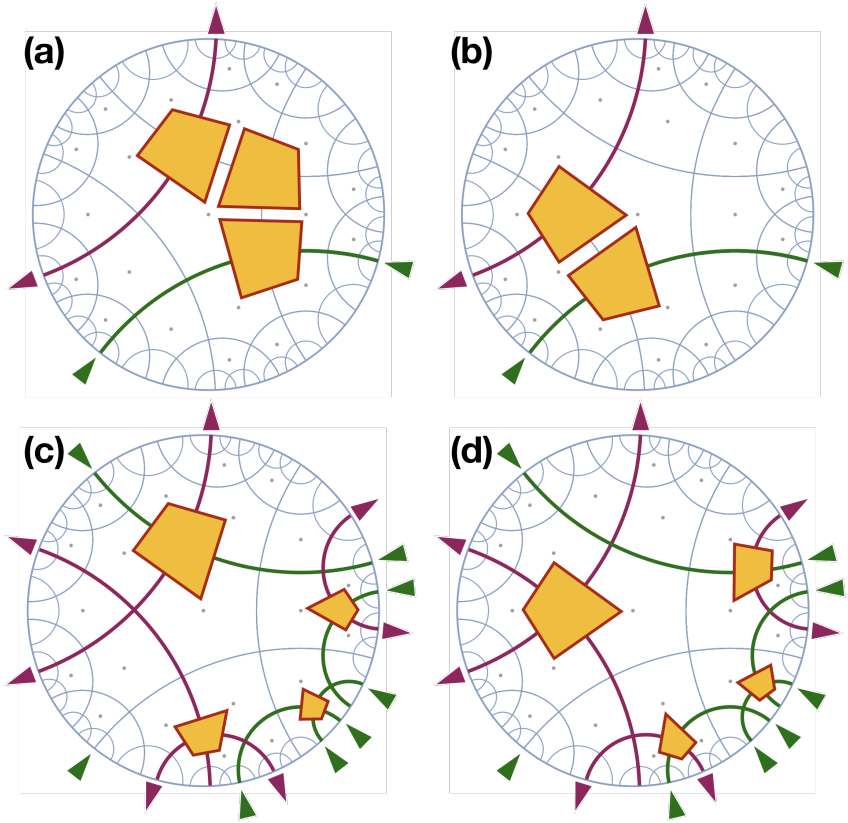

Figure 3.7: Two examples of isometry violation. (a, b) The dense three-fracton excitation state cannot be distinguished from the two-fracton excitation state by examining the boundary. (c, d) Two states with four-fracton excitations cannot be distinguished by examining the boundary. Figure reproduced from Ref. [131].

identify γ_1 and γ_2 with ± 2 charges, thus determine the location of the fracton, and the entire bulk [Fig. 3.8a].

All the two fracton excited states can also be included in this subset. The most-likely case is that we have four geodesics with non-zero subsystem charges, which pins down the two fractons [Fig. 3.8b]. The hyperbolic lattice geometry guarantees us that situation like Fig. 3.8d will never happen, since in that case the four geodesics form a rectangle with all its corners of angle $\pi/2$. Such rectangles cannot exist in hyperbolic geometry.

The other possibility is when the two fractons sit on the same geodesic, a situation illustrated in Fig. 3.8c . In this case there are only two geodesics with non-zero subsystem charges. However, due to the lattice geometry, there is one and only one geodesic that intersects both, so it can be uniquely determined. Hence the two fractons' positions can always be located.

The isometry will be broken if we further include all three-fracton excited states. The Figs. 3.7 a,b illustrate one of such examples, in which the three-fracton excited state has the same boundary as the two-fracton excited state. This can be fixed by excluding

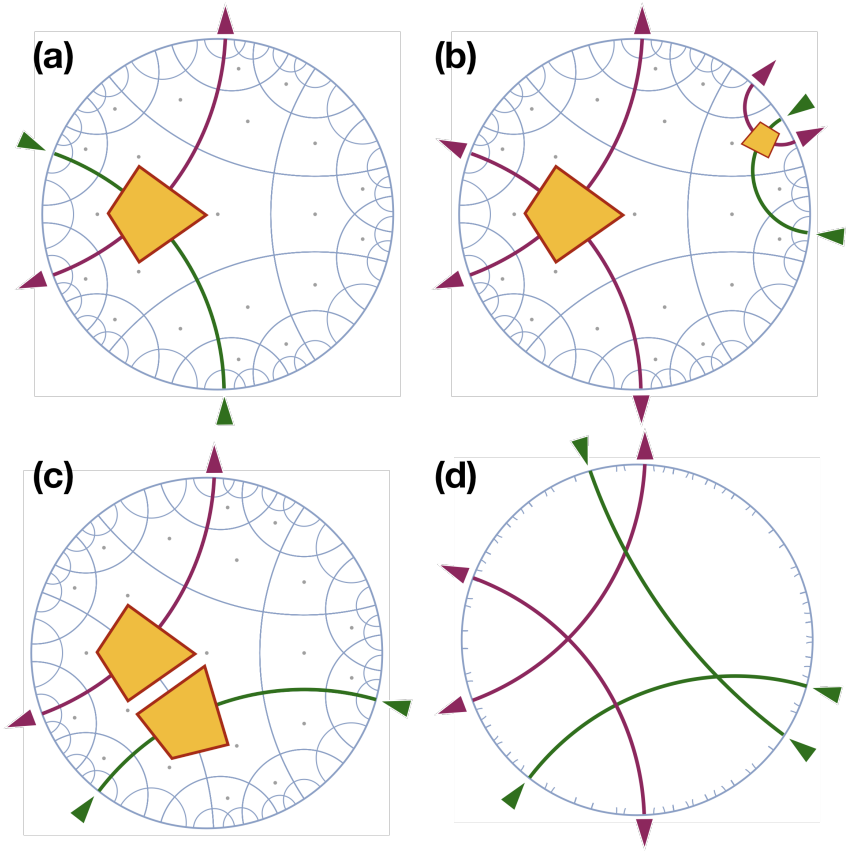

Figure 3.8: (a) A single fracton excitation can be reconstructed from the boundary by identifying the geodesics with non-zero subsystem charges. (b, c) Two-fracton excitations can also be reconstructed, even if they lie on the same geodesic which has zero-charge from boundary point of view. Because such geodesic can be uniquely identified. (d) Geodesics in this configuration are forbidden by the lattice geometry, which guarantees situations of (b) are always unambiguous about the locations of two fractons. Figure reproduced from Ref. [131].

the cases when the three-fracton excitations are *dense*, that is, they locate around the same pentagon. Once such cases are removed from the subset, so that only the diluted three-fracton excitations are included, isometry is recovered.

The same procedure can be applied as higher-energy states are included: if by local operations a state can be turned into a lower energy one [Figs. 3.7a,b] or one at the same energy level [Figs. 3.7c,d], it should excluded in the subset. In this way we include as many lower energy states as possible while maintaining isometry. To enumerate all cases is a slightly tedious task, but in principle achievable. Roughly speaking, as long as the fracton excitations are "diluted," isometry holds. This is actually very sensible, since high energy density means distortion of the local space geometry, where the lattice model is not a good representation anymore.

Coming back to the question in the beginning of this section, at low energy levels, we can include most of the states without violating isometry. Or, if we include all states

at low energy levels, the isometry is not broken too much. This is also the case of holographic tensor networks [15]

An interesting side note is that the mostly-preserved isometry for low energy excitations is a consequence of the negatively-curvatured geometry. On the Euclidean lattice, isometry is completely violated starting from two fracton excitations.

3.7 Non-Local Black Hole Microstate Degree of Freedom

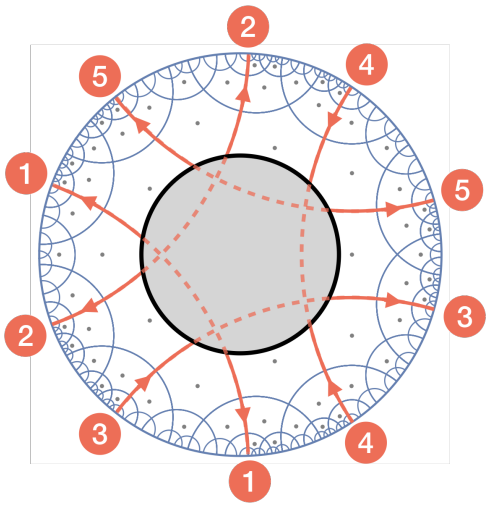

Figure 3.9: A black hole in the hyperbolic fracton model. The five labeled geodesics are cut into five pairs. The black hole microscopic degrees of freedom are whether each pair has aligned arrows (pair 3 here) or anti-aligned arrows (pair 1, 2, 4, 5 here). Figure reproduced from Ref. [131].

Another concept made clear in the dual picture is the black hole microstates, which turn out to be non-locally encoded on the horizon and also on the boundary.

In Ref. [48], we used the increase of ground state entropy in the bulk to compute the black hole entropy. An equivalent definition of black hole entropy is the entropy from the microstates of the black hole [47]. In the spin picture from the hyperbolic fracton model, how to identify them is a bit obscure: the microstate dofs are not the spins next to the horizon, since they are collectively constrained by the non-local symmetry structure, and not independent from each other.

In the dual vertex model, the microstates of the black hole become clear. Let us take the black hole in Fig. 3.9 as an example. There are five geodesics cut open by the black hole. So attached to the horizon are ten threads, extending to the boundary.

Let us first consider the original ground states without the black hole. From the boundary point of view, they are those that each pair of threads aligned in the same direction, so that each geodesic has zero subsystem charge. We define the normalized subsystem

charge

$$c_i = \frac{C_i}{2} \mod 2, \tag{3.18}$$

where the C_i denotes the subsystem charge from the i-th pair of bit-threads observed from the boundary. The ground states then can be expressed collectively as states satisfying

$$(c_1, c_2, c_3, c_4, c_5) = (0, 0, 0, 0, 0). \tag{3.19}$$

After introducing the black hole, the two bit-threads in each pair become independent. For the boundary, that means the normalized subsystem charges for these pairs can be

$$c_i = 1, \text{ or } 0. \tag{3.20}$$

The different black hole microstates correspond to different arrays $(c_1, c_2, c_3, c_4, c_5)$. That is, the dofs living on the horizon are whether each pair of threads is aligned or not. Or in more mathematical terms, the microstates are all the ground states quotient the subsystem symmetries from the no-black-hole bulk. Here we emphasis that the single bit-threads should not be viewed as the dofs individually. This is a critical to identify the correct black hole microstates: different states connected by subsystem symmetries should not be counted, since they are already included in the entropy contribution of ground states without black holes. This is also reason we use the normalized subsystem charge c_i instead of the original C_i: to guarantee that the microstate is invariant under subsystem symmetries.

A sanity check is to consider the "entanglement entropy" as half the classical mutual information between the black hole and the AdS boundary. As mentioned, the mutual information is counted by the number of threads ending on the horizon on one side and the AdS boundary on the other side. So the entanglement entropy is counted by this number divided by two, i.e., each pair of thread counts as one dof. This is consistent with the microstate dof counting.

One interesting implication of the result is that the black hole dofs are encoded *non-locally*. A single thread of a pair only gives some information of C_i but no information of c_i at all. Only when both bit-threads are known can we recover the value of c_i. Thus the black hole microstate information is non-locally encoded on its horizon and also the AdS boundary.

Such conclusion agrees with the analysis in Ref. [125], where the authors discussed how much of the AdS boundary subregion needs to be measured to distinguish black hole microstates.

In our bit-thread model, as the observer starts to expand the observed subregion on the boundary, he/she will know the arrow directions of more threads. But any pair of thread heads from the black hole is separated by a macroscopic distance, so starting from zero up to a finite subregion, the observer cannot infer any information about the black hole microstate. As the first pair of cut-open threads is included in the observed

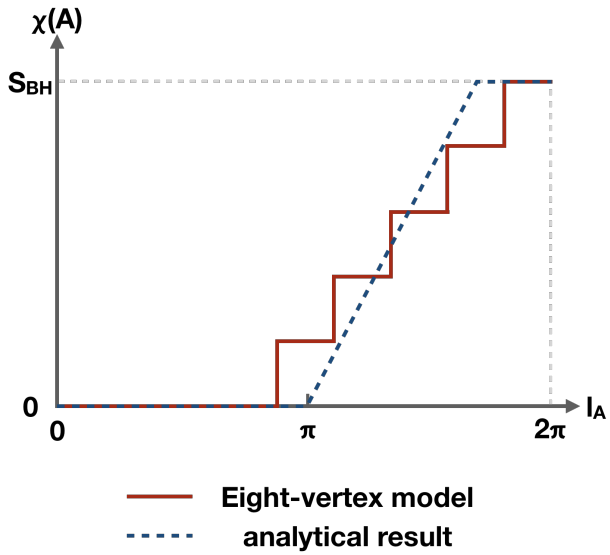

Figure 3.10: Black hole microstate information for observer covering a subregion of the boundary. Red line: in the eight-vertex model, the observer starts to have black hole microstate information when covering a pair of geodesics cut open by the black hole [Fig. 3.9]. Such information is zero until the observer reaches about half the boundary size, and gradually grows till the observer almost covers the entire boundary. Blue line: analytical calculation of the Holevo information measuring the microstate distinguishability as a function of the boundary subregion area measurable to the observer in Ref. [125]. Even though the black hole in the eight-vertex model is very naively defined, the black hole information recovery behavior looks similar to the analytical results. Figure reproduced from Ref. [131].

subregion, the observer begins to have some information of the black hole microstates, and the amount of information grows approximately linearly as the subregion expands. Finally when almost covering the full boundary, the observer can obtain all the information of the black hole microstate.

In Fig. 3.10, we plot the black hole microstate information as a function of the observed subregion from the eight-vertex model, as well as the analytical result obtained in Ref. [125]. The behaviors of the two curves qualitatively agree, in terms of the zero information segment in the beginning, the linear growth in the middle and the final saturation.

3.8 Outlook

In this chapter we discussed in detail the implications of the dual eight-vertex model equivalent to the original hyperbolic fracton model. Despite the equivalence, it advances our understanding by providing a much clearer picture of a few aspects of its physics.

The hyperbolic eight-vertex model becomes a discrete bit-thread model at zero temperature. This explains why the fracton model has the holographic properties demonstrated before. It is also significant that we have another concrete, sophisticated holographic model – the bit-thread model – as a reference frame to evaluate the similarity between fracton models and the informational-aspects of holography. It is a very useful guideline to construct improved holographic fracton models. For example, fracton bit-threads being discrete is a major obstacle for holography at higher order (for disconnected boundary components), or below the AdS scale (i.e., for regions smaller than the pentagon). So an improved version should tackle such problems.

The connection between the fracton model and bit-threads also implies that it might be possible to establish a concrete duality between linearized gravity (or theories with linearized diffeomorphism-like gauge symmetry) and the full-fledged bit-thread model. It has been pointed out that rank-2 U(1) gauge theory, the underlying effective theory of the hyperbolic fracton model (with Higgs mechanism), is actually the linearized limit of certain gravitational theory. This also gives us some confidence in constructing more sophisticated holographic fracton models to mimic gravity better.

At finite temperature, utilizing the bit-thread picture and subsystem charges, one can establish isometry for a subset of low energy states, and identify the non-locally encoded black hole microscopic dofs. It is intriguing to ask what will these subsystem charges become when we work on the continuous field theory, or what is their analogy in gravity.

To explore the relationship between gravity and fracton states can be a meaningful program for condensed matter physics. A lot is known on how topological orders are described by gauge theories, but not much on what kind of (beyond) topological order can arise from gravitational-like theories. Certain fracton states seem to be such examples [35, 113, 121], but the whole picture is vastly unexplored.

If we could discover more gravity-like many-body systems, they may also help us establish links between gravity and various other toy models of holography, including the holographic tensor networks and the bit-thread model. This chapter already serves as a primitive example of the latter case. It is also attractive to mimic gravity in a laboratory using fracton states, after we understand their relations better.

Chapter 4

Unifying holographic toy models with rank-2 U(1) field theory

In the previous two chapters, a toy fracton model in AdS space was studied and shown to satisfy holographic properties in a similar fashion as the holographic tensor-networks.

Some important questions remain unanswered despite these discoveries. First, what are the connections between these different holographic toy models? Can we find a universal picture behind them? Furthermore, what is the continuous limit of of such universal picture, and is there a bulk field theory for it, instead of some discretized lattice model? And, how is the bulk theory related to gravity? This is in particular intriguing for the perfect tensor models, since they are clever constructions directly motivated by the holographic entanglement properties, but their correspondence to any concrete bulk field theory is still unknown. Although the hyperbolic fracton model is a spin model in the bulk, it is still far from a field theory that shows satisfactory resemblance to gravity.

In this chapter, we advance our understanding of holographic toy models by providing answers to these questions. First, we point out that there is a universal picture behind different constructions of holographic toy models: a homogeneous and isotropic distribution of bit-threads in the continuous limit. Upon proper lattice discretization, it becomes the different toy models on lattice. We then argue that the traceful, vector-charged rank-2 U(1) (R2-U1) gauge theory, a theory with linearized diffeomorphsim as its gauge symmetry, gives rise to this continuous bit-thread picture. We reason that in the presence of spatial curvature, the gauge symmetry, and the consequent Gauss's laws, only allow electric field lines along a geodesics to be the fundamental dynamical variables (magnetic field), Any loop configurations like in conventional U(1) theory are forbidden. Hence the entanglement structure is determined by the "geodesic string condensation," which is exactly the continuous bit-thread picture. As such, we establish the connection between the holographic toy models and a concrete gravity-like bulk field theory, and shows how entanglement structure emerges from linearized diffeomorphism.

4.1 Bit-thread type holographic toy models as a universal picture

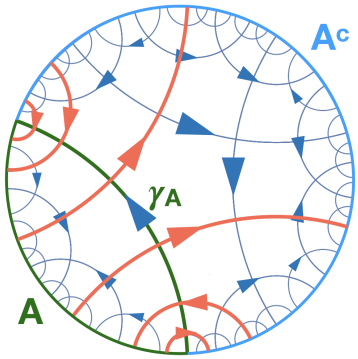

Figure 4.1: Universal picture of holographic toy models: bit-threads distributed evenly on the hyperbolic lattice. In the continuous case it is bit-threads distributed homogeneously and isotropically in AdS space. The bit-threads connecting boundary subregion A and its complement A^c are highlighted in orange. Their number is proportional to the length of covering geodesic γ_A, which yields the Ryu-Takayanagi formula (Eq. (4.1)). Figure reproduced from Ref. [136].

This chapter focuses on the field-theory aspect of fracton holography. It is motivated by the similarity between different toy models of holography. These toy models are based on two different constructions: the hyperbolic fracton model introduced in the two previous chapters, and the perfect tensor-networks [12–18]. But we observe that they belong to a universal picture: They are equivalent to bit-threads arranged on a tessellation of the hyperbolic disk. A bit-thread is a line with entangled qubits (or more generally, we can consider any quantum/classical degrees of freedom) at its two ends [19–21]. A flow of the bit-threads in the AdS space, when saturating minimal covering surface of a boundary subregion, gives the correct entanglement entropy described by the Ryu-Takayanagi formula [RT-formula] [22, 23]

$$S_{\mathrm{A}} = \frac{\mathrm{area}(\gamma_A)}{4G_N}. \tag{4.1}$$

The hyperbolic fracton model is dual to the eight-vertex model defined on the edges of the pentagon tessellation [Fig. 4.1] as discussed in previous two chapters. At low temperature, the eight-vertex model becomes a web of independent one-dimensional chains with ferromagnetic couplings. Each chain is then a classical bit-thread with its two ends correlated.

Recent work by Jahn et al. [135, 137] show that the perfect tensor-network can be described by Majorana modes via Jordan-Wigner transformation. In the Mjaorana fermion language, the tensor-network state becomes a collection of Majorana dimers. Each dimer locates at the two ends of a geodesic on the tensor tessellation, which is the bit-thread.

	AdS/CFT	Bit-thread type toy models	random tensor-networks
RT-formula for connected boundary subregion	Yes	Yes	Yes
RT-formula for disconnected boundary subregion	Yes	No	Yes
$n-$dependence of Rényi entropy	Yes	No	No
Non-flat entanglement spectrum	Yes	No	No

Table 4.1: Comparison of the holographic entanglement properties between genuine AdS/CFT, bit-thread type holographic toy models, and random tensor-networks. The bit-thread type holographic toy models, as a "leading order" approximation to holographic entanglement entropy, capture the Ryu-Takayanagi formula (Eq. (4.1)) for connected boundary subregion, but not other finer details. Table reproduced from Ref. [136].

Following these observations, a universal picture of the holographic toy model emerges: by arranging the bit-threads in the AdS space homogeneously and isotropically in the continuous limit, or on a regular tessellation in the discrete case, the simplest toy model of holography can be constructed.

Such toy models capture the RT-formula for entanglement entropy of any *connected* boundary subregion. Instead of adjusting the bit-thread flow to saturate the target covering surface like in the original proposal [19], the bit-threads in this picture are in a fixed configuration, but the RT-formula is satisfied due to their even distribution in the bulk. The bulk information is defined in the dual model in both the hyperbolic fracton model and the perfect tensor-networks. Its reconstruction obeys the Rindler reconstruction rule [122, 138], again when the boundary subregion is connected.

It can be viewed as a "leading order" approximation of the entanglement structure of AdS/CFT. Built upon a collection of two-body entangled qubits/bits only, it naturally fails to capture the finer entanglement structure of genuine gravitational AdS/CFT.

For example, the entanglement spectrum of a boundary subregion is always flat, thus the nth-Rényi entanglement entropy

$$S_n(\rho_A) = \frac{1}{1-n} \log \mathrm{Tr} \rho_A^n \tag{4.2}$$

has no n-dependence, while in AdS/CFT the n-dependence is non-trivial [139]. Also, such models deviate from the RT-formula when the boundary subregion has multiple disconnected components. This deviation is due to the bit-threads connecting different components of the boundary subregion, which is discussed in the previous chapter.

In Table. 4.1 , we have summarized the comparison between genuine AdS/CFT, the bit-thread type toy models, and for completeness also the holographic random tensor-networks proposed by Yang et al. [15–17]. The random tensor-network satisfies RT-formula for arbitrary boundary subregion, and does not belong to the universal picture proposed here.

These observations lead to the question this work addresses: what is the bulk field theory that gives rise to the bit-thread type of holographic toy models? These toy models capture the RT-formula and Rindler reconstruction at "leading order," but fails at

"higher order," or the finer entanglement structure. Thus, the reasonable speculation is that such bulk theory cannot be the full-fledged general relativity, but it has to share certain essential features of gravity or is a special limit/case of it.

We will show that, the bulk theory that describes the bit-thread type toy models is the Lifshitz gravity [140, 141] in the high energy theory literature, or the traceful, vector-charged rank-2 U(1) gauge theory [32, 33, 36, 37, 80, 114] in the condensed matter physics literature. As a special case of general relativity, its gauge symmetry is the spatial part of the linearized diffeomorphism. As we will elaborate, the consequence of such gauge symmetry is that the electric field lines can only travel along the geodesics in AdS space, instead of forming local loops like in conventional gauge theory. Hence, the entanglement structure is the continuous bit-thread distribution.

4.2 Rank-2 U(1) Theory and Its Flat-Space Dynamics

Let us first quickly review the traceful, vector-charged version of R2-U1 theory [32, 33, 36, 80]. Here we work in two-dimensional space, but the physics naturally extends to higher dimensions.

The R2-U1 theory has gauge symmetry

$$A^{ij} \to A^{ij} + \partial^i \lambda^j + \partial^j \lambda^i. \tag{4.3}$$

Taking A^{ij} as the perturbation of the metric $A^{ij} = h^{ij} - \delta^{ij}$ in general relativity, the transformation is the linearized limit of diffeomorphism.

The gauge symmetry corresponds to the Gauss's laws of the electric field at low energy. In this case, the electric field is a rank-2 symmetric tensor

$$E^{ij} = E^{ji}. \tag{4.4}$$

The Gauss's laws imposed on the electric field is

$$\partial_i E^{ij} = 0. \tag{4.5}$$

We take both Eq.(4.4) and (4.5) to be the Gauss's laws at the low energy sector of the theory.

The charge for such diffeomorphism-like gauge theory is a vector, defined as

$$\rho^i = \partial_j E^{ij}. \tag{4.6}$$

Beside the total vector charge conservation, the symmetric condition imposes an additional conservation law

$$[\int dv\, \boldsymbol{\rho} \times \mathbf{x}]^k = \int dv\, \epsilon^k_{\ ij} x^i \partial_l E^{jl} = -\int dv\, \epsilon^k_{\ ij} E^{ij} = 0. \tag{4.7}$$

This restricts the movement of a vector charge $\boldsymbol{\rho}$. The charge $\boldsymbol{\rho}$ can only move in the direction of itself. It has crucial consequences in the entanglement structure, as we shall see.

Finally, in the *flat* space, the magnetic field is the simplest gauge symmetry-invariant term,

$$B = \epsilon^{ai}\epsilon^{bj}\nabla_a\nabla_b A_{ij}. \tag{4.8}$$

And the Hamiltonian is

$$\mathcal{H}_{\text{R2-U1-flat}} = UE_{ij}E^{ij} + tB^2. \tag{4.9}$$

The dynamics B, however, do not survive in the presence of spatial curvature, as we will explain later.

The Hamiltonian of Eq. (4.9) is also a case of Lifshitz gravity [37]. Treating A^{ij} as the perturbation of the metric, the magnetic field squared term B^2 is equivalent to R^2, R being the Ricci scalar. Here, the conventional linear term R and cosmological constant Λ in general relativity, as well as the self-interacting, non-linear terms are forbidden due to the time-reversal, lattice translation, and spatial reflection symmetries. This was carefully analyzed in Ref. [37]. So the theory of Eq. 4.9 can be viewed as a special version of linearized gravity.

4.3 Entanglement structure from Gauge symmetry: conventional U(1) as an example

Before examining the entanglement structure of the R2-U1 in AdS space, let us first review the topological entanglement entropy in the conventional U(1) gauge theory from the condensed matter point-of-view [142–145]. It is the string-net condensation picture proposed by Levin and Wen [142]. This helps to understand the logical chain of how gauge symmetry determines the entanglement structure.

The gauge symmetry for conventional U(1) theory

$$A^i \to A^i + \partial^i\lambda \tag{4.10}$$

as our starting point determines the Gauss's law to be electric charge conservation

$$\partial_i E^i = 0 \tag{4.11}$$

At low energy, the operations of gauge field A^x, A^y are to construct microscopic electric fields, or dipoles (cf. Table. 4.2). The gauge field operators respect the charge conservation globally, but not locally. Mathematically, that is to say the gauge field themselves are not gauge invariant.

To respect the Gauss's law in any infinitesimal, local subregion, the dipoles operators have to be connected head-to-tail together to form a loop. The minimal loop is the magnetic field $B = \epsilon^{ij}\nabla_i A_j$ (cf. Table. 4.2), which is now gauge invariant.

Gauge symmetry & Gauss' law	gauge operator **A**	gauge invariant operator magnetic field **B**	electric field line
$A^i \to A^i + \partial^i \lambda$ $\partial_i E^i = 0$	A^x A^y 	B 	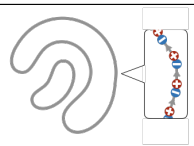
$A^{ij} \to A^{ij} + \partial^i \lambda^j + \partial^j \lambda^i$ $\partial_i E^{ij} = 0 \quad E^{ij} = E^{ji}$ curved space	A^{xy} A^{yy} A^{xx} 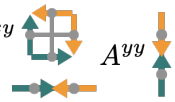	B_g 	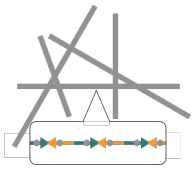

Table 4.2: From gauge symmetry to the entanglement structure. This table demonstrates the logical chain leading from the gauge symmetry to the configurations of electric field lines as the dynamical variables. The second row is for conventional U(1), where the electric field lines can be arbitrary loops. The third row is for rank-2 U(1) in AdS space, where the electric field lines are on the geodesics extending to infinity. The first column of the table is the starting point of the logic chain. It states the Gauss's laws and the associated gauge transformations for different gauge theories. The second column illustrates that the gauge operators effectively create multipoles of charges from the point of view of lattice theory. The third column expresses the magnetic fields **B** as compositions of gauge operators. Being gauge-invariant means that the gauge operators need to be placed in such a way that in any local region the Gauss's laws are satisfied. The magnetic field creates a field line (or loop) of electric field. Finally, the fourth column illustrates that the vacuum of a system is the fluctuation of the electric field lines. In the case of R2-U1 in curved space, these lines do not form loops. Instead they stay on the geodesics, and extend to infinity. They are the bit threads. Table reproduced from Ref. [136].

To be an eigenstate of the magnetic field term B^2, the vacuum of the system is the fluctuation of the electric-field-line loops, or a superposition of all loop configurations [142]. This enables the calculation of topological entanglement entropy.

Here we can identify the crucial chain of logic: the gauge symmetry chosen determines the Gauss's laws; the gauge operators are those objects (dipoles) obeying Gauss's law globally but not locally; they can be used to construct the magnetic field that respect Gauss's law in any local region (minimal loops); the magnetic field determine the configuration of electric field lines at low energy (all loop configurations), which then determine the entanglement structure of the system.

In Table.4.2, the above logical chain is shown on the second row.

4.4 Entanglement structure of R2-U1 in AdS space: geodesic string condensation

Now let us examine the entanglement structure of R2-U1 in the 2-dimensional AdS space following the same mechanism. We will see that instead of string-net condensation, the picture will be *"geodesic string condensation."* That is, the electric field lines travel along geodesics only, and the superposition of fluctuating electric field lines is the vacuum that determines the entanglement structure. The facts that the charge is a vector, and space is curved, play crucial roles in determining the entanglement structure.

Like in the previous section, the gauge symmetry and Gauss's laws determine the effects of gauge operators in terms of creating vector charge multipoles. They are listed in Table. 4.2. The diagonal terms A^{xx}, A^{yy}, or in general $A^{ij}s_i s_j$ for direction $\hat{\boldsymbol{s}}$ is to move a vector charge along the direction it points. The off-diagonal term A^{xy} creates a vector charge multipole with vanishing $\int \boldsymbol{\rho}$ and $\int \boldsymbol{\rho} \times \boldsymbol{x}$.

The dynamics, or magnetic fields, however, are very different in the curved space. It has been carefully studied by Slagle et al. in Ref. [114]. When a vector charge is parallel transported around a finite region back to its starting point, it will in general be different from the original vector due to the spatial curvature. So such parallel transport over a closed loop is expensive in energy, hence forbidden in the low energy sector.

Consequently, the local dynamics of B (Eq. (4.8)) is forbidden. The pictorial intuition is that the dynamics of B as illustrated by Fig. 4.2 always happen over a finite-sized plaquette in the system. In flat lattice, such combination of A^{ij} operators does not violate the Gauss's laws (Eqs. (4.4,4.4)) in any microscopic region. But in curved space it is not true anymore.

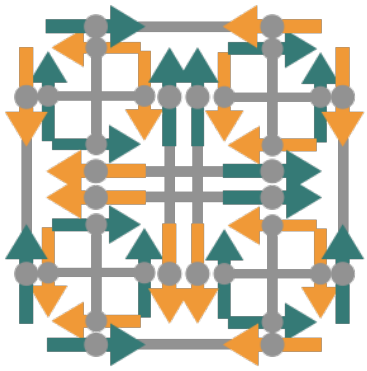

Figure 4.2: The operator B of rank-2 U(1) theory in the flat space (Eq. (4.8)). It involves multiple A^{xx}, A^{yy} and A^{xy} operators. It acts on a finite-area plaquette in the system, and does not survive the spatial curvature. Figure reproduced from Ref. [136].

To convince ourselves, we find that B (Eq. (4.8)) is not gauge invariant in the presence

of curvature. Promoting $\boldsymbol{\nabla}$ to the covariant derivative, we have

$$B \to B - R g^{aj} \nabla_a \lambda_j, \tag{4.12}$$

under gauge transformation, where R is the Ricci scalar [114]. In fact, higher order local terms up to $\nabla_a \nabla_b \nabla_c \nabla_d \lambda^e$ was systematically explored but no gauge invariant B term was found in Ref. [114].

So what are the dynamics allowed in the AdS space? We note that, the difficulty is rooted in parallel transporting a vector charge around a loop. To avoid this, we have to consider instead parallel transporting the charge on a geodesic, extending from one infinity to the other.

In the lattice model, it has the following picture: A vector charge, for example, $\boldsymbol{\rho} = (\rho^x, 0)$, can be moved along $x-$direction by acting A^{xx} operators on the path. To make sure that any local region respects Gauss's laws, however, such line-operation has to extend to infinity in both directions.

In the field theory, for a given geodesic g with unit vector $\hat{\boldsymbol{s}}$ along it, this operation is the dynamics

$$B_g = \int_g ds\, A^{ij} \hat{s}_i \hat{s}_j. \tag{4.13}$$

The fact that locally no Gauss's laws are broken is reflected by its invariance under gauge transformation

$$\begin{aligned} B_g \to & B_g + \int_g ds (\nabla^i \lambda^j + \nabla^i \lambda^j) \hat{s}_i \hat{s}_j \\ = & B_g + 2(\boldsymbol{\lambda} \cdot \hat{\boldsymbol{s}}) \Big|_{-\inf}^{\inf}, \end{aligned} \tag{4.14}$$

where the second term vanishes assuming vanishing gauge transformation at infinity.

We can thus write down the theory as

$$H_{\text{R2-U1-AdS}} = \int dv\, U E^{ij} E_{ij} + \sum_{g \in \text{all geodesics}} t_g B_g^2 \tag{4.15}$$

Such non-local dynamics are normally unfavored in many disciplines of physics. However, they are the ones stable in the presence of spatial curvature. Let us bear with them, and examine the corresponding of entanglement structure.

With such dynamics on geodesics, a drastic change happens for the electric field lines. In AdS space, instead of forming loops, they travel along geodesics from one boundary point to another. The vacuum is then a superposition of all possible geodesic electric field line configurations. We name this the "geodesic string condensation." As a result, the entanglement structure for each geodesic string is that the two boundary points are

entangled by the corresponding geodesic dynamics. As the B_g distribute in AdS space homogeneously and isotropically, we have exactly the continuous bit-thread picture we speculated at the beginning of this work. Upon lattice discretization, and also assigning $\boldsymbol{E}$ discrete/continuous values, one can obtain toy models of the same universal picture but different in details, including the perfect tensor-networks and the hyperbolic fracton models.

4.5 The case of scalar charged R2-U1

So far, we have been entirely concerned with vector-charged R2-U1 theories, as introduced in Sec. 4.2. However, it is also possible to define R2-U1 theories with scalar charges [32, 35, 36], and ask if they give rise to the same bit-thread picture. In this section, we will discuss the scalar-charged case.

In this case we consider the traceless electric field E_{ij},

$$E_{ij} = E_{ji}, \qquad E^i_i = 0. \tag{4.16}$$

The charge is defined as

$$\partial_i \partial_j E^{ij} = \rho. \tag{4.17}$$

The gauge symmetry for this case is

$$A_{ij} \to A_{ij} + \partial_i \partial_j \lambda + \delta_{ij} \gamma, \tag{4.18}$$

and in flat spacetime, the magnetic field is found to be

$$B_{ij} = \frac{1}{2}(\epsilon_{iab} \partial^a A^b_j + \epsilon_{jab} \partial^a A^b_i). \tag{4.19}$$

This version of R2-U1 has the following conservation laws:

$$\int dv \rho = 0, \tag{4.20}$$

$$\int dv \rho \vec{x} = 0, \tag{4.21}$$

$$\int dv \rho x^2 = 0. \tag{4.22}$$

In this case, the scalar charge is fractonic, due to the dipole conservation law. Furthermore, a dipole excitation can only move perpendicularly to itself. This is because the quadrupolar operator in Fig. 4.3a is forbidden as it takes a finite value of $\int dv \rho x^2$ (Eq. (4.22)), and only the quadrupolar operator in Fig. 4.3b is allowed. So in 2D, the dipole excitation has the same sub-dimensional mobility as the vector charge in the vector-charge version of R2-U1, but perpendicular to the dipoles instead of parallel.

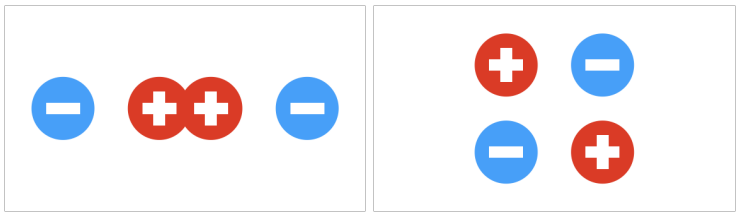

(a) quadrupole 1 **(b)** quadrupole 2

Figure 4.3: Different quadrupoles. (a) Quadrupole with non-vanishing value of $\int dv\rho x^2$ and forbidden in the traceless scalar-charged R2-U1. (b) Quadrupole with vanishing value of $\int dv\rho x^2$ and allowed in the traceless scalar-charged R2-U1.

Now we have gathered enough knowledge to ask whether a scalar-charged R2-U1 theory can also support the same type of holographic structure seen in the vector-charged theory. The answer is that it also leads to the same picture of geodesics string condensation, and gives rise to the bit threads in 2D. However, the vector-charged R2-U1 analysis can be generalized to all higher dimensions while the scalar charged version can not. Therefore the vector-charged R2-U1 is a better field theory for explaining the bit-thread picture.

4.6 Discussion

In this chapter we obtained a very pictorial, intuitive understanding of the "leading order" entanglement structure of holography, and the mechanism generating it.

First, we made the observation that different holographic toy models share the same entanglement structure as a web of evenly distributed bit-threads. In the continuous limit, the generalization of this picture is a isotropic and homogeneous distribution of bit-threads. Such entanglement structure satisfies the RT-formula for any connected region, which is a property of holographic entanglement entropy. However it fails to reproduce the finer properties including the RT-formula for disconnected boundary subregion and the non-flatness of the entanglement spectrum. Therefore we view such picture as the "leading order" approximation of the holographic entanglement.

We then go on to analyze what theory gives rise to exactly this picture. The main inspiration of the bulk theory is the fact that the hyperbolic fracton model produces the entanglement structure, and the rank-2 U(1) gauge theory gives rise to fractons. We reason that, taking the linearized diffeomorphism as the gauge symmetry, the corresponding symmetric tensor gauge theory (vector charge rank-2 U(1)) gives rise to this picture by geodesic string condensation. This is because in the presence of spatial curvature, all local dynamical terms are forbidden due to violation of gauge invariance. Consequently, only global terms are allowed, and the simplest global term is to virtually push a vector charge on a geodesic from infinity to infinity. Such global terms lead to the condensation of geodesic strings, which is the bit-thread picture we observed.

Retrospectively, it is sensible that a theory mimicking gravity at first order has the entanglement structure of gravity also at first order.

This concludes the first part of the thesis, which is to explore the connection between fracton states of matter and gravity. We have found a class of condensed matter systems featuring fractons that mimic the entanglement structure of gravity, in the context of AdS/CFT. These results improve our understanding of fracton states of matter, and also provide an intuitive picture of the holographic entanglement structure at leading order.

Chapter 5

Pyrochlore Spin System

In the first part of the thesis, we have shown that the rank-2 U(1) gauge field theory and its variations are highly interesting due to their resemblance to gravity.

In the second part of the thesis, we turn to a more experimentally oriented discussion — but during the journey there will be many interesting theoretical discoveries too.

The rank-2 U(1) theories were originally proposed as a type of exotic lattice gauge theories, and in particular have been studied as the low energy effective theory of spin liquids. Most of the prototype models are, however, complicated in terms of the lattice and the interactions. It is of course not a problem for the prototypes, whose main purpose is to demonstrate the interesting properties of the effective theory. But in the end, if we would like to observe rank-2 U(1) spin liquids in experiments, we need to know what are the most realistic and simple system that can achieve rank-2 U(1) physics.

To our delight, there actually is such a simple way to do that. It is a spin model defined on the breathing pyrochlore lattice with relatively simple spin-spin interactions. To explain how the rank-2 U(1) physics arises, we will have to first understand the pyrochlore lattice spin model, and develop some theoretical tools to analyze the emergent Gauss's laws when a spin liquid phase emerges. This will be done in Chapter 5 and part of Chapter 6. These tools will finally help us obtain the rank-2 U(1) spin liquid on the breathing pyrochlore lattice at the end of Chapter 5.

5.1 Introduction

One of the most exciting aspects of quantum many-body physics is the new phases of matter. In particular, the long-range entangled phases are only possible in quantum systems and fundamentally distinct from classical statistical systems from the point of view of renormalization. Furthermore, such states *cannot* be traced back to a broken symmetry, which is another reason for its fundamental interest. The rank-2 U(1) theo-

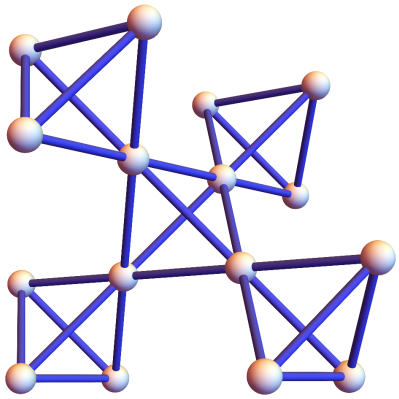

Figure 5.1: The pyrochlore lattice as a network of corner-sharing tetrahedra.

ries as spin liquids without breaking any symmetry [36] of the system are examples of such exotic states.

There are several well-known models with long-range entangled phases. For the gapped cases, toric code is a canonical example, and very sophisticated mathematical tools to classify the gapped phases have been developed in recent years. The gapless cases are much more challenging in its classification, numerical simulation and various other aspects of study. The U(1) spin liquids with emergent gapless photon excitations belong to this case.

In essence, the topological orders are often described by different gauge field theories at low energy. If we look at the classical sector of these models, very often the gauge symmetry becomes local degeneracies of ground states, constrained by the corresponding Gauss's laws.

Experimentally, discovery materials that realize either the classical physics of local degeneracy and emergent Gauss's law, or the quantum physics of long range quantum entanglement, will be highly significant. For such purposes, the spin liquid phases found in frustrated magnets are a rich source of inspiration [39] as discussed in the introduction.

The (arguably) most widely studied examples are the "spin ice" states in $Ho_2Ti_2O_7$ and $Dy_2Ti_2O_7$, classical spin-liquids famous for their magnetic monopole excitations [146]. And there is now good evidence showing that that a *quantum* spin-liquid phase could exist in materials where quantum effects play a larger role [66, 75, 147–156].

The exotic physics of spin ice originates from two features of the pyrochlore lattice compounds. First, the geometry of the pyrochlore lattice is highly frustrated as it is composed of corner sharing tetrahedra [Fig. 5.1]. Second, the magnetic rare earth ions R^{3+} on the lattice have strong anisotropic interactions between them [157, 158]. As such, a wide range of interesting, exotic physical behaviors arise from pyrochlore lattice compounds [159].

The spin ice materials $Ho_2Ti_2O_7$ and $Dy_2Ti_2O_7$ belong to a wider family of rare-earth pyrochlore oxides $R_2M_2O_7$ in which the magnetic ions have a doublet ground state, and highly-anisotropic interactions. The physical properties of these materials depend on the highly diverse choice of rare-earth R^{3+} and transition metal M^{4+}. In addition to spin ices, this family includes a wide range of systems that order magnetically, spin glasses and systems where local moments couple to itinerant electrons [159, 160]. Materials of current interest include $Yb_2Ti_2O_7$, which exhibits striking "rod-like" features in neutron scattering [161–163], and has been argued to undergo a Higgs transition into a ferromagnetically ordered state [164]; $Er_2Ti_2O_7$, which appears to offer an elegant worked example of (quantum) order by disorder [165–169]; $Er_2Sn_2O_7$, which has yet to been seen to order at *any* temperature [170, 171]; and $Pr_2Hf_2O_7$ that shows quantum modified pinch point and also signatures of magnetic monopole excitations [172]. Alongside continuing experimental investigations into these materials, the last few years has witnessed the synthesis of a steady increase of new rare earth pyrochlore oxides, exhibiting both ordered [173–177] and disordered [56] low temperature phases.

The rich variety of ordered and disordered phases calls for a comprehensive analysis. The analysis has many levels of depth. The simplest case are the ordered states, which should be explained in the framework of the Landau-Ginsberg symmetry breaking. This will of course require us to do the symmetry analysis of the spin system and work out the irreps of the spin degrees of freedom. This work is done in this chapter.

The symmetry breaking ordered phase is not capable to address the classical spin liquids like spin ice, which do not develop order, and often has no symmetry breaking. To understand these spin liquid states, new tools are developed in a series of our works [178–180], and also documented in the thesis by Owen Benton [181] comprehensively. It will be explained in the next chapter, and then used to obtain the rank-2 U(1) gauge theory.

This chapter is arranged as follows. In Section 5.2 we introduce a general model of nearest–neighbour exchange interactions on a pyrochlore lattice and, restricting to classical spins, establish the conditions under which the model has a magnetically ordered ground state.

In Section 5.3 we provide a complete classification of possible ordered states at momentum $\mathbf{q} = 0$ in terms of the irreducible representations of the tetrahedral symmetry group T_d. We show that this symmetry analysis can be used to determine the classical ground state of $\mathcal{H}_{\text{ex}}$ [Eq. (5.3)] for arbitrary parameters (J_1, J_2, J_3, J_4), utilizing the symmetry analysis. The nature of the ground states in the case $(J_3 < 0, J_4 = 0)$, which is of high relevance to real materials, is explored in detail, including analysis of the degenerate manifolds arising at the phase boundaries of the model.

In Sections 5.4, we discuss the implications of these results for the rare-earth pyrochlore oxides $Er_2Ti_2O_7$, $Yb_2Ti_2O_7$ and $Er_2Sn_2O_7$.

We conclude in Section 5.5 with a summary of our results, and an overview of some of the interesting open issues.

5.2 The pyrochlore lattice spin model with anisotropic exchange

5.2.1 Spin from a single ion

Let us start by motivating the pyrochlore spin model from its experimental, microscopic origin.

Pyrochlore oxides, $R_2M_2O_7$, are a ubiquitous feature of igneous rocks throughout the world. This broad family of materials takes its name from the mineral "pyrochlore" [$(Ca/Na)_2Nb_2O_6(OH/F)$], which burns with a green ($\chi\lambda\omega\rho\grave{o}\varsigma$) fire ($\pi\grave{\upsilon}\rho$), and shares its crystal structure with a great many other oxides, halides and chalcogenides.

Here we focus on the pyrochlore oxides in which the M-cation is a non-magnetic transition metal, such as Ti^{4+} or Sn^{4+}, while the R^{3+}-cation is a rare-earth ion with a magnetic doublet ground state. These R^{3+} magnetic ions form a *pyrochlore lattice*, built of corner-sharing tetrahedra, which has the cubic symmetry $Fd\bar{3}m$, same as the parent material.

Even within this restricted group of rare-earth oxides, there is a huge variation of the magnetic properties of the rare-earth ions, due to the interplay between strong spin-orbit coupling, and the crystal electric field (CEF) at the A-cation sites. For instance, Dy^{3+} provides the strong Ising moment in the spin-ice $Dy_2Ti_2O_7$, while Er^{3+} forms a moment with XY-like character in $Er_2Ti_2O_7$ [182].

The goal of this chapter is not to explore the physical-chemistry of the intricate CEF ground states of rare-earth ions (see *e.g.* Ref. [183, 184] for a discussion on this topic), but rather to understand the way in which the anisotropic exchange interactions between them determines the magnetic order, or properties of disorder, of rare-earth pyrochlore oxides. We therefore concentrate on materials in which the ground state of the rare-earth ion is a Kramers doublet, with an odd number of electrons, like Yb^{3+} ([Xe]$4f^{13}$) or Er^{3+} ([Xe]$4f^{11}$). In other words, our starting point is a lattice of quantum or classical spins with general interactions between them, without elaborating the microscopic origin of the effective spins models.

In this case, as long as the temperature is much lower than the lowest-lying CEF excitations, the magnetic ion can be described by a pseudospin-1/2 degree of freedom

$$[S^\mu, S^\nu] = i\epsilon_{\mu\nu\rho}S^\rho. \tag{5.1}$$

It is important to note that, even with the restriction to Kramers doublets, there are many possibilities for how S^μ will transform under space–group operations [185]. In this chapter we will focus on the case where S^μ transforms like a magnetic dipole, which is the case appropriate to Yb^{3+} and Er^{3+} based pyrochlores. We note that an alternative "dipolar-octupolar" case may be realized in Dy^{3+}, Nd^{3+} and Ce^{3+} based pyrochlores [56, 185, 186].

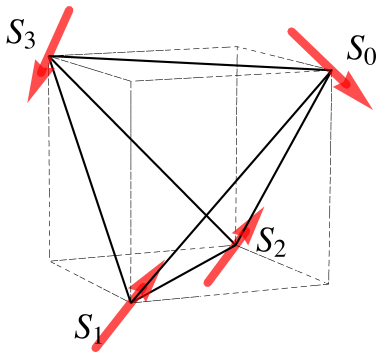

Figure 5.2: Labeling of sub-lattice sites on a tetrahedron. Figure reproduced from Ref. [188].

Where S^μ transforms like a magnetic dipole, it will be associated with an effective magnetic moment

$$m_i^\mu = \sum_{\nu=1}^{3} g_i^{\mu\nu} S_i^\nu \tag{5.2}$$

where $\mu, \nu = \{x, y, z\}$. That is, the effective magnetic moment is determined by the site dependent g-tensor $g_i^{\mu\nu}$ from microscopic details. It has physical consequences for the magnetic correlations measured in neutron scattering experiments, as the neutrons interact with the effective magnetic moments.

5.2.2 Anisotropy in exchange interactions

The interplay of spin-orbit coupling and CEF leads to anisotropic interactions between the effective spins from the rare-earth ions. It is possible to estimate the exchange interactions in a pyrochlore oxides from knowledge of the CEF ground state and low-lying excitations [183, 187]. However for the purposes of analysis in this chapter, it is sufficient to consider the general case in which the constraints on these interactions are imposed only by the symmetries of the lattice, and ignore their chemical origin.

In the case of Kramers ions on a pyrochlore lattice, the most general form of nearest–neighbour exchange breaks down into a sum over tetrahedra t

$$\mathcal{H}_{\mathsf{ex}} = \sum_{\langle ij \rangle} J_{ij}^{\mu\nu} S_i^\mu S_j^\nu = \sum_t \mathcal{H}_{\mathsf{ex}}^{\mathsf{tet}}[t] \,, \tag{5.3}$$

where

$$\mathcal{H}_{\mathsf{ex}}^{\mathsf{tet}}[t] = \sum_{\langle ij \rangle \in t} J_{ij}^{[t]\mu\nu} S_i^\mu S_j^\nu \,, \tag{5.4}$$

is the Hamiltonian for a single tetrahedron. Here, $\mathbf{S}_i = (S_i^x, S_i^y, S_i^z)$ are shown in Fig. 5.2, and $\mathbf{J}_{ij}^{[t]}$ is a 3×3 matrix specific to the bond ij, within tetrahedron t. The

magnetic ions labelled S_0, S_1, S_2 and S_3 occupy positions

$$\mathbf{r}_0 = \tfrac{a}{8}(1,1,1) \qquad \mathbf{r}_1 = \frac{a}{8}(1,-1,-1)$$
$$\mathbf{r}_2 = \tfrac{a}{8}(-1,1,-1) \qquad \mathbf{r}_3 = \frac{a}{8}(-1,-1,1)\ , \tag{5.5}$$

where a is the lattice size. The exchange interactions $\mathbf{J}_{ij}$ do not, in general, need to respect any *any* continuous spin-rotational symmetry. They are, however, strongly constrained by the symmetry of the bond ij and also the lattice symmetries.

Once these constraints are taken into account [189], the three-by-three matrix $\mathbf{J}_{ij}$ is reduced to four independent free parameters. Different $\mathbf{J}_{ij}$ for different bonds are related to each other by a proper rotation from the lattice symmetry. The exchange of the six bonds on the tetrahedron shown in Fig. 5.2 can be written as

$$\mathbf{J}_{01} = \begin{pmatrix} J_2 & J_4 & J_4 \\ -J_4 & J_1 & J_3 \\ -J_4 & J_3 & J_1 \end{pmatrix} \qquad \mathbf{J}_{02} = \begin{pmatrix} J_1 & -J_4 & J_3 \\ J_4 & J_2 & J_4 \\ J_3 & -J_4 & J_1 \end{pmatrix}$$
$$\mathbf{J}_{03} = \begin{pmatrix} J_1 & J_3 & -J_4 \\ J_3 & J_1 & -J_4 \\ J_4 & J_4 & J_2 \end{pmatrix} \qquad \mathbf{J}_{12} = \begin{pmatrix} J_1 & -J_3 & J_4 \\ -J_3 & J_1 & -J_4 \\ -J_4 & J_4 & J_2 \end{pmatrix}$$
$$\mathbf{J}_{13} = \begin{pmatrix} J_1 & J_4 & -J_3 \\ -J_4 & J_2 & J_4 \\ -J_3 & -J_4 & J_1 \end{pmatrix} \qquad \mathbf{J}_{23} = \begin{pmatrix} J_2 & -J_4 & J_4 \\ J_4 & J_1 & -J_3 \\ -J_4 & -J_3 & J_1 \end{pmatrix} \tag{5.6}$$

where we label lattice sites and interactions following the conventions of Ross *et al.* [190]. From the structure of these matrices we can identify the different physical contributions to the interaction $\mathbf{J}_{ij}$ [Eq. (5.6)] approximately as

- $J_1 \rightarrow$ "XY" with respect to the local bond
- $J_2 \rightarrow$ "Ising" with respect to the local bond
- $J_3 \rightarrow$ symmetric off diagonal exchange
- $J_4 \rightarrow$ Dzyaloshinskii-Moriya interaction

5.2.3 Anisotropic exchange in a local frame

Both the anisotropy in magnetic ground state of the rare-earth ion and the anisotropy in its interactions are dictated by the local CEF field around that ion. It is thus often convenient to describe them in a local coordinate frame rather than the global one. The local frame is denoted as

$$\{\mathbf{x}_i^{\text{local}}, \mathbf{y}_i^{\text{local}}, \mathbf{z}_i^{\text{local}}\}$$

such that the axis $\mathbf{z}_i^{\text{local}}$aligns with the C_3 symmetry axis of the local CEF on site i. These local axes are defined explicitly as

$$\mathbf{z}_0^{\text{local}} = \tfrac{1}{\sqrt{3}}(1,1,1) \qquad \mathbf{z}_1^{\text{local}} = \frac{1}{\sqrt{3}}(1,-1,-1)$$
$$\mathbf{z}_2^{\text{local}} = \tfrac{1}{\sqrt{3}}(-1,1,-1) \qquad \mathbf{z}_3^{\text{local}} = \frac{1}{\sqrt{3}}(-1,-1,1)\ .$$

In defining $(\mathbf{x}_i^{\text{local}}, \mathbf{y}_i^{\text{local}})$ we follow the conventions of Ross *et al.* [190],

$$\mathbf{x}_0^{\text{local}} = \tfrac{1}{\sqrt{6}}(-2,1,1) \qquad \mathbf{x}_1^{\text{local}} = \frac{1}{\sqrt{6}}(-2,-1,-1)$$
$$\mathbf{x}_2^{\text{local}} = \tfrac{1}{\sqrt{6}}(2,1,-1) \qquad \mathbf{x}_3^{\text{local}} = \frac{1}{\sqrt{6}}(2,-1,1)\ ,$$

such that all $\mathbf{y}_i^{\text{local}}$ lie in a common plane for easier visualization

$$\mathbf{y}_0^{\text{local}} = \tfrac{1}{\sqrt{2}}(0,-1,1) \qquad \mathbf{y}_1^{\text{local}} = \frac{1}{\sqrt{2}}(0,1,-1)$$
$$\mathbf{y}_2^{\text{local}} = \tfrac{1}{\sqrt{2}}(0,-1,-1) \qquad \mathbf{y}_3^{\text{local}} = \frac{1}{\sqrt{2}}(0,1,1)\ .$$

We now introduce a SU(2) (pseudo) spin-1/2 in this local frame, denoted as

$$[\mathsf{S}_i^\alpha, \mathsf{S}_i^\beta] = i\epsilon_{\alpha\beta\gamma}\mathsf{S}_i^\gamma\ , \tag{5.7}$$

where $\alpha, \beta, \gamma = \{\mathbf{x}_i^{\text{local}}, \mathbf{y}_i^{\text{local}}, \mathbf{z}_i^{\text{local}}\}$. Note that throughout the thesis the sans-serif S_i^α refers to the spin components in this local frame, while the serif S_i^α refers to the spin components in the global, crystal, coordinate system.

In the local coordinate frame, the most general form of exchange interactions between Kramers ions on the pyrochlore lattice can be written as [190]

$$\begin{aligned}\mathcal{H}_{\text{ex}}^{\text{local}} \;=\; \sum_{\langle ij\rangle} \Big\{ & J_{zz}\mathsf{S}_i^z\mathsf{S}_j^z - J_\pm(\mathsf{S}_i^+\mathsf{S}_j^- + \mathsf{S}_i^-\mathsf{S}_j^+) \\ & + J_{\pm\pm}\left[\gamma_{ij}\mathsf{S}_i^+\mathsf{S}_j^+ + \gamma_{ij}^*\mathsf{S}_i^-\mathsf{S}_j^-\right] \\ & + J_{z\pm}\left[\mathsf{S}_i^z(\zeta_{ij}\mathsf{S}_j^+ + \zeta_{ij}^*\mathsf{S}_j^-) + i \leftrightarrow j\right]\Big\}\end{aligned} \tag{5.8}$$

where the matrix

$$\zeta = \begin{pmatrix} 0 & -1 & e^{i\frac{\pi}{3}} & e^{-i\frac{\pi}{3}} \\ -1 & 0 & e^{-i\frac{\pi}{3}} & e^{i\frac{\pi}{3}} \\ e^{i\frac{\pi}{3}} & e^{-i\frac{\pi}{3}} & 0 & -1 \\ e^{-i\frac{\pi}{3}} & e^{i\frac{\pi}{3}} & -1 & 0 \end{pmatrix} \qquad \gamma = -\zeta^* \tag{5.9}$$

encodes the change in coordinate frames between different sublattices.

interaction in local coordinate frame	exchange parameters in global frame
J_{zz}	$-\frac{1}{3}(2J_1 - J_2 + 2J_3 + 4J_4)$
$J_{\pm}$	$\frac{1}{6}(2J_1 - J_2 - J_3 - 2J_4)$
$J_{\pm\pm}$	$\frac{1}{6}(J_1 + J_2 - 2J_3 + 2J_4)$
$J_{z\pm}$	$\frac{1}{3\sqrt{2}}(J_1 + J_2 + J_3 - J_4)$

Table 5.1: Relationship between the parameters of the anisotropic nearest–neighbour exchange model in the local coordinate frame, $\mathcal{H}_{\text{ex}}^{\text{local}}$ [Eq. (5.8)], and the exchange parameters in the crystal coordinate frame $\mathcal{H}_{\text{ex}}$ [Eq. (5.3)]. The notation used for the different components of the interaction follows Ross *et al.* [190]. Table reproduced from Ref. [188].

It is a equivalent description to the global coordinate one. The conversion between the four free parameters in this local frame, $(J_{zz}, J_{\pm}, J_{\pm\pm}, J_{z\pm})$, and parameters in the global frame (J_1, J_2, J_3, J_4), is given in Table 5.1.

The corresponding estimated parameters from experiments on $Yb_2Ti_2O_7$ [190], $Er_2Ti_2O_7$ [166], and $Er_2Sn_2O_7$ [171], are shown in Table 5.5. We will come back to discussing the materials later in this chapter.

5.2.4 Existence of the $\mathbf{q} = 0$ order

After writing down the Hamiltonian, the first thing to do is to find the ground state of $\mathcal{H}_{\text{ex}}$ [Eq. (5.3)], for a model with quantum (pseudo)spin-1/2s and arbitrary exchange interactions (J_1, J_2, J_3, J_4). It is a very difficult problem, in general only tractable at a mean-field level [66, 148, 150, 152, 191], or by numerical techniques for a finite sized lattice. However, many rare-earth pyrochlore materials are known to have relatively simple ground states with vanishing crystal momentum $\mathbf{q} = 0$, implying a 4-sublattice magnetic order [159]. Here we prove that, under the condition that $\mathbf{S}_i$ is a classical O(3) spin, $\mathcal{H}_{\text{ex}}$ [Eq. (5.3)] *always* possesses a ground state of this type. Note that, however, it is not necessarily the unique ground state of the system, there can be different types of ground state degeneracy depending on the choice of parameters. We will first prove the existence of such $\mathbf{q} = 0$, 4-sublattice magnetic order [159], and then explore the conditions for this classical ground state is unique.

We begin with the observation that, since $\mathcal{H}_{\text{ex}}$ [Eq. (5.3)] is expressed as a sum over individual tetrahedra, any state which minimizes the energy of each individual tetrahedron must be a ground state, if it can be "copied and pasted" to all the other tetrahedra. Such copy and paste can be shown to be always possible. It is convenient to split this sum into two pieces

$$\mathcal{H}_{\text{ex}} = \sum_{t \in \mathsf{A}} \mathcal{H}_{\text{ex}}^{\mathsf{A}}[t] + \sum_{t' \in \mathsf{B}} \mathcal{H}_{\text{ex}}^{\mathsf{B}}[t']; \tag{5.10}$$

where A and B refer to the two sublattices of tetrahedra, with

$$\mathcal{H}_{\mathsf{ex}}^{\mathsf{A}}[t] = \sum_{\langle ij\rangle\in t} J_{ij}^{[\mathsf{A}]\mu\nu} S_i^\mu S_j^\nu \,, \tag{5.11}$$

$$\mathcal{H}_{\mathsf{ex}}^{\mathsf{B}}[t'] = \sum_{\langle ij\rangle\in t'} J_{ij}^{[\mathsf{B}]\mu\nu} S_i^\mu S_j^\nu \,. \tag{5.12}$$

The interactions $\mathbf{J}_{ij}^{[\mathsf{A}]}$ and $\mathbf{J}_{ij}^{[\mathsf{B}]}$ are related by inversion symmetry about a single site $\mathcal{I}$

$$\mathbf{J}_{ij}^{[\mathsf{B}]} = \mathcal{I}\cdot\mathbf{J}_{ij}^{[\mathsf{A}]}\cdot\mathcal{I} \,. \tag{5.13}$$

Since $\mathcal{I}^2 = 1$, we have

$$\begin{aligned}\mathbf{S}_i\cdot\mathbf{J}_{ij}^{[\mathsf{A}]}\cdot\mathbf{S}_j &= \mathbf{S}_i\cdot\mathcal{I}^2\cdot\mathbf{J}_{ij}^{[\mathsf{A}]}\cdot\mathcal{I}^2\cdot\mathbf{S}_j \\ &= \mathbf{S}_i\cdot\mathcal{I}\cdot\mathbf{J}_{ij}^{[\mathsf{A}]}\cdot\mathcal{I}\cdot\mathbf{S}_j \end{aligned} \tag{5.14}$$

where we have used the fact that the spin $\mathbf{S}_i$ remains invariant under lattice inversion. This implies

$$\mathbf{J}_{ij}^{[\mathsf{A}]} = \mathcal{I}\cdot\mathbf{J}_{ij}^{[\mathsf{A}]}\cdot\mathcal{I} = \mathbf{J}_{ij}^{[\mathsf{B}]} \,. \tag{5.15}$$

It then follows that interactions for *any* tetrahedron t must be the same, regardless of which tetrahedral sublattice it belongs to. Therefore we can safely write the Hamiltonian as a sum over tetrahedra with the same sublattice site labeling,

$$\mathcal{H}_{\mathsf{ex}}^{\mathsf{tet}} = \sum_{i,j\in t} \mathbf{S}_i\cdot\mathbf{J}_{ij}\cdot\mathbf{S}_j \tag{5.16}$$

where $\mathbf{J}_{ij}$ are given by Eq. (5.6), and the sum runs over all pairs of sites i, j in a given tetrahedron t, which may now be of either sublattice.

The proof follows directly from this result [Eq. (5.16)]. For classical spins, $[\mathcal{H}_{\mathsf{ex}}^{\mathsf{A}}, \mathcal{H}_{\mathsf{ex}}^{\mathsf{B}}] = 0$, and we can find a ground state of $\mathcal{H}_{\mathsf{ex}}$ by choosing *any* state that minimizes the energy of a single tetrahedron, and repeating it over all A-sublattice (or B-sublattice) tetrahedra. Since every spin is shared between one A– and one B–sublattice tetrahedron, the labeling of the sublattice sites are the same upon inversion symmetry, and the Hamiltonians for A– or B–sublattices are equivalent [Eq. (5.16)], any classical spin-configuration that minimizes the energy on one tetrahedral sublattice, simultaneously minimizes the energy of the other tetrahedral sublattice. Now that it minimizes all tetrahedra in the system, it is a ground state of $\mathcal{H}_{\mathsf{ex}}$.

Or in other words, if we have a spin configuration $\{\mathbf{S}_0, \mathbf{S}_1, \mathbf{S}_2, \mathbf{S}_3\}$ that minimizes A-sublattice tetrahedron, then we can copy and paste it over all A-sublattice tetrahedra. Automatically, the B-sublattice tetrahedra are in their ground states too. Hence, the entire system is in its ground state.

Therefore, there *always* exists a classical, $\mathbf{q} = 0$ ground state of $\mathcal{H}_{\text{ex}}$ [Eq. (5.3)], with 4-sublattice long-range magnetic order, for arbitrary exchange interactions (J_1, J_2, J_3, J_4). This is true in the presence of finite Dzyaloshinskii-Moriya interaction J_4 in particular.

Such $\mathbf{q} = 0$ ground state has a finite, discrete degeneracy from the breaking of point-group and time-reversal symmetries (in the case of classical spins, time-reversal corresponds to the inversion of all spins $\mathbf{S}_i \to -\mathbf{S}_i$). This degeneracy must be at least 2 (time-reversal), and is typically 6 from C_3 rotations $\otimes$ time-reversal, for the ordered phases considered in this chapter.

5.2.5 Conditions for the uniqueness the $\mathbf{q} = 0$ order — the "Lego–brick" rules

The existence of a classical ground state of $\mathcal{H}_{\text{ex}}$ [Eq. (5.3)] with 4-sublattice $\mathbf{q} = 0$ magnetic order, for arbitrary exchange interactions (J_1, J_2, J_3, J_4) leads to an significant simplification. It is much easier to determine the four-spin-configuration that minimizes the energy of a single tetrahedron (as described in Section 5.3, below) than to find the ground state of the entire system. However, as we shall see, many of interesting properties of rare-earth pyrochlores arises when such a classical ground state is not the unique one.

Here, let us first establish the condition for uniqueness of a 4–sublattice ground state, up to the discrete degeneracy of the state itself. It amounts to the following procedure: (1) identify the spin configurations that minimize the energy of a single tetrahedron; (2) find out how these configurations can tile the entire lattice consistently.

For many purposes, it is convenient to think of such procedure as a set of "Lego–brick" rules for fitting together spin-configurations on a lattice. These rules allow us to determine the degeneracy of the ground states of the whole lattice, using the ground states of a single tetrahedron.

The rules can be stated as follows:

1. If the spin on every site of the tetrahedron points in a different direction in each of its classical ground–states, then the 4–sublattice ground state of the lattice is unique up to global symmetry operations. In this case, the degeneracy of the ground states of the lattice is the same as that of a single tetrahedron.

2. If, within the set of ground states for a single tetrahedron, there are two states share the same spin orientation for a single site, the 4–sublattice ground state of the lattice is not unique. In this case, the system undergoes a dimensional reduction into independent kagome planes, and the degeneracy of classical ground states is at least as $\mathcal{O}(2^L)$, where L is the linear size of the system.

3. If, within the set of ground states for a single tetrahedron, there are two states which have the same spin orientation on two sites, the 4–sublattice ground state

is also not unique. However in this case, the number of classical ground states must grow as *at least* as $\mathcal{O}(2^{L^2})$, corresponding to dimensional reduction into independent chains of spins. In the special case of spin–ice, the corresponding classical ground–state degeneracy is extensive.

Let us elaborate on these statements. The first rule guarantees the uniqueness of a 4-sublattice ground state, where the spin on every site of the tetrahedron points in a different direction in each of its ground states. Hence, the only option to tile the entire system consistently is to copy and paste the same configuration over the whole lattice. Otherwise two neighboring tetrahedra will have conflict configuration for the spin they share. Away from phase boundaries, this is always true for *all* of the 4-sublattice $\mathbf{q} = 0$ ordered phases discussed in this chapter.

In contrast, it is clear from Rules 2 and 3 that if two of the ground states of a single tetrahedron share a common spin orientation on a given site, then it is *always* possible to construct other ground states, with finite $\mathbf{q}$. This is because after fixing the spin configuration of the first tetrahedron, we have multiple options for the next neighboring tetrahedron.

To give a concrete example of how these "Lego–brick" rules work, let us assume that two different ground states for a single tetrahedron have identical orientation of the spin on sublattice site 0, but different orientation of the spins on sites 1, 2 and 3. In this case it is possible to divide the pyrochlore lattice into a set of parallel kagome planes, containing spins associated with sublattice sites 1,2 and 3, separated by triangular-lattice planes associated with site 0. Since each kagome plane can take on one of two different spin configurations, the number of such ground states grows as 2^{N_K}, where N_K is the number of kagome planes. As different kagome planes are independent from each other, the ground states encompass all possible $\mathbf{q} \parallel [111]$. This is called dimensional reduction. Dimensional reduction of this type occurs on the classical phase boundary between ordered FM and Palmer–Chalker phases, which is discussed in Section 5.3.10 of this chapter.

An example where Rule 3 applies, and a set of independent chains emerges in the ground state manifold, is the phase boundary between the Palmer–Chalker phase and the non–coplanar antiferromagnet discussed in Section 5.3.8. However the "Lego–brick" rules permit even larger ground–state degeneracies, as is known from the "two–in, two–out" states, made famous by the spin–ice problem. In this case there are a total of 6 possible ground states for a single tetrahedron, but each possible spin orientation, on each site, belongs to 3 different ground states. According to Rule 3, the 4–sublattice classical ground-state — a ferromagnet — should not be unique, and the total number of classical grounds states must grow as *at least* $\mathcal{O}(2^{L^2})$. In fact, the ground–state degeneracy of spin ice is extensive, scaling as $\Omega_{\text{ice}} \sim (3/2)^{N/2} \sim \mathcal{O}(e^{cL^3})$, where N is the total number of sites in the lattice [71]. This manifold of spin–ice states includes ground states with all possible $\mathbf{q}$.

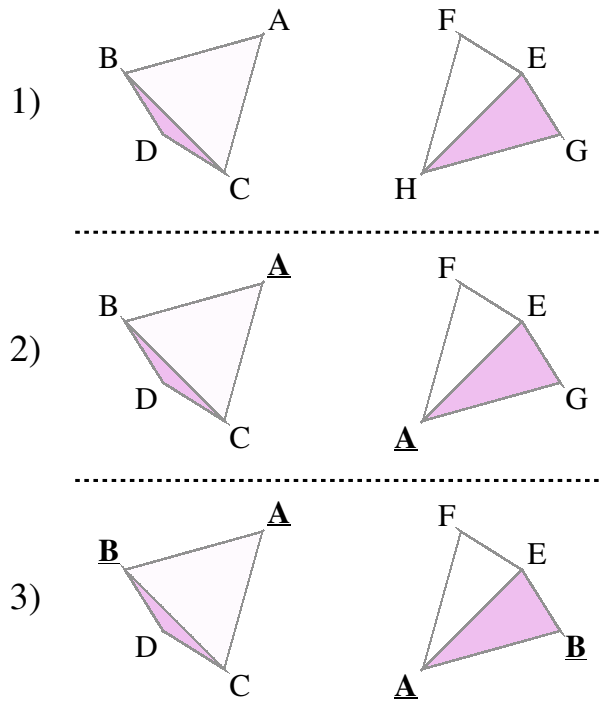

Figure 5.3: The "Lego–brick" rules describing how the ground states of a single tetrahedron can be connected to tile the pyrochlore lattice. The two tetrahedra in the left and right panels represent a pair of tetrahedra in distinct ground–state configurations. Distinct spin orientations on the sites of each tetrahedron are denoted by letters **A**—**H**. Three cases are shown. In case (1) all of the ground states for a single tetrahedron have different spin orientations for any given site. This means that two tetrahedra in distinct ground states cannot be joined together because they do not share a common spin orientation on any site. In this case the 4–sublattice ground state of the lattice is unique with $q = 0$ order, up to global symmetry operations. In case (2) there are two ground states configurations for a tetrahedron which share a common spin orientation on a single site, here denoted **A**. These tetrahedra can be joined together by sharing the spin in orientation **A**. In this case the ground state of the lattice has a degeneracy of at least $\mathcal{O}(2^L)$. Indeed, successive kagome layers of spins can be independently in BDC or FEG configurations. In case (3) there is a pair of ground states which share common spin orientations on two sites, here denoted **A** and **B**. These tetrahedra can be joined together by sharing the spin in orientation **A** or the spin in orientation **B**. In this case the ground state of the lattice has a degeneracy of at least $\mathcal{O}(2^{L^2})$. Figure reproduced from Ref. [188].

order parameter	definition in terms of spin components	associated ordered phases
m_{A_2}	$\frac{1}{2\sqrt{3}}\left(S_0^x+S_0^y+S_0^z+S_1^x-S_1^y-S_1^z-S_2^x+S_2^y-S_2^z-S_3^x-S_3^y+S_3^z\right)$	"all in-all out"
$\mathbf{m}_{\mathsf{E}}$	$\begin{pmatrix}\frac{1}{2\sqrt{6}}\left(-2S_0^x+S_0^y+S_0^z-2S_1^x-S_1^y-S_1^z+2S_2^x+S_2^y-S_2^z+2S_3^x-S_3^y+S_3^z\right)\\ \frac{1}{2\sqrt{2}}\left(-S_0^y+S_0^z+S_1^y-S_1^z-S_2^y-S_2^z+S_3^y+S_3^z\right)\end{pmatrix}$	Ψ_2 and Ψ_3
$\mathbf{m}_{\mathsf{T}_{1,\mathsf{A}}}$	$\begin{pmatrix}\frac{1}{2}(S_0^x+S_1^x+S_2^x+S_3^x)\\ \frac{1}{2}(S_0^y+S_1^y+S_2^y+S_3^y)\\ \frac{1}{2}(S_0^z+S_1^z+S_2^z+S_3^z)\end{pmatrix}$	collinear FM
$\mathbf{m}_{\mathsf{T}_{1,\mathsf{B}}}$	$\begin{pmatrix}\frac{-1}{2\sqrt{2}}(S_0^y+S_0^z-S_1^y-S_1^z-S_2^y+S_2^z+S_3^y-S_3^z)\\ \frac{-1}{2\sqrt{2}}(S_0^x+S_0^z-S_1^x+S_1^z-S_2^x-S_2^z+S_3^x-S_3^z)\\ \frac{-1}{2\sqrt{2}}(S_0^x+S_0^y-S_1^x+S_1^y+S_2^x-S_2^y-S_3^x-S_3^y)\end{pmatrix}$	non-collinear FM
$\mathbf{m}_{\mathsf{T}_2}$	$\begin{pmatrix}\frac{1}{2\sqrt{2}}\left(-S_0^y+S_0^z+S_1^y-S_1^z+S_2^y+S_2^z-S_3^y-S_3^z\right)\\ \frac{1}{2\sqrt{2}}\left(S_0^x-S_0^z-S_1^x-S_1^z-S_2^x+S_2^z+S_3^x+S_3^z\right)\\ \frac{1}{2\sqrt{2}}\left(-S_0^x+S_0^y+S_1^x+S_1^y-S_2^x-S_2^y+S_3^x-S_3^y\right)\end{pmatrix}$	Palmer–Chalker (Ψ_4)

Table 5.2: Order parameters $\mathbf{m}_\lambda$, describing how the point-group symmetry of a single tetrahedron within the pyrochlore lattice is broken by magnetic order. Order parameters transform according to irreducible representations of the point-group T_d, and are expressed in terms of linear combinations of spin-components $\mathbf{S}_i = (S_i^x, S_i^y, S_i^z)$, in the global frame of the crystal axes — cf. $\mathcal{H}_{\mathsf{ex}}$ [Eq. (5.3)]. Labelling of spins within the tetrahedron follows the convention of Ross *et al.* [190] — cf. Fig. 5.2. The notation Ψ_i for ordered phases is taken from [192]. Table reproduced from Ref. [188].

5.3 Analysis of the classical phase diagram at T=0

5.3.1 Representation theory

Except in very specific points of the phase diagram, such as the Heisenberg model ($J_1 = J_2 = J, J_3 = J_4 = 0$), the Hamiltonian $\mathcal{H}_{\mathsf{ex}}$ [Eq. (5.3)] does not possess *any* continuous spin-rotation symmetry. The key to understanding its properties, therefore, is to understand how different ordered states break the space-group symmetries of the pyrochlore lattice. Our earlier observation that a classical ground state with $\mathbf{q} = 0$ exists for all possible (J_1, J_2, J_3, J_4) [Sec. 5.2.4] has made this task easier. It is therefore possible to restrict discussion to the point-group symmetries of the lattice, or even simpler, of a tetrahedron.

In this section, we apply the representation theory analysis for these point-group operations on the most generic pyrochlore lattice model of anisotropic nearest-neighbor exchange, $\mathcal{H}_{\mathsf{ex}}$ [Eq. (5.3)]. This analysis achieve two things: it simplifies the Hamiltonian of a single tetrahedron $\mathcal{H}_{\mathsf{ex}}^{\mathsf{tet}}$ [Eq. (5.16)] to a diagonal form, and it provides the set of order parameters to characterize the $\mathbf{q} = 0$, 4-sublattice ordered phases found in real materials.

The point-group symmetry of the pyrochlore lattice is the cubic symmetry group $\mathsf{O}_h = \mathsf{T}_d \times \mathsf{I}$. Here T_d is symmetry group of a single tetrahedron, and $\mathsf{I} = \{\epsilon, \mathcal{I}\}$, where ϵ is the identity and $\mathcal{I}$ is the lattice inversion introduced in Eq. (5.13). For classical spins it

is sufficient to consider T_d alone. The group T_d has 24 elements [193]. They correspond to the symmetries of the tetrahedron : $8 \times C_3$ — $\frac{2\pi}{3}$ rotation around a [111] axis; $3 \times C_2$ — π rotation around [100] axis; $6 \times S_4$ — $\frac{\pi}{2}$ rotation around a [100] axis followed by reflection in the same [100] plane; $6 \times \sigma_d$ — reflection in [011] plane; and ϵ — the identity [194].

The non-trivial irreducible representations of T_d are labeled $\lambda = \{ \mathsf{A}_2, \mathsf{E}, \mathsf{T}_1, \mathsf{T}_2 \}$. The different ways in which classical ground states of momentum $\mathbf{q} = 0$ break the symmetries of a tetrahedron can be fully characterized by introducing order parameters $\mathbf{m}_\lambda$ which transform under them. These order parameters are linear combinations of spin components, and can be expressed in either global coordinate frame of $\mathcal{H}_{\mathsf{ex}}$ [Eq. (5.3), Table 5.2] or in the local coordinate frame of $\mathcal{H}_{\mathsf{ex}}^{\mathsf{local}}$ [Eq. (5.8), Table 5.3].

In terms of same set of irreps, the anisotropic exchange Hamiltonian $\mathcal{H}_{\mathsf{ex}}^{\mathsf{tet}}$ [Eq. (5.16)] can be rewritten in a mostly diagonalized form

$$\begin{aligned} \mathcal{H}_{\mathsf{ex}}^{\mathsf{tet}} \equiv \frac{1}{2} \Big[& a_{\mathsf{A}_2} m_{\mathsf{A}_2}^2 + a_{\mathsf{E}} \mathbf{m}_{\mathsf{E}}^2 + a_{\mathsf{T}_2} \mathbf{m}_{\mathsf{T}_2}^2 + a_{\mathsf{T}_{1,\mathsf{A}}} \mathbf{m}_{\mathsf{T}_{1,\mathsf{A}}}^2 \\ & + a_{\mathsf{T}_{1,\mathsf{B}}} \mathbf{m}_{\mathsf{T}_{1,\mathsf{B}}}^2 + a_{\mathsf{T}_{1,\mathsf{AB}}} \mathbf{m}_{\mathsf{T}_{1,\mathsf{A}}} \cdot \mathbf{m}_{\mathsf{T}_{1,\mathsf{B}}} \Big] , \end{aligned} \tag{5.17}$$

where the coefficients

$$\begin{aligned} a_{\mathsf{A}_2} &= -2J_1 + J_2 - 2(J_3 + 2J_4) \\ a_{\mathsf{E}} &= -2J_1 + J_2 + J_3 + 2J_4 \\ a_{\mathsf{T}_2} &= -J_2 + J_3 - 2J_4 \\ a_{\mathsf{T}_{1,\mathsf{A}}} &= 2J_1 + J_2 \\ a_{\mathsf{T}_{1,\mathsf{B}}} &= -J_2 - J_3 + 2J_4 \\ a_{\mathsf{T}_{1,\mathsf{AB}}} &= -\sqrt{8} J_3 \end{aligned} \tag{5.18}$$

are determined by the parameters of $\mathcal{H}_{\mathsf{ex}}$ [Eq. (5.3)]. Equivalent expressions for a_λ can be found in terms of the parameters of $\mathcal{H}_{\mathsf{ex}}^{\mathsf{local}}$ [Eq. (5.8)].

The two irrep fields $\mathbf{m}_{\mathsf{T}_{1,\mathsf{A}}}$ and $\mathbf{m}_{\mathsf{T}_{1,\mathsf{B}}}$ can have a finite coupling $a_{\mathsf{T}_{1,\mathsf{AB}}} \neq 0$ between them. It can be eliminated by a basis transformation that rotates the two irreps,

$$\begin{aligned} \mathbf{m}_{\mathsf{T}_{1,\mathsf{A}'}} &= \cos\theta_{\mathsf{T}_1} \mathbf{m}_{\mathsf{T}_{1,\mathsf{A}}} - \sin\theta_{\mathsf{T}_1} \mathbf{m}_{\mathsf{T}_{1,\mathsf{B}}} \\ \mathbf{m}_{\mathsf{T}_{1,\mathsf{B}'}} &= \sin\theta_{\mathsf{T}_1} \mathbf{m}_{\mathsf{T}_{1,\mathsf{A}}} + \cos\theta_{\mathsf{T}_1} \mathbf{m}_{\mathsf{T}_{1,\mathsf{B}}} \end{aligned} \tag{5.19}$$

where

$$\theta_{\mathsf{T}_1} = \frac{1}{2} \arctan \left(\frac{\sqrt{8} J_3}{2J_1 + 2J_2 + J_3 - 2J_4} \right). \tag{5.20}$$

The Hamiltonian $\mathcal{H}_{\mathsf{ex}}^{\mathsf{tet}}$ then becomes fully diagonal

$$\begin{aligned} \mathcal{H}_{\mathsf{ex}}^{[\mathsf{T}_d]} = \frac{1}{2} \big[& a_{\mathsf{A}_2} m_{\mathsf{A}_2}^2 + a_{\mathsf{E}} \mathbf{m}_{\mathsf{E}}^2 + a_{\mathsf{T}_2} \mathbf{m}_{\mathsf{T}_2}^2 \\ & + a_{\mathsf{T}_{1,\mathsf{A}'}} \mathbf{m}_{\mathsf{T}_{1,\mathsf{A}'}}^2 + a_{\mathsf{T}_{1,\mathsf{B}'}} \mathbf{m}_{\mathsf{T}_{1,\mathsf{B}'}}^2 \big]. \end{aligned} \tag{5.21}$$

order parameter	definition in terms of local spin components
m_{A_2}	$\frac{1}{2}\left(\mathsf{S}_0^z+\mathsf{S}_1^z+\mathsf{S}_2^z+\mathsf{S}_3^z\right)$
$\mathbf{m}_{\mathsf{E}}$	$\frac{1}{2}\begin{pmatrix}\mathsf{S}_0^x+\mathsf{S}_1^x+\mathsf{S}_2^x+\mathsf{S}_3^x\\ \mathsf{S}_0^y+\mathsf{S}_1^y+\mathsf{S}_2^y+\mathsf{S}_3^y\end{pmatrix}$
$\mathbf{m}_{\mathsf{T}_{1,\mathsf{A}}}$	$\begin{pmatrix}\frac{1}{2\sqrt{3}}(-\sqrt{2}\mathsf{S}_0^x+\mathsf{S}_0^z-\sqrt{2}\mathsf{S}_1^x+\mathsf{S}_1^z+\sqrt{2}\mathsf{S}_2^x-\mathsf{S}_2^z+\sqrt{2}\mathsf{S}_3^x-\mathsf{S}_3^z)\\ \frac{1}{12}(\sqrt{6}\mathsf{S}_0^x-3\sqrt{2}\mathsf{S}_0^y+2\sqrt{3}\mathsf{S}_0^z-\sqrt{6}\mathsf{S}_1^x+3\sqrt{2}\mathsf{S}_1^y-2\sqrt{3}\mathsf{S}_1^z+\sqrt{6}\mathsf{S}_2^x-3\sqrt{2}\mathsf{S}_2^y+2\sqrt{3}\mathsf{S}_2^z-\sqrt{6}\mathsf{S}_3^x+3\sqrt{2}\mathsf{S}_3^y-2\sqrt{3}\mathsf{S}_3^z)\\ \frac{1}{12}(\sqrt{6}\mathsf{S}_0^x+3\sqrt{2}\mathsf{S}_0^y+2\sqrt{3}\mathsf{S}_0^z-\sqrt{6}\mathsf{S}_1^x-3\sqrt{2}\mathsf{S}_1^y-2\sqrt{3}\mathsf{S}_1^z-\sqrt{6}\mathsf{S}_2^x-3\sqrt{2}\mathsf{S}_2^y-2\sqrt{3}\mathsf{S}_2^z+\sqrt{6}\mathsf{S}_3^x+3\sqrt{2}\mathsf{S}_3^y+2\sqrt{3}\mathsf{S}_3^z)\end{pmatrix}$
$\mathbf{m}_{\mathsf{T}_{1,\mathsf{B}}}$	$\begin{pmatrix}\frac{1}{2\sqrt{3}}(-\sqrt{2}\mathsf{S}_0^x-\mathsf{S}_0^z-\sqrt{2}\mathsf{S}_1^x-\mathsf{S}_1^z+\sqrt{2}\mathsf{S}_2^x+\mathsf{S}_2^z+\sqrt{2}\mathsf{S}_3^x+\mathsf{S}_3^z)\\ \frac{1}{12}(\sqrt{6}\mathsf{S}_0^x-3\sqrt{2}\mathsf{S}_0^y-2\sqrt{3}\mathsf{S}_0^z-\sqrt{6}\mathsf{S}_1^x+3\sqrt{2}\mathsf{S}_1^y+2\sqrt{3}\mathsf{S}_1^z+\sqrt{6}\mathsf{S}_2^x-3\sqrt{2}\mathsf{S}_2^y-2\sqrt{3}\mathsf{S}_2^z-\sqrt{6}\mathsf{S}_3^x+3\sqrt{2}\mathsf{S}_3^y+2\sqrt{3}\mathsf{S}_3^z)\\ \frac{1}{12}(\sqrt{6}\mathsf{S}_0^x+3\sqrt{2}\mathsf{S}_0^y-2\sqrt{3}\mathsf{S}_0^z-\sqrt{6}\mathsf{S}_1^x-3\sqrt{2}\mathsf{S}_1^y+2\sqrt{3}\mathsf{S}_1^z-\sqrt{6}\mathsf{S}_2^x-3\sqrt{2}\mathsf{S}_2^y+2\sqrt{3}\mathsf{S}_2^z+\sqrt{6}\mathsf{S}_3^x+3\sqrt{2}\mathsf{S}_3^y-2\sqrt{3}\mathsf{S}_3^z)\end{pmatrix}$
$\mathbf{m}_{\mathsf{T}_2}$	$\begin{pmatrix}\frac{1}{2}\left(-\mathsf{S}_0^y-\mathsf{S}_1^y+\mathsf{S}_2^y+\mathsf{S}_3^y\right)\\ \frac{1}{4}\left(\sqrt{3}\mathsf{S}_0^x+\mathsf{S}_0^y-\sqrt{3}\mathsf{S}_1^x-\mathsf{S}_1^y+\sqrt{3}\mathsf{S}_2^x+\mathsf{S}_2^y-\sqrt{3}\mathsf{S}_3^x-\mathsf{S}_3^y\right)\\ \frac{1}{4}\left(-\sqrt{3}\mathsf{S}_0^x+\mathsf{S}_0^y+\sqrt{3}\mathsf{S}_1^x-\mathsf{S}_1^y+\sqrt{3}\mathsf{S}_2^x-\mathsf{S}_2^y-\sqrt{3}\mathsf{S}_3^x+\mathsf{S}_3^y\right)\end{pmatrix}$

Table 5.3: Order parameters $\mathbf{m}_\lambda$, describing how the point-group symmetry of a single tetrahedron within the pyrochlore lattice is broken by magnetic order. Order parameters are irreducible representations of the point-group T_d, and are expressed in terms of linear combinations of spin-components $\mathsf{S}_i = (\mathsf{S}_i^x, \mathsf{S}_i^y, \mathsf{S}_i^z)$, in the local frame of the magnetic ions — cf. $\mathcal{H}_{\mathsf{ex}}^{\mathsf{local}}$ [Eq. (5.8)]. For convenience, in this table, the local axes $(x^{\mathsf{local}}, y^{\mathsf{local}}, z^{\mathsf{local}})$ are simply written (x, y, z). Labelling of spins within the tetrahedron follows the convention of Ross *et al.* [190] — cf. Fig. 5.2. Table reproduced from Ref. [188].

with coefficients given in Table 5.4. Here we emphasize that $\mathcal{H}_{\mathsf{ex}}^{[\mathsf{T}_\mathsf{d}]}$ [Eq. (5.21)] is an *exact transcription* of $\mathcal{H}_{\mathsf{ex}}^{\mathsf{tet}}$ [Eq. (5.16)] and *not* a phenomenological Landau theory. As such, $\mathcal{H}_{\mathsf{ex}}^{[\mathsf{T}_\mathsf{d}]}$ [Eq. (5.21)] is still subject to the constraint that every classical O(3) spin has fixed length, but now written in a complicated form in terms of $\mathbf{m}_\lambda$

For the majority of the discussion in this chapter, we are concerned with classical vectors $\mathbf{S}_i$ representing a (pseudo)spin-1/2, with

$$S = 1/2\,, \tag{5.22}$$

in which case the spin-norm constraint is

$$|\mathbf{S}_i|^2 = 1/4\,. \tag{5.23}$$

For the four spins on a single tetrahedron, we express the four constraints as

$$\begin{aligned}
\mathbf{S}_0^2+\mathbf{S}_1^2+\mathbf{S}_2^2+\mathbf{S}_3^2 &= 1\\
\mathbf{S}_0^2+\mathbf{S}_1^2-\mathbf{S}_2^2-\mathbf{S}_3^2 &= 0\\
\mathbf{S}_0^2-\mathbf{S}_1^2+\mathbf{S}_2^2-\mathbf{S}_3^2 &= 0\\
\mathbf{S}_0^2-\mathbf{S}_1^2-\mathbf{S}_2^2+\mathbf{S}_3^2 &= 0\,.
\end{aligned} \tag{5.24}$$

The constraints of fixed spin-length, Eq. (5.24), plays a crucial role in determining the allowed classical ground states, as we will discuss below.

A note to add here is that the addition of a single–ion anisotropy term $-D(\mathbf{S}\cdot\mathbf{z}_i^{\mathsf{local}})^2$ can also be included in the analysis by a simple modification of the coefficients a_λ in

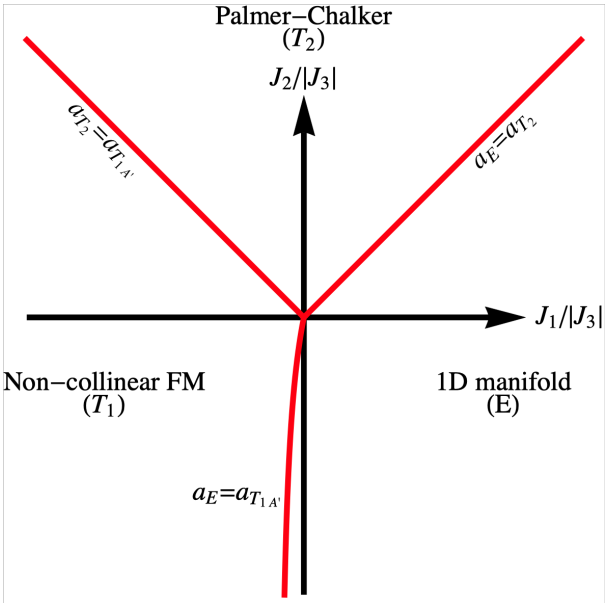

Figure 5.4: Classical ground state phase diagram of $\mathcal{H}_{\mathrm{ex}}$ [Eq. (5.3)] for $J_3 < 0$, $J_4 = 0$, as a function of $(J_1, J_2)/|J_3|$. In the absence of fluctuations, the ground states are a non-collinear FM transforming with the T_1 irrep of T_d; a one–dimensional manifold of states transforming with the E irrep of T_d; and the Palmer–Chalker phase, a coplanar antiferromagnet transforming with the T_2 irrep of T_d. All three phases have long-range 4-sublattice order. Analytical expressions for the boundaries between phases are given in Eq. (5.29–5.31), with coefficients a_λ defined in Table 5.4. Figure reproduced from Ref. [188].

$\mathcal{H}_{\mathrm{ex}}^{[\mathsf{T}_\mathsf{d}]}$ [Eq. (5.21)], So it does not affect any of the conclusions reached about ground states in the rest of this section. However, since interactions of this form contribute only to a trivial energy constant for a Kramers doublet, we will ignore this point further here.

5.3.2 General considerations

Given the existence of at least one classical ground state with $\mathbf{q} = 0$, 4-sublattice order, it is straightforward to determine the ground-state phase diagram directly from the diagonalized Hamiltonian $\mathcal{H}_{\mathrm{ex}}^{[\mathsf{T}_\mathsf{d}]}$ [Eq. (5.21)]. The method developed in what follows is very general and can be applied for arbitrary (J_1, J_2, J_3, J_4). However, for concreteness, we concentrate on the case

$$J_3 < 0\,,\ J_4 \equiv 0\,, \tag{5.25}$$

which is of particular experimental relevance to known pyrochlore materials, leading to the phase diagrams shown in Fig. 5.4, Fig. 5.5 and Fig. 5.6.

The classical ground states of $\mathcal{H}_{\mathrm{ex}}^{[\mathsf{T}_\mathsf{d}]}$ [Eq. (5.21)] can be found by the following procedure. First we identify the irrep λ^* for which a_{λ^*} takes on the minimum value among

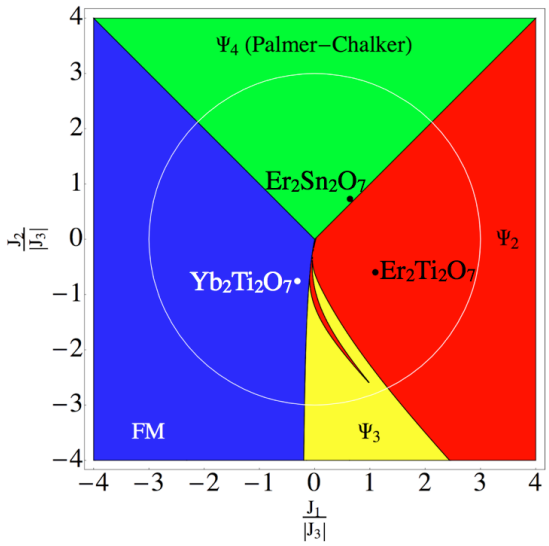

Figure 5.5: Classical ground-state phase diagram for a pyrochlore magnet with anisotropic exchange interactions. The model considered is the most general nearest–neighbour exchange Hamiltonian on the pyrochlore lattice $\mathcal{H}_{\text{ex}}$ [Eq. (5.3)], with symmetric off-diagonal exchange $J_3 < 0$, and vanishing Dzyaloshinskii-Moriya interactions ($J_4 = 0$). There are four distinct ordered phases, illustrated in the insets of Fig. 5.6. Points correspond to published estimates of parameters for $Yb_2Ti_2O_7$ [[190]], $Er_2Ti_2O_7$ [[166]], and $Er_2Sn_2O_7$ [[171]], setting $J_4 = 0$. The white circle corresponds to the path through parameter space shown in Fig. 5.6. Figure reproduced from Ref. [188].

coefficient of $\lvert\mathbf{m}_\lambda\rvert^2$	definition in terms of parameters of $\mathcal{H}_{\text{ex}}$ [Eq. (5.3)]	definition in terms of parameters of $\mathcal{H}_{\text{ex}}^{\text{local}}$ [Eq. (5.8)]
a_{A_2}	$-2J_1 + J_2 - 2(J_3 + 2J_4)$	$3J_{zz}$
a_{E}	$-2J_1 + J_2 + J_3 + 2J_4$	$-6J_{\pm}$
a_{T_2}	$-J_2 + J_3 - 2J_4$	$2J_{\pm} - 4J_{\pm\pm}$
$a_{\mathsf{T}_{1,\mathsf{A}'}}$	$(2J_1 + J_2)\cos^2(\theta_{\mathsf{T}_1})$ $-(J_2 + J_3 - 2J_4)\sin^2(\theta_{\mathsf{T}_1})$ $+\sqrt{2}J_3\sin(2\theta_{\mathsf{T}_1})$	$\frac{1}{3}(4J_{\pm} + 8J_{\pm\pm} + 8\sqrt{2}J_{z\pm} - J_{zz})\cos^2(\theta_{\mathsf{T}_1})$ $+\frac{2}{3}(1J_{\pm} + 2J_{\pm\pm} - 4\sqrt{2}J_{z\pm} - J_{zz})\sin^2(\theta_{\mathsf{T}_1})$ $+\frac{\sqrt{2}}{3}(-2J_{\pm} - 4J_{\pm\pm} + 2\sqrt{2}J_{z\pm} - J_{zz})\sin(2\theta_{\mathsf{T}_1})$
$a_{\mathsf{T}_{1,\mathsf{B}'}}$	$(2J_1 + J_2)\sin^2(\theta_{\mathsf{T}_1}) -$ $(J_2 + J_3 - 2J_4)\cos^2(\theta_{\mathsf{T}_1})$ $-\sqrt{2}J_3\sin(2\theta_{\mathsf{T}_1})$	$\frac{1}{3}(4J_{\pm} + 8J_{\pm\pm} + 8\sqrt{2}J_{z\pm} - J_{zz})\sin^2(\theta_{\mathsf{T}_1})$ $-\frac{2}{3}(1J_{\pm} + 2J_{\pm\pm} - 4\sqrt{2}J_{z\pm} - J_{zz})\cos^2(\theta_{\mathsf{T}_1})$ $-\frac{\sqrt{2}}{3}(-2J_{\pm} - 4J_{\pm\pm} + 2\sqrt{2}J_{z\pm} - J_{zz})\sin(2\theta_{\mathsf{T}_1})$

Table 5.4: Coefficients a_λ of the scalar invariants $\lvert\mathbf{m}_\lambda\rvert^2$ appearing in $\mathcal{H}_{\text{ex}}^{[\mathsf{T}_d]}$ [Eq. (5.21)]. Coefficients are expressed as a function of (J_1, J_2, J_3, J_4), the parameters of $\mathcal{H}_{\text{ex}}$ [Eq. (5.3)]; and (J_{zz}, $J_{\pm}$, $J_{\pm\pm}$, $J_{z\pm}$), the parameters of $\mathcal{H}_{\text{ex}}^{\text{local}}$ [Eq. (5.8)], with the canting angle θ_{T_1} defined in Eq. (5.20). The classical ground states of $\mathcal{H}_{\text{ex}}$ [Eq. (5.3)] can be found by identifying the coefficient(s) a_λ with the lowest value, and imposing the constraint of fixed spin-length, Eq. (5.24), on the associated $\mathbf{m}_\lambda$. Table reproduced from Ref. [188].

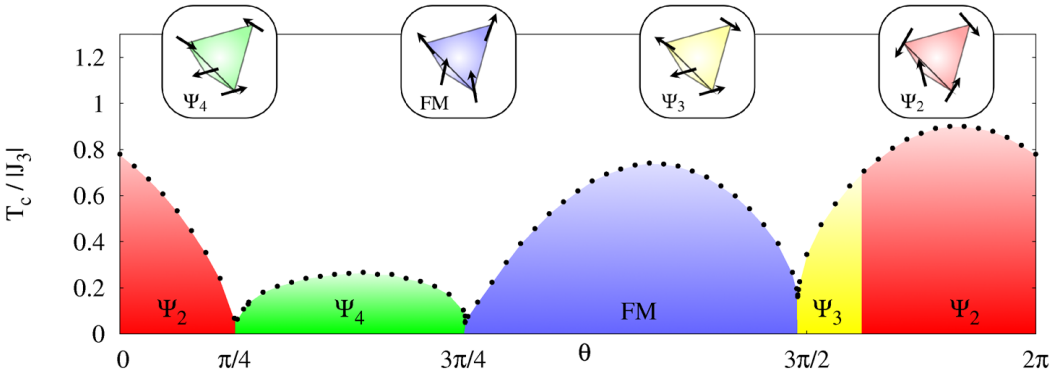

Figure 5.6: Finite-temperature phase diagram for a pyrochlore magnet with anisotropic exchange interactions. The model considered is $\mathcal{H}_{\mathsf{ex}}$ [Eq. (5.3)], with $J_1 = 3|J_3|\cos\theta$, $J_2 = 3|J_3|\sin\theta$, $J_3 < 0$, and $J_4 \equiv 0$, corresponding to the white circle in Fig. 5.5. Points show finite temperature phase transitions found from classical Monte Carlo simulations. The four ordered phases, Palmer–Chalker (Ψ_4), non-collinear ferromagnetic (FM), coplanar antiferromagnetic (Ψ_3) and non-coplanar antiferromagnetic (Ψ_2), are illustrated at the top of the figure. Each of these phases is six-fold degenerate, with zero crystal momentum, and is completely specified by the spin configuration in a single tetrahedron. Figure reproduced from Ref. [188].

all a_λ. Then we impose the constraint on the total length of the spin [Eq. (5.24)] on $\mathbf{m}_{\lambda^*}$, which implies that

$$m^2_{\mathsf{A}_2} + \mathbf{m}^2_{\mathsf{E}} + \mathbf{m}^2_{\mathsf{T}_2} + \mathbf{m}^2_{\mathsf{T}_{1,\mathsf{A}'}} + \mathbf{m}^2_{\mathsf{T}_{1,\mathsf{B}'}} \equiv \sum_\lambda \mathbf{m}^2_\lambda = 1 \,. \tag{5.26}$$

Such an approach is viable because each individual order parameter $\mathbf{m}_\lambda$ (or the norm of it) can reach its maximum value of 1 within physical spin configurations

$$\max \mathbf{m}^2_\lambda = 1 \,. \tag{5.27}$$

This method of determining the classical ground state is completely general and, once generalized to the lattice, is not restricted to conventionally ordered states [178, 181].

If a single a_{λ^*} takes on the minimum value, then the ground state corresponds to

$$\mathbf{m}^2_{\lambda^*} = 1, \qquad \text{for other } \lambda\text{s } \mathbf{m}^2_\lambda = 0 \tag{5.28}$$

In the case $J_3 < 0$, $J_4 \equiv 0$, the coefficients a_λ with the lowest values can be a_{E}, $a_{\mathsf{T}_{1\mathsf{A}'}}$, or a_{T_2}, and the corresponding $\mathbf{q} = 0$ ordered ground states have E, T_1 and T_2 symmetry.

The boundaries between these phases occur where

$$\begin{aligned} a_{\mathsf{T}_2} &= a_{\mathsf{E}} < a_{\mathsf{T}_2},\ a_{\mathsf{T}_{1\mathsf{B}'}},\ a_{\mathsf{A}_2} \\ &\Rightarrow J_2 = J_1 > 0 \qquad (5.29) \\ a_{\mathsf{T}_2} &= a_{\mathsf{T}_{1,\mathsf{A}'}} < a_{\mathsf{E}},\ a_{\mathsf{T}_{1\mathsf{B}'}},\ a_{\mathsf{A}_2} \\ &\Rightarrow J_2 = -J_1 > 0 \qquad (5.30) \\ a_{\mathsf{E}} &= a_{\mathsf{T}_{1,\mathsf{A}'}} < a_{\mathsf{T}_2},\ a_{\mathsf{T}_{1\mathsf{B}'}},\ a_{\mathsf{A}_2} \\ &\Rightarrow J_2 = \frac{J_1(4J_1 - 5J_3)}{4J_1 - J_3} < 0 \qquad (5.31) \end{aligned}$$

as illustrated in Fig. 5.4. This is the phase diagram for the classical system at $T = 0$ exactly.

In the following, we study the classical ground states with E, T_1 and T_2 symmetry in more detail, paying particular attention to the physics on phase boundaries. There we have degenerate a_{λ^1} and a_{λ^2} that are both minimal, hence more than one order parameter can take on a finite value,. The case of "all–in, all out" ground state is not considered here. It is a simple Ising–type order with two degenerate ground states. "All–in, all out" order has a finite value of the order parameter m_{A_2} [cf Table 5.3], which requires a_{A_2} to be the lowest coefficient. This only occurs for $J_4 > 0$ and/or $J_3 > 0$, and so falls outside the interested phase diagram of this chapter.

5.3.3 Non-collinear FM with T_1 symmetry

We start by studying what happens when interactions are predominantly ferromagnetic (i.e. $J_1, J_2 < 0$), as in $Yb_2Ti_2O_7$ [190] — cf. Table 5.5. For most of this region, as might be expected, the classical ground state configuration is a state with a finite magnetisation. This is the ground state throughout the region bounded by $a_{\mathsf{T}_{1,\mathsf{A}'}} = a_{\mathsf{T}_2}$ [Eq. (5.30)] , and $a_{\mathsf{T}_{1,\mathsf{A}'}} = a_{\mathsf{E}}$ [Eq. (5.31)] — cf. Fig. 5.4. Here the energy is minimised by requiring

$$\mathbf{m}^2_{\mathsf{T}_{1,\mathsf{A}'}} = 1 \qquad (5.32)$$

and

$$m_{\mathsf{A}_2} = \mathbf{m}_{\mathsf{E}} = \mathbf{m}_{\mathsf{T}_2} = \mathbf{m}_{\mathsf{T}_{1\mathsf{B}'}} = 0 \qquad (5.33)$$

Furthermore, the constraints on the spin lengths [Eq. (5.24)] imply that

$$\begin{aligned} m^y_{\mathsf{T}_{1\mathsf{A}'}} m^z_{\mathsf{T}_{1\mathsf{A}'}} &= 0 \\ m^x_{\mathsf{T}_{1\mathsf{A}'}} m^z_{\mathsf{T}_{1\mathsf{A}'}} &= 0 \\ m^x_{\mathsf{T}_{1\mathsf{A}'}} m^y_{\mathsf{T}_{1\mathsf{A}'}} &= 0. \qquad (5.34) \end{aligned}$$

Hence there are 6 possible ground states

$$\mathbf{m}_{\mathsf{T}_{1\mathsf{A}'}} = \begin{pmatrix} \pm 1 \\ 0 \\ 0 \end{pmatrix}, \begin{pmatrix} 0 \\ \pm 1 \\ 0 \end{pmatrix}, \begin{pmatrix} 0 \\ 0 \\ \pm 1 \end{pmatrix}. \qquad (5.35)$$

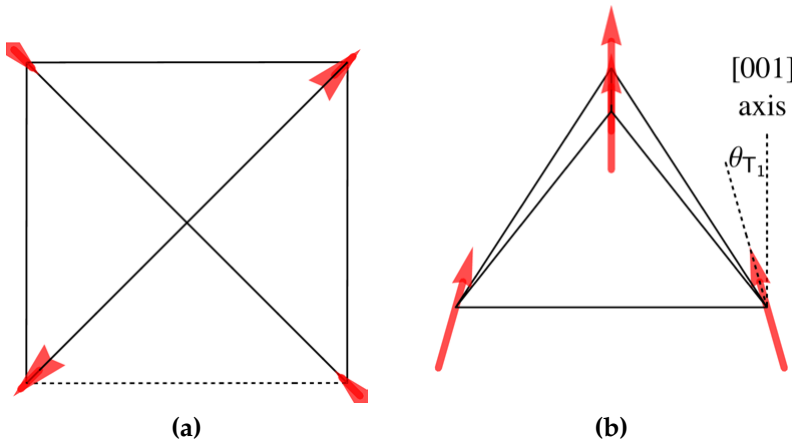

Figure 5.7: Spin-configuration in the 4-sublattice non-collinear FM phase, transforming with the T_1 irrep of T_d : (a) viewed along the [001] axis; (b) viewed slightly off the [110] axis. The magnetisation is aligned with the [001] axis. Spins are canted into the plane perpendicular to this, with canting angle θ_{T_1}. The canting is of an "ice-like" form such that the projection of the spin configuration onto a [001] plane has two spins oriented into the tetrahedron and two oriented out, as shown in (a). Figure reproduced from Ref. [188].

Translating back in terms of spins, these are 6, non-collinear ferromagnetic (FM) ground states, with typical spin configuration

$$\begin{aligned}
\mathbf{S}_0 &= S\left(\sin\theta_{T_1}/\sqrt{2}, \sin\theta_{T_1}/\sqrt{2}, \cos\theta_{T_1}\right) \\
\mathbf{S}_1 &= S\left(-\sin\theta_{T_1}/\sqrt{2}, \sin\theta_{T_1}/\sqrt{2}, \cos\theta_{T_1}\right) \\
\mathbf{S}_2 &= S\left(\sin\theta_{T_1}/\sqrt{2}, -\sin\theta_{T_1}/\sqrt{2}, \cos\theta_{T_1}\right) \\
\mathbf{S}_3 &= S\left(-\sin\theta_{T_1}/\sqrt{2}, -\sin\theta_{T_1}/\sqrt{2}, \cos\theta_{T_1}\right)
\end{aligned} \tag{5.36}$$

where θ_{T_1} is given by Eq. (5.20) and, following Eq. (5.22), $S = 1/2$.

The magnetisation of this FM ground state, illustrated in Fig. 5.7, is parallel to the [001] axis. But the spins are canted away from this axis, in an "ice-like" manner, so their canting cancel out. This state has been identified as the ground state in $Yb_2Sn_2O_7$, where it was referred to as a "splayed FM" [174]. It is also observed in most samples of $Yb_2Ti_2O_7$ which order at low temperature [164, 195–201] although a different form of canting has been reported in Ref. [202]. It is also the observed ordered state of the Tb based pyrochlore $Tb_2Sn_2O_7$ [203, 204].

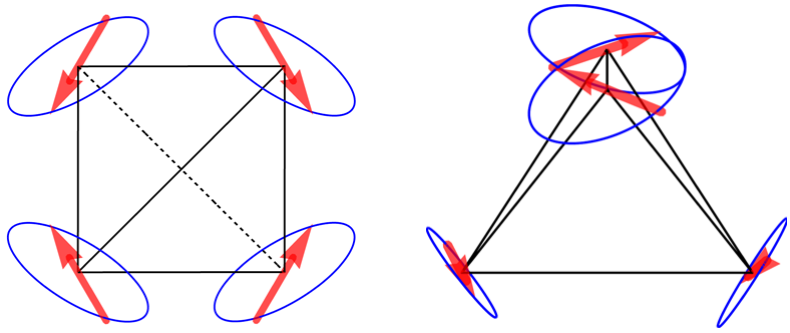

Figure 5.8: Example of a spin configuration within the one–dimensional manifold of states transforming with the E irrep of T_d : (a) viewed along [001] axis; (b) viewed slightly off the [110] axis. The manifold possesses 4-sublattice long-range order, with spins lying in the "XY" plane perpendicular to the local [111] axis at each site. The manifold is continuous, and can be parameterised with a single angle θ_{E}. The manifold can be generated by a clockwise rotation of all spins around their respective local axes. Figure reproduced from Ref. [188].

5.3.4 One–dimensional manifold of states with E symmetry

For a wide range of parameters with predominant antiferromagnetic "XY" interactions $J_1 > 0$, the classical ground state of $\mathcal{H}_{\mathsf{ex}}^{[\mathsf{T_d}]}$ [Eq. (5.21)] is a one–dimensional manifold of states which transforms with the E irrep of T_d. These ground states occur in a region bounded by $a_{\mathsf{E}} = a_{\mathsf{T}_{1,\mathsf{A}'}}$ [Eq. (5.31)] and $a_{\mathsf{E}} = a_{\mathsf{T}_2}$ [Eq. (5.29)] [Fig. 5.4] and is characterised by spins lying in the local "XY" plane normal to the local z-axis in [111]-direction on each site [cf Eqs. (5.7,5.7,5.7)].

For this range of parameters, the classical ground state energy can be minimised by setting

$$\mathbf{m}_{\mathsf{E}}^2 = 1 \tag{5.37}$$

and

$$m_{\mathsf{A}_2} = \mathbf{m}_{\mathsf{T}_2} = \mathbf{m}_{\mathsf{T}_{1\mathsf{A}'}} = \mathbf{m}_{\mathsf{T}_{1\mathsf{B}'}} = 0 \,. \tag{5.38}$$

These solutions *automatically* satisfy all the constraints on the total length of the spin Eq. (5.24) and can be conveniently parametrized by θ_{E} as

$$\mathbf{m}_{\mathsf{E}} = \left(\cos\theta_{\mathsf{E}},\, \sin\theta_{\mathsf{E}}\right) . \tag{5.39}$$

Therefore, the ground state is a continuous, one–dimensional manifold of states parameterised by the single angle $0 \leq \theta_{\mathsf{E}} < 2\pi$. The spin configuration in this manifold

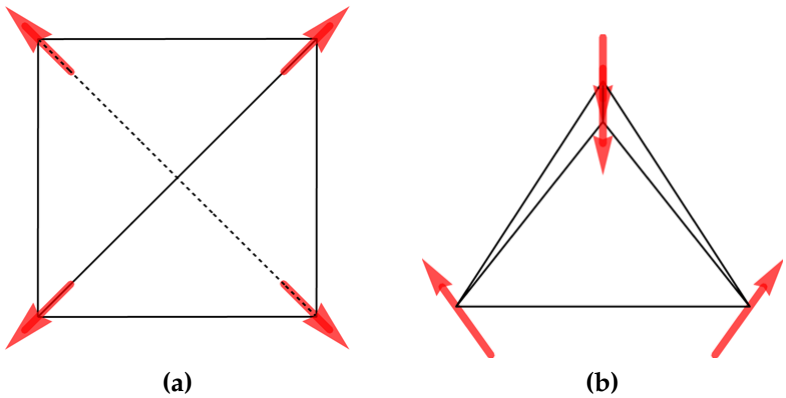

Figure 5.9: Spin configuration in the 4-sublattice non-coplanar antiferromagnet, Ψ_2, selected by fluctuations from the one–dimensional manifold of states transforming with E : (a) viewed along [001] axis; (b) viewed slightly off the [110] axis. At the phase boundary with the Palmer–Chalker phase, each of the six Ψ_2 ground states can be transformed continuously into a Palmer–Chalker state without leaving the ground–state manifold. Figure reproduced from Ref. [188].

is given by

$$\begin{aligned}
\mathbf{S}_0 &= S\Big(\sqrt{\frac{2}{3}}\cos(\theta_{\mathsf{E}}),\ \sqrt{\frac{2}{3}}\cos(\theta_{\mathsf{E}}+\frac{2\pi}{3}),\ \sqrt{\frac{2}{3}}\cos(\theta_{\mathsf{E}}-\frac{2\pi}{3})\Big)\\
\mathbf{S}_1 &= S\Big(\sqrt{\frac{2}{3}}\cos(\theta_{\mathsf{E}}),\ -\sqrt{\frac{2}{3}}\cos(\theta_{\mathsf{E}}+\frac{2\pi}{3}),\ -\sqrt{\frac{2}{3}}\cos(\theta_{\mathsf{E}}-\frac{2\pi}{3})\Big)\\
\mathbf{S}_2 &= S\Big(-\sqrt{\frac{2}{3}}\cos(\theta_{\mathsf{E}}),\ \sqrt{\frac{2}{3}}\cos(\theta_{\mathsf{E}}+\frac{2\pi}{3}),\ -\sqrt{\frac{2}{3}}\cos(\theta_{\mathsf{E}}-\frac{2\pi}{3})\Big)\\
\mathbf{S}_3 &= S\Big(-\sqrt{\frac{2}{3}}\cos(\theta_{\mathsf{E}}),\ -\sqrt{\frac{2}{3}}\cos(\theta_{\mathsf{E}}+\frac{2\pi}{3}),\ \sqrt{\frac{2}{3}}\cos(\theta_{\mathsf{E}}-\frac{2\pi}{3})\Big).
\end{aligned} \tag{5.40}$$

in which the spins lie in the local "XY" plane [cf. Eqs. (5.7) and (5.7)].

5.3.5 Non-coplanar antiferromagnet Ψ_2, with E symmetry

The degeneracy of the one-dimensional ground state manifold in the E symmetry is exact at zero temperature. However the system normally orders at small finite temperature, which requires additional analysis.

For example, it is now well–understood that for the model parametrized by $Er_2Ti_2O_7$, quantum fluctuations [166, 167, 191], classical thermal fluctuations at low temperature [165] and thermal fluctuations near the ordering temperature [168, 205] fluctuations all act within the one–dimensional manifold of classical ground states described in Section 5.3.4, to select a fixed non–coplanar antiferromagnet state in the one-dimensional manifold, Ψ_2, which is illustrated in Fig. (5.9). Structural disorder, meanwhile, favours

the coplanar antiferromagnet, Ψ_3 [206, 207], which are on other points of the one-dimensional manifold. It is illustrated in Fig. (5.10). Together, these two states Ψ_2 and Ψ_3 form a basis for the E irrep of T_d [192].

The Ψ_2 ground states are six-fold degenerate, with spins canted symmetrically out of the [100] plane. The six spin configurations for Ψ_2 states are the points of $\theta_{\mathsf{E}} = \frac{n\pi}{3}$, $n = 0, 1, 2 \ldots 5$ in Eq. (5.40).

The Ψ_2 state is characterised by the primary order parameter $\mathbf{m}_{\mathsf{E}}$ [cf. Table 5.2], and additionally by $c_{\mathsf{E}} > 0$, where (cf. Refs. [205, 208])

$$c_{\mathsf{E}} = \langle \cos 6\theta_{\mathsf{E}} \rangle. \tag{5.41}$$

Symmetry allows fluctuations to induce a finite value of m_{A_2} in the Ψ_2 phase [209], but classically this must vanish at $T \to 0$ since the energy is minimised by requiring$m_{\mathsf{A}_2} = 0$ within the region of phase diagram of the Ψ_2 state.

5.3.6 Coplanar antiferromagnet, Ψ_3, with E symmetry

For parameters bordering on the non-collinear FM phase, fluctuations select another state, the coplanar antiferromagnet, Ψ_3, out of the one–dimensional manifold of states of symmetry E. The Ψ_3 ground states are six-fold degenerate, with spins lying in a common [100] plane.

The six spin configurations for Ψ_3 states are the points of $\theta_{\mathsf{E}} = \frac{(2n+1)\pi}{6}$, $n = 0, 1, 2 \ldots 5$ in Eq. (5.40).

They are characterised by a finite value of the order parameter $\mathbf{m}_{\mathsf{E}}$ [cf Table 5.2], and additionally $c_{\mathsf{E}} < 0$ [cf. Eq. (5.41)]. An example of a typical spin configuration is shown in Fig. (5.10).

Taken together Ψ_2 and Ψ_3 form a complete basis for the E irrep of T_d.

5.3.7 Palmer–Chalker phase, Ψ_4, with T_2 symmetry

In a region bounded by $a_{\mathsf{T}_2} = a_{\mathsf{T}_{1,\mathsf{A}'}}$ [Eq. (5.30)] and $a_{\mathsf{T}_2} = a_{\mathsf{E}}$ [Eq. (5.29)] — cf. Fig. 5.4 — the energy is minimised by constraints

$$\mathbf{m}_{\mathsf{T}_2}^2 = 1 \tag{5.42}$$

and

$$m_{\mathsf{A}_2} = \mathbf{m}_{\mathsf{E}} = \mathbf{m}_{\mathsf{T}_{1\mathsf{A}'}} = \mathbf{m}_{\mathsf{T}_{1\mathsf{B}'}} = 0 \tag{5.43}$$

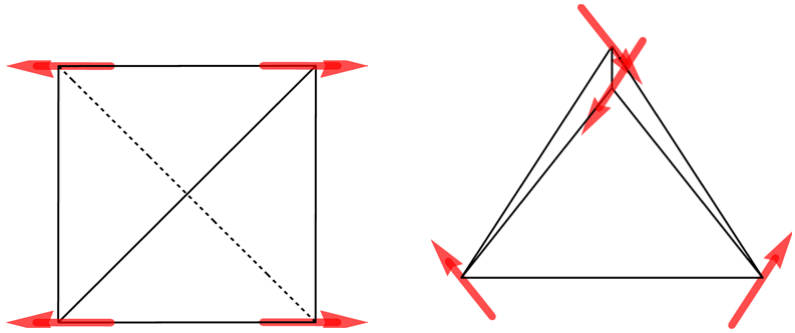

Figure 5.10: Spin configuration in the 4-sublattice coplanar antiferromagnet, Ψ_3, selected by fluctuations from the one–dimensional manifold of states transforming with E : (a) viewed along [001] axis; (b) viewed slightly off the [110] axis. At the phase boundary with the non-collinear FM phase, each of the six Ψ_3 ground states can be transformed continuously into a non-collinear FM state, without leaving the ground–state manifold. Figure reproduced from Ref. [188].

The constraints on the total length of the spin, Eq. (5.24), further imply that

$$\mathbf{m}^2_{\mathsf{T}_2} = 1 \tag{5.44}$$

$$m^y_{\mathsf{T}_2} m^z_{\mathsf{T}_2} = 0 \tag{5.45}$$

$$m^x_{\mathsf{T}_2} m^z_{\mathsf{T}_2} = 0 \tag{5.46}$$

$$m^x_{\mathsf{T}_2} m^y_{\mathsf{T}_2} = 0 \tag{5.47}$$

giving us a set of 6 degenerate ground states

$$\mathbf{m}_{\mathsf{T}_2} = \begin{pmatrix} \pm 1 \\ 0 \\ 0 \end{pmatrix}, \begin{pmatrix} 0 \\ \pm 1 \\ 0 \end{pmatrix}, \begin{pmatrix} 0 \\ 0 \\ \pm 1 \end{pmatrix}. \tag{5.48}$$

Within these ground states, spins are arranged in helical manner in a common [100] plane, with an example spin configuration given by (see Fig. 5.11).

$$\begin{aligned} \mathbf{S}_0 &= S\left(\frac{1}{\sqrt{2}}, -\frac{1}{\sqrt{2}}, 0\right) \\ \mathbf{S}_1 &= S\left(-\frac{1}{\sqrt{2}}, -\frac{1}{\sqrt{2}}, 0\right) \\ \mathbf{S}_2 &= S\left(\frac{1}{\sqrt{2}}, \frac{1}{\sqrt{2}}, 0\right) \\ \mathbf{S}_3 &= S\left(-\frac{1}{\sqrt{2}}, \frac{1}{\sqrt{2}}, 0\right) \end{aligned} \tag{5.49}$$

This phase is dubbed the "Palmer–Chalker" phase, first observed as the ground state of a model with antiferromagnetic nearest neighbour Heisenberg interactions and long-range dipolar interactions on the pyrochlore lattice [210]. The 6 degenerate ground

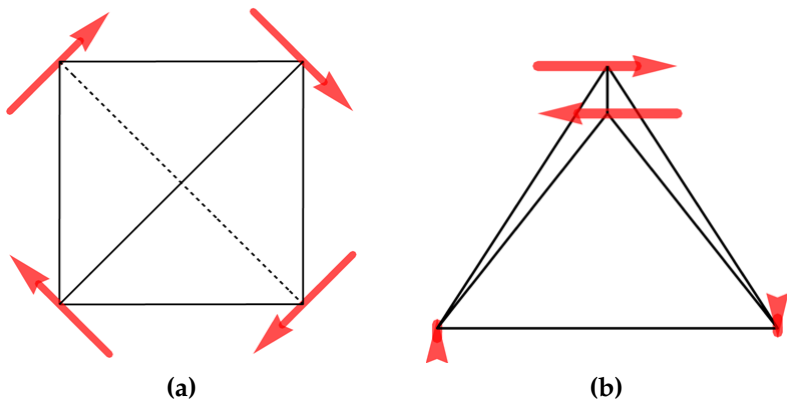

Figure 5.11: Spin configuration in the 4-sublattice Palmer–Chalker phase, Ψ_4, transforming with the T_2 irrep of T_d : (a) viewed along [001] axis; (b) viewed slightly off the [110] axis. At the phase boundary with the Ψ_2 phase, each of the six Palmer–Chalker ground states can be transformed continuously into a Ψ_2 state. Figure reproduced from Ref. [188].

states in this phase are also described by the basis vectors $\Psi_{4,5,6}$ [192], which are all equivalent by symmetry. For simplicity we refer to this phase as Ψ_4, but it should be noted that all three basis vectors $\Psi_{4,5,6}$ are equivalent ground states.

The Palmer-Chalker states are superficially similar to the Ψ_3 states [Sec. 5.3.6], since in both cases the states are coplanar, antiferromagnet configurations with all spins lying in a [100] plane. However, their symmetry properties must be different, since they transform according to different irreps of T_d. One example of the different symmetry properties is their transformation under the 3 C_2 rotations around $\langle 100 \rangle$ axes. The Ψ_3 configurations are invariant under all such rotations. The PC states are invariant under one of such rotations, i.e., the one around the axis normal to all the spins. But they reverse all spin orientations under the other two rotations.

5.3.8 Boundary between Palmer–Chalker phase and the one–dimensional manifold of states with E symmetry

So far we have identified all the ordered phases in the phase diagram. In the following, we will examine the more interesting physics on the phase boundary, where the degeneracy of ground states are enlarged.

The boundary between the Palmer–Chalker phase and the one–dimensional manifold of states with E symmetry are located on the line of $a_{\mathsf{E}} = a_{\mathsf{T}_2}$, and both of them being the minimal values [cf. Eq. (5.29)]. In this case, $\mathcal{H}_{\text{ex}}^{[\mathsf{T}_d]}$ [Eq. (5.21)] is minimized by constraints

$$\mathbf{m}_{\mathsf{E}}^2 + \mathbf{m}_{\mathsf{T}_2}^2 = 1 \tag{5.50}$$

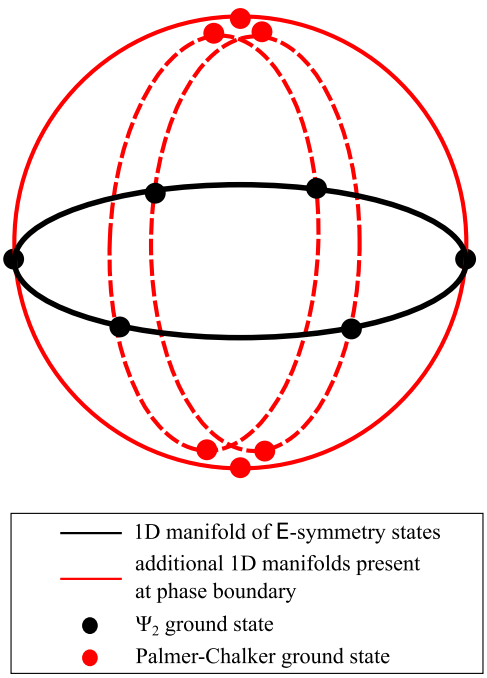

Figure 5.12: Structure of the ground state manifold at the boundary between the Palmer–Chalker (PC) phase and the one–dimensional manifold of states with E symmetry. The black circle denotes the manifold of E–symmetry ground states, including the six Ψ_2 ground states (black dots). At the boundary with the PC phase, this manifold branches at the Ψ_2 states, to connect with three, additional, one–dimensional manifolds. These manifolds in turn interpolate to the six Palmer–Chalker ground states with T_2 symmetry (red dots). An exactly equivalent picture holds on the boundary between the non-collinear ferromagnet (FM), and the one–dimensional manifold of states with E symmetry. However in this case the different manifolds intersect at the Ψ_3 states. Figure reproduced from Ref. [188].

and

$$m_{\mathsf{A}_2} = \mathbf{m}_{\mathsf{T}_{1\mathsf{A}'}} = \mathbf{m}_{\mathsf{T}_{1\mathsf{B}'}} = 0. \tag{5.51}$$

Substituting

$$\mathbf{m}_{\mathsf{E}} = m_{\mathsf{E}}(\cos\theta_{\mathsf{E}},\ \sin\theta_{\mathsf{E}})\ , \tag{5.52}$$

and imposing the constraint Eq. (5.24), we have

$$\begin{aligned} 2m_{\mathsf{E}}m^x_{\mathsf{T}_2}\sin(\theta_{\mathsf{E}}) - m^y_{\mathsf{T}_2}m^z_{\mathsf{T}_2} &= 0 \\ 2m_{\mathsf{E}}m^y_{\mathsf{T}_2}\sin\left(\theta_{\mathsf{E}} - \frac{2\pi}{3}\right) - m^x_{\mathsf{T}_2}m^z_{\mathsf{T}_2} &= 0 \\ 2m_{\mathsf{E}}m^z_{\mathsf{T}_2}\sin\left(\theta_{\mathsf{E}} + \frac{2\pi}{3}\right) - m^x_{\mathsf{T}_2}m^y_{\mathsf{T}_2} &= 0. \end{aligned} \tag{5.53}$$

It can be easily shown that there are no solutions to Eqs. (5.53) where more than one component of $\mathbf{m}_{\mathsf{T}_2}$ is finite. There are, however, three distinct one–dimensional manifolds emerging as the new ground states. They connect pairs of Palmer–Chalker states

to the one–dimensional manifold of E-symmetry states, and can be parametrized as

$$\mathbf{m}_{\mathsf{E}} = \cos(\alpha)\begin{pmatrix}1\\0\end{pmatrix},\ \mathbf{m}_{\mathsf{T}_2} = \sin(\alpha)\begin{pmatrix}1\\0\\0\end{pmatrix} \tag{5.54}$$

$$\mathbf{m}_{\mathsf{E}} = \cos(\beta)\begin{pmatrix}-\frac{1}{2}\\ \frac{\sqrt{3}}{2}\end{pmatrix},\ \mathbf{m}_{\mathsf{T}_2} = \sin(\beta)\begin{pmatrix}0\\1\\0\end{pmatrix} \tag{5.55}$$

$$\mathbf{m}_{\mathsf{E}} = \cos(\gamma)\begin{pmatrix}-\frac{1}{2}\\ -\frac{\sqrt{3}}{2}\end{pmatrix},\ \mathbf{m}_{\mathsf{T}_2} = \sin(\gamma)\begin{pmatrix}0\\0\\1\end{pmatrix} \tag{5.56}$$

where the angles α, β and γ run from 0 to 2π.

A spin configuration example for one of the three connecting manifolds is

$$\begin{aligned}
\mathbf{S}_0 &= S\sqrt{\frac{2}{3}}\left(-\cos(\alpha),\ \cos\left(\alpha+\frac{\pi}{3}\right),\ \cos\left(\alpha-\frac{\pi}{3}\right)\right)\\
\mathbf{S}_1 &= S\sqrt{\frac{2}{3}}\left(-\cos(\alpha),\ -\cos\left(\alpha+\frac{\pi}{3}\right),\ -\cos\left(\alpha-\frac{\pi}{3}\right)\right)\\
\mathbf{S}_2 &= S\sqrt{\frac{2}{3}}\left(\cos(\alpha),\ \cos\left(\alpha-\frac{\pi}{3}\right),\ -\cos\left(\alpha+\frac{\pi}{3}\right)\right),\\
\mathbf{S}_3 &= S\sqrt{\frac{2}{3}}\left(\cos(\alpha),\ -\cos\left(\alpha-\frac{\pi}{3}\right),\ \cos\left(\alpha+\frac{\pi}{3}\right)\right).
\end{aligned} \tag{5.57}$$

where $\alpha = 0, \pi$ are points of the Ψ_2 ground states with $\theta_{\mathsf{E}} = 0, \pi$, and $\alpha = \pi/2, 3\pi/2$ are points of the six Palmer–Chalker ground states. These manifolds are illustrated in Fig. 5.12.

Applying of the "Lego–brick" rules given in Section 5.2.5, the ground state degeneracy on this phase boundary is at least $\mathcal{O}(2^{L^2})$. This follows from the observation that, on the boundary, the Palmer–Chalker ground states Ψ_4 share two spin configurations with the neighbouring Ψ_3 states. This, in turn, is connected with the $\mathcal{O}(L^2)$ number of zero modes in the spin wave expansions around the Ψ_2 configurations.

We note that a special limit of this phase boundary is studied for strictly XY spins (i.e. with infinite easy–plane anisotropy) in Ref. [211], where the same structure of ground state manifolds was found.

5.3.9 Boundary between the non-collinear ferromagnet and the one–dimensional manifold of states with E symmetry

The boundary between the non-collinear ferromagnet and the one–dimensional manifold of states with E symmetry occurs when $a_{\mathsf{E}} = a_{\mathsf{T}_{1,\mathsf{A}'}}$ and both of them remain

minimal [cf. Eq. (5.31)]. In this case, $\mathcal{H}_{\mathsf{ex}}^{[\mathsf{T_d}]}$ [Eq. (5.21)] is minimised by constraints

$$\mathbf{m}^2_{\mathsf{T}_{1,\mathsf{A}'}} + \mathbf{m}^2_{\mathsf{E}} = 1 \tag{5.58}$$

and

$$m_{\mathsf{A}_2} = \mathbf{m}_{\mathsf{T}_{1,\mathsf{B}'}} = \mathbf{m}_{\mathsf{T}_2} = 0. \tag{5.59}$$

For simplicity, we define the quantities

$$\begin{aligned} \mu(\theta_{\mathsf{T}_1}) &= (\sqrt{2}\cos(\theta_{\mathsf{T}_1}) - \sin(\theta_{\mathsf{T}_1})) \\ \nu(\theta_{\mathsf{T}_1}) &= (\sin(\theta_{\mathsf{T}_1})^2 + \sqrt{2}\sin(2\theta_{\mathsf{T}_1})) \end{aligned} \tag{5.60}$$

and impose the constraint Eq. (5.24). We then obtain

$$\begin{aligned} 2m_{\mathsf{E}} m^x_{\mathsf{T}_{1,\mathsf{A}'}} \cos(\theta_{\mathsf{E}}) &= -\frac{\mu(\theta_{\mathsf{T}_{1,\mathsf{A}'}})}{\nu(\theta_{\mathsf{T}_{1,\mathsf{A}'}})} m^y_{\mathsf{T}_{1,\mathsf{A}'}} m^z_{\mathsf{T}_{1,\mathsf{A}'}} \\ 2m_{\mathsf{E}} m^y_{\mathsf{T}_{1,\mathsf{A}'}} \cos\left(\theta_{\mathsf{E}} - \frac{2\pi}{3}\right) &= -\frac{\mu(\theta_{\mathsf{T}_{1,\mathsf{A}'}})}{\nu(\theta_{\mathsf{T}_{1,\mathsf{A}'}})} m^x_{\mathsf{T}_{1,\mathsf{A}'}} m^z_{\mathsf{T}_{1,\mathsf{A}'}} \\ 2m_{\mathsf{E}} m^z_{\mathsf{T}_{1,\mathsf{A}'}} \cos\left(\theta_{\mathsf{E}} + \frac{2\pi}{3}\right) &= -\frac{\mu(\theta_{\mathsf{T}_{1,\mathsf{A}'}})}{\nu(\theta_{\mathsf{T}_{1,\mathsf{A}'}})} m^x_{\mathsf{T}_{1,\mathsf{A}'}} m^y_{\mathsf{T}_{1,\mathsf{A}'}} \end{aligned} \tag{5.61}$$

where θ_{T_1} is the fixed canting angle [Eq. (5.20)], and θ_{E} is the variable angle parameter for the U(1) manifold [Eq. (5.39)]. For the parameters considered here, the quantities $\mu(\theta_{\mathsf{T}_1})$ and $\nu(\theta_{\mathsf{T}_1})$ are always finite.

Enlarged ground state manifold isomorphic to those developed for the boundary with the Palmer–Chalker phase, give us three more 1D manifolds in addition to the one associated with the E phase. However, in this case the intersections of the manifolds are located at $\theta_{\mathsf{E}} = \frac{(2n+1)\pi}{6}$, corresponding to the Ψ_3 states. This qualitatively explains the model's general entropic preference for Ψ_3 states in the region proximate to the ferromagnetic phase.

A typical spin configuration for one of the three connecting manifolds, parameterised

by an angle η is

$$
\begin{aligned}
\mathbf{S}_0 &= S\Big(\cos(\theta_{\mathsf{T}_1})\sin(\eta),\ \frac{1}{\sqrt{2}}(-\cos(\eta)+\sin(\eta)\sin(\theta_{\mathsf{T}_1})),\\
&\quad \frac{1}{\sqrt{2}}(\cos(\eta)+\sin(\eta)\sin(\theta_{\mathsf{T}_1})\Big)\\
\mathbf{S}_1 &= S\Big(\cos(\theta_{\mathsf{T}_1})\sin(\eta),\ \frac{1}{\sqrt{2}}(\cos(\eta)-\sin(\eta)\sin(\theta_{\mathsf{T}_1})),\\
&\quad \frac{1}{\sqrt{2}}(-\cos(\eta)-\sin(\eta)\sin(\theta_{\mathsf{T}_1})\Big)\\
\mathbf{S}_2 &= S\Big(\cos(\theta_{\mathsf{T}_1})\sin(\eta),\ \frac{1}{\sqrt{2}}(-\cos(\eta)-\sin(\eta)\sin(\theta_{\mathsf{T}_1})),\\
&\quad \frac{1}{\sqrt{2}}(-\cos(\eta)+\sin(\eta)\sin(\theta_{\mathsf{T}_1})\Big)\\
\mathbf{S}_3 &= S\Big(\cos(\theta_{\mathsf{T}_1})\sin(\eta),\ \frac{1}{\sqrt{2}}(\cos(\eta)+\sin(\eta)\sin(\theta_{\mathsf{T}_1})),\\
&\quad \frac{1}{\sqrt{2}}(\cos(\eta)-\sin(\eta)\sin(\theta_{\mathsf{T}_1})\Big).
\end{aligned}
\tag{5.62}
$$

Here $\eta = 0$ corresponds to the Ψ_3 ground state with $\theta_{\mathsf{E}} = \pi/2$, and $\eta = \pi/2$ to one of the six FM ground states.

We noted that an equivalent ground–state manifold was studied by Canals and coauthors [212], and also by Chern [208], in the context the Heisenberg antiferromagnet with Dzyaloshinskii–Moriya interactions on the pyrochlore lattice. Their case corresponds to a single point on the phase boundary considered in this section.

5.3.10 Boundary between the Palmer–Chalker phase and the non-collinear ferromagnet

Finally, we study the boundary between the Palmer–Chalker phase and the non-collinear ferromagnet. It occurs when $a_{\mathsf{T}_2} = a_{\mathsf{T}_{1,\mathsf{A}'}}$ and are both minimal [cf. Eq. (5.30)]. In this case, $\mathcal{H}_{\mathsf{ex}}^{[\mathsf{T}_\mathsf{d}]}$ [Eq. (5.21)] is minimised by constraints

$$
\mathbf{m}_{\mathsf{T}_2}^2 + \mathbf{m}_{\mathsf{T}_{1,\mathsf{A}'}}^2 = 1
\tag{5.63}
$$

and

$$
m_{\mathsf{A}_2} = \mathbf{m}_{\mathsf{E}} = \mathbf{m}_{\mathsf{T}_{1,\mathsf{B}'}} = 0.
\tag{5.64}
$$

Imposing the constraint Eq. (5.24) we obtain a set of more complicated identities

$$\begin{aligned}
&-m^y_{\mathsf{T}_2} m^z_{\mathsf{T}_2} + (\sin(\theta_{\mathsf{T}_1})^2 + \sqrt{2}\sin(2\theta_{\mathsf{T}_1})) m^y_{\mathsf{T}_{1\mathsf{A}'}} m^z_{\mathsf{T}_{1\mathsf{A}'}} \\
&\quad + (\sqrt{2}\cos(\theta_{\mathsf{T}_1}) - \sin(\theta_{\mathsf{T}_1}))(\mathbf{m}_{\mathsf{T}_{1\mathsf{A}'}} \times \mathbf{m}_{\mathsf{T}_2})_x = 0 \\
&-m^x_{\mathsf{T}_2} m^z_{\mathsf{T}_2} + (\sin(\theta_{\mathsf{T}_1})^2 + \sqrt{2}\sin(2\theta_{\mathsf{T}_1})) m^x_{\mathsf{T}_{1\mathsf{A}'}} m^z_{\mathsf{T}_{1\mathsf{A}'}} \\
&\quad + (\sqrt{2}\cos(\theta_{\mathsf{T}_1}) - \sin(\theta_{\mathsf{T}_1}))(\mathbf{m}_{\mathsf{T}_{1\mathsf{A}'}} \times \mathbf{m}_{\mathsf{T}_2})_y = 0 \\
&-m^x_{\mathsf{T}_2} m^y_{\mathsf{T}_2} + (\sin(\theta_{\mathsf{T}_1})^2 + \sqrt{2}\sin(2\theta_{\mathsf{T}_1})) m^x_{\mathsf{T}_{1\mathsf{A}'}} m^y_{\mathsf{T}_{1\mathsf{A}'}} \\
&\quad + (\sqrt{2}\cos(\theta_{\mathsf{T}_1}) - \sin(\theta_{\mathsf{T}_1}))(\mathbf{m}_{\mathsf{T}_{1\mathsf{A}'}} \times \mathbf{m}_{\mathsf{T}_2})_z = 0
\end{aligned} \tag{5.65}$$

where θ_{T_1} is defined in Eq. (5.20).

We can show that the ground state manifold on the neighborhood of the Palmer–Chalker state points is locally two–dimensional. To see this, consider small deviations from a given solution

$$\begin{aligned}
\mathbf{m}_{\mathsf{T}_2} &= \mathbf{m}^0_{\mathsf{T}_2} + \delta\mathbf{m}_{\mathsf{T}_2} \\
\mathbf{m}_{\mathsf{T}_{1\mathsf{A}'}} &= \mathbf{m}^0_{\mathsf{T}_{1\mathsf{A}'}} + \delta\mathbf{m}_{\mathsf{T}_{1\mathsf{A}'}}
\end{aligned} \tag{5.66}$$

and expand the constraint Eq. (5.65) to linear order in $\delta\mathbf{m}$. Generally, we find two linearly–independent solutions for $(\delta\mathbf{m}_{\mathsf{T}_2}, \delta\mathbf{m}_{\mathsf{T}_{1\mathsf{A}'}})$, hence the manifold in the vicinity of $(\mathbf{m}^0_{\mathsf{T}_2}, \mathbf{m}^0_{\mathsf{T}_{1\mathsf{A}'}})$ is two–dimensional.

In contrast, if we expand around a state $(\tilde{\mathbf{m}}^0_{\mathsf{T}_2}, \tilde{\mathbf{m}}^0_{\mathsf{T}_{1\mathsf{A}'}})$ where *both* order parameters are aligned with the same cubic axis, e.g.

$$\tilde{m}^{0y}_{\mathsf{T}_2} = \tilde{m}^{0z}_{\mathsf{T}_2} = \tilde{m}^{0y}_{\mathsf{T}_{1\mathsf{A}'}} = \tilde{m}^{0z}_{\mathsf{T}_{1\mathsf{A}'}} = 0 \tag{5.67}$$

one of the Eqs. (5.65) is satisfied trivially, leaving three constraints acting on six variables. It means that the manifold is locally three-dimensional in the vicinity of $(\tilde{\mathbf{m}}^0_{\mathsf{T}_2}, \tilde{\mathbf{m}}^0_{\mathsf{T}_{1\mathsf{A}'}})$.

This set of ground states on the tetrahedron includes multiple states where one of the spins has the same direction. Following the "Lego–brick" rule described in Section 5.2.5, this means that neighbouring kagome planes can be decoupled in the ground state and there is a ground state degeneracy of at least $\mathcal{O}(2^L)$.

5.3.11 All–in, all–out order with A_2 symmetry

In the Sections 5.3.3-5.3.10 we have discussed the different types of ordered, classical ground state which can occur for $J_3 < 0, J_4 = 0$ and their phase boundaries in detail. A more general choice of parameters, with $J_4 > 0$ or $J_3 > 0$, allows for situations where the lowest parameter in $\mathcal{H}^{\mathsf{tet}}_{\mathsf{ex}}$ [Eq. (5.21)] is a_{A_2}.

	$Yb_2Ti_2O_7$ [190]	$Er_2Ti_2O_7$ [166]	$Er_2Sn_2O_7$ [171]
J_1	-0.09 meV	0.11 meV	0.07 meV
J_2	-0.22 meV	-0.06 meV	0.08 meV
J_3	-0.29 meV	-0.10 meV	-0.11 meV
J_4	0.01 meV	-0.003 meV	0.04 meV
J_{zz}	0.17 meV	-0.025 meV	0
$J_{\pm}$	0.05 meV	0.065 meV	0.014 meV
$J_{\pm\pm}$	0.05 meV	0.042 meV	0.074 meV
$J_{z\pm}$	-0.14 meV	-0.009 meV	0

Table 5.5: Estimates of the parameters for anisotropic near-neighbour exchange, taken from experiments on $Yb_2Ti_2O_7$ [190], $Er_2Ti_2O_7$ [166], and $Er_2Sn_2O_7$ [171]. Values are quoted for exchange interactions in both the crystal coordinate frame $\mathcal{H}_{\text{ex}}$ [Eq. (5.3)], and the local coordinate frame, $\mathcal{H}_{\text{ex}}^{\text{local}}$ [Eq. (5.8)], following the notation of Ross *et al.* [190]. An alternative set of parameters for $Yb_2Ti_2O_7$ has recently been proposed by Robert *et al.* [199]. Table reproduced from Ref. [188].

In this case, the ground state will have $\mathbf{q} = 0$ 4-sublattice order with a finite value of the order parameter m_{A_2} [Table 5.2]. As one can see from the definition of the order parameters, it is a type of order that is particularly simple, with all spins aligned along the local [111] axes, and all of them pointing either into, or out of, tetrahedra on the A-sublattice simultaneously. This type of order is commonly referred to as "all–in, all–out" state, and is observed in some pyrochlore magnets, including $Nd_2Zr_2O_7$ [213].

We will not discuss it further in here, except for mentioning the following fact. Since the order parameter m_{A_2} is a scalar, the finite–temperature phase transitions are expected to belong to the Ising universality class, in the absence of a first order phase transition.

5.4 Application to materials

The anisotropic nearest–neighbour exchange model studied in this chapter, $\mathcal{H}_{\text{ex}}$ [Eq. (5.3)], has been used to describe a number of pyrochlore oxides with considerable success.

In the case of $Yb_2Ti_2O_7$, $\mathcal{H}_{\text{ex}}$ [Eq. (5.3)] has been shown to give excellent descriptions of spin-wave spectra measured in magnetic field [190]. Thermodynamic quantities, calculated from $\mathcal{H}_{\text{ex}}$ [Eq. (5.3)] using the parameters from [190], also match well with experiments [214, 215].

Parameters for $Er_2Ti_2O_7$ have been extracted from similar inelastic neutron scattering experiments[166], and also from results of the field-dependence of magnetisation at low temperature [216]. The model $\mathcal{H}_{\text{ex}}$ [Eq. (5.3)], using parameters taken from neutron scattering [166], has been shown to give good agreement to the observed spin

wave spectrum in $Er_2Ti_2O_7$. It is consistent with quantum order–by–disorder scenario [166]. Anisotropic nearest–neighbour exchange parameters for $Er_2Sn_2O_7$ have also been estimated from tge magnetization curve measurements [171].

Representative estimates of the exchange parameters (J_1, J_2, J_3, J_4) taken from experiment on $Yb_2Ti_2O_7$ [190], $Er_2Ti_2O_7$ [166], and $Er_2Sn_2O_7$ [171], are listed in Table 5.5. The typical scale of interactions is at $|J| \sim 0.1$ meV (i.e. $|J| \sim 1$ K), with typical uncertainty estimated to be $\delta J \sim 0.02$ meV (i.e. $\delta J \sim 0.2$ K) [166, 171, 190]. In all of these cases, the off-diagonal exchange interaction J_3 is negative, and the Dzyaloshinskii-Moriya interaction J_4 is smaller.

Consequently, in $Yb_2Ti_2O_7$, we find ferromagnetic order close to the competing "Ψ_3" and "Ψ_2" states, which manifest themselves in the "rod" structures seen in neutron scattering. These "rod" structures implies very low energy cost for the system to tunnel into other states. Meanwhile, in $Er_2Ti_2O_7$, we find that the reason fluctuations select the well–established "Ψ_2" ground state [165–167], is its proximity to a neighboring Palmer–Chalker phase. And in the case of $Er_2Sn_2O_7$, we observe that fluctuations of Palmer–Chalker order predominate, but that all forms of magnetic order are strongly suppressed by its proximity of a degenerate ground-state manifold connected to neighbouring "Ψ_2" states.

Crucially, the core message is that the "accidental" degeneracies arising at boundaries of different phases with different symmetries play a critical role in determining the properties of these materials. The symmetry-based approach allows us to systematically explore the enlarged ground-state manifolds on these phase boundaries and determine the non-trivial physical effects.

The common theme which emerges is of systems "living on the edge" — the physical properties of materials showing one type of magnetic order being heavily influenced by the proximity of another, competing, ordered phase.

5.5 Conclusion

Rare-earth pyrochlore oxides are a veritable treasure trove for novel physical phenomena, ranging from classical and quantum spin liquids, to dimensional reduction, and phases governed by order–by–disorder effects. In this chapter we have constructed a general theory of the symmetry breaking order parameters, and used it to analyze the effects of multiple–phase competition in materials with anisotropic exchange interactions on the pyrochlore lattice. We have shown how it can be applied to explain the physics some specific materials : $Er_2Ti_2O_7$, $Yb_2Ti_2O_7$ and $Er_2Sn_2O_7$. The recurring theme throughout this analysis is of materials "living on the edge", in the sense of having properties which are dictated by the competition between neighbouring phases of magnetic order.

Starting from a very general model of interactions between nearest–neighbour spins on the pyrochlore lattice, $\mathcal{H}_{\mathsf{ex}}$ [Eq. (5.3)], we have used an analysis based on point–group symmetry to identify the order parameters, diagonalize the Hamiltonian, and finally establish the exact, classical, ground–state phase diagram [Sections 5.2 and 5.3]. We provide a complete classification of possible four–sublattice ordered states at $\mathbf{q} = 0$, according to the way they break the symmetry of a single tetrahedron. Moreover, using the "Lego–brick" rules explained in Section 5.2.5, we can to identify the conditions under which the classical ground state manifold undergoes dimensional reductions into independent planes or chains of spins, opening the door to exotic physical phenomena.

We have given particularly careful analysis of the ground–state manifolds in the case of the symmetric off diagonal exchange $J_3 < 0$ and the Dzyaloshinskii-Moriya interaction $J_4 = 0$ [Section 5.3]. From the experimental parameterisations of exchange interactions for multiple Kramers pyrochlores [166, 171, 190], this case is of particular experimental relevance. We have elucidated the nature of the enlarged ground state manifolds at the phase boundaries of this model, and shown that it is them that drive much of the physics of the surrounding regions of parameter space.

From a theoretical perspective, this work highlights the importance of large, ground–state degeneracies which are *not* related to the well–studied examples of spin ice, or of the Heisenberg antiferromagnet on a pyrochlore lattice. These degeneracies, which emerge in a number of different phase boundaries of $\mathcal{H}_{\mathsf{ex}}$ [Eq. (5.3)], could lead to novel physics of classical or quantum spin liquid, as well as entirely new forms of classical and quantum order [181]. One of such cases, where fluctuations lead to a spin–liquid described by a rank–2 tensor field with a continuous gauge symmetry, has been developed in Ref. [178]. In the next chapter, we will utilize the tools to develop the model that host rank-2 U(1) spin liquid physics.

Chapter 6

Rank-2 U(1) spin liquid on breathing pyrochlore lattice

6.1 Introduction

In previous chapter, we have built our analysis based on the symmetry breaking scenario. As we pointed out, the physics becomes more exotic on the boundary of two phases.

Generally, in each symmetry-breaking phase, the number of ground states is of order $\mathcal{O}(1)$, where the degeneracy comes from finite, discrete symmetries. In the case of 4-sublattice, $\boldsymbol{q} = 0$ order on the pyrochlore lattice, considered in Chapter. 5, the degeneracy is six-fold, coming from the cubic reflectional and rotational symmetries.

On the phase boundary where two (or more) phases meet, the ground state manifold is enlarged. It includes both the ground states in the two (or more) phases, and additional ones that connect them. Sometimes, the number of additional ground states is infinite in the thermodynamic limit. In some cases, the infinity of the ground-state number is measured by continuous, global symmetries, and does not scale with the volume of the system when the system size is finite. For example, see Sec. 5.3.4 in Chapter 5.

In more exceptional cases, the infinity is of higher order, and proportional to the exponential of the system volume for finite-sized systems. This implies that there are local operations that tunnel one ground state to another. For example, see spin ice introduced in Chapter 1. In these cases, the ground states are defined not by symmetry-breaking order parameters, but by local Gauss's law-like constraints on the fluctuating order parameters. These are the classical spin liquids.

As we explained, a classical spin liquid at $T = 0$ has an exponentially large ground state manifold. the ground states are constrained by the local Gauss's law, which is not enough to kill all degrees of freedom. It is thus an interesting question: how to

derive the Gauss's law from the symmetry breaking analysis?

Such advancement of analysis should help us understand known spin liquids on the pyrochlore lattice better. Furthermore, one should be able to use it to find out more spin liquids — not relying on trial and error, but in a more systematic way. This is what we will achieve in the chapter.

To be more specific, we will realize a rank-2 U(1) spin liquid on the breathing pyrochlore lattice. Rank-2 U(1) gauge theories have recently been highlighted by its exotic forms of emergent electrodynamics [36, 79–81], where electric and magnetic fields have the form of rank–2 (or higher–rank) tensors.

The gauge sectors were initially proposed as a special version of Lifshitz gravity of $z = 2$ and $z = 3$ [134]. They have modified conservation laws and gauge symmetries inherited from the linearized version of diffeomorphism, resulting in some remarkable properties.

Later, the charged excitations dubbed "fractons" are studied in further detail. They have constrained mobility, and characterize a new class of "geometrical" order [34, 83–86, 217–221] beyond our conventional knowledge of topological order. Fracton models are also linked to quantum stabilizer codes [119, 222], holography [48], gravity/elasticity duality [100, 223].

None the less, these desirable properties come at a price: the local constraint required has a tensor character. As a consequence, prototypical models of fractons are based on complex, multiple-spin interactions [36, 83–86], with only a handful of proposals motivated by experiment [220, 224, 225]. In the case of gapless higher–rank gauge theories, only a few concrete models exist [80, 134, 226], and even less is known about how to achieve such a phase in a real material. For this reason, realizing an emergent higher–rank electrodynamics in experiment presents a significant challenge.

In this chapter, we show how the classical limit of a canonical rank–2 U(1) [R2–U1] spin liquid can arise naturally in a breathing pyrochlore magnet. We study the Heisenberg antiferromagnet (HAF) model on a breathing pyrochlore lattice, perturbed by weak Dzyaloshinskii–Moriya (DM) interactions [Fig. 6.1]. These interactions are relatively simple, and experimentally motivated. First we establish that low–energy fluctuations can be described using a matrix electric field satisfying the Gauss's laws required by a R2–U1 gauge theory. This is done using the analytical tools we developed.

We then use classical Monte Carlo simulation to confirm the theoretical analysis, and to examine how a R2–U1 spin liquid could be identified in experiment. We find that 4–fold pinch points (4FPP) singularities, a characteristic spin-spin correlation pattern of the R2–U1 state [227], become visible in polarised neutron scattering. In earlier works by Slagle, Gabor, You *et al.*, some experimentally oriented models with bilinear interactions to realize gapped, fracton topological orders were discussed. Our results complement them by providing an example of a gapless R2–U1 state, also in an experimentally–motivated context.

6.2 Rank–2 U(1) gauge theory

Here, following [36, 79], we review the relationship between electric, gauge and magnetic fields within the rank–2 U(1) [R2–U1] electrodynamics considered in this chapter. We first introduce the classical rank-2 electrostatics and its Gauss's laws that is realized in our work. We also discuss the quantum dynamics of the theory, which is beyond the scope of this model but nevertheless essential for future developments.

The starting point is an electric field described by a symmetric, traceless rank–2 tensor field,

$$E^{ij} = E^{ji}, \quad E^i_i = 0. \tag{6.1}$$

Here we do not distinguish super and subscript since we are dealing exclusively with spacial indices, and the Einstein summation rule is used on repeated indices.

The low energy sector of the electric field has vanishing vector charge,

$$\partial_i E^{ij} = 0. \tag{6.2}$$

Retrospectively, the reason that we choose the traceless, vector-charged version of R2-U1 is that the required spin-spin interactions for this case are particularly simple, making it an attractive model for experiments. Within this framework, it is also possible to realize the traceful version of vector-charged R2-U1, but the interactions required are more complicated. This approach so far does not support realization of scalar charged R2-U1, as the double derivatives only arise in our coarse-grained field theory analysis at higher order.

We will show, in this chapter, the proper rank-2 tensor with the corresponding Gauss's laws as a classical spin liquid system are achieved on a classical spin model.

A quantum spin liquid requires quantum dynamics in addition to the emergent Gauss's law. Broadly speaking, the dynamics play the role of $\mathbf{B}^2$ term in electrodynamics. They are to tunnel different classical spin liquid states between each other, leading to a long-range entangled quantum ground state and gapless photon excitations.

As in conventional electrodynamics, the conjugate of $\mathbf{E}$ is the rank-two gauge field $\mathbf{A}$, which also has to be symmetric in order to match the degrees of freedom,

$$A_{ij} = A_{ji}. \tag{6.3}$$

These traceless and charge-free conditions [Eqs. 6.1,6.2] determine the form of gauge transformation in the following way. Consider a state described by the wave-function

$$|\Psi(\mathbf{A})\rangle\,. \tag{6.4}$$

We take a low energy configuration of $\mathbf{E}$ obeying the Gauss's laws (Eqs. (6.1,6.2)) and construct a symmetrized operator that is equivalent to identity. The action of this

operator upon the state gives

$$\exp\left[-i(\lambda_i\partial_j E_{ij} + \lambda_j\partial_i E_{ij})\right]|\Psi(\mathbf{A})\rangle = |\Psi(\mathbf{A})\rangle\,. \tag{6.5}$$

Performing integration by parts and assuming vanishing boundary terms, we have also

$$\exp\left[i(\partial_i\lambda_j + \partial_j\lambda_i)E_{ij}\right]|\Psi(\mathbf{A})\rangle = |\Psi(\mathbf{A})\rangle\,. \tag{6.6}$$

Since E_{ij} conjugates with A_{ij}, it generates a transformation of $\mathbf{A}$. Thus we also have

$$\exp\left[i(\partial_i\lambda_j + \partial_j\lambda_i)E_{ij}\right]|\Psi(\mathbf{A})\rangle = |\Psi(\mathbf{A} + \boldsymbol{\nabla}\otimes\boldsymbol{\lambda} + (\boldsymbol{\nabla}\otimes\boldsymbol{\lambda})^T)\rangle\,. \tag{6.7}$$

That is, the charge-free wave function in the low energy sector is invariant under the gauge transformation

$$\mathbf{A} \to \mathbf{A} + \boldsymbol{\nabla}\otimes\boldsymbol{\lambda} + (\boldsymbol{\nabla}\otimes\boldsymbol{\lambda})^T, \quad \text{i.e.,} \quad A_{ij} \to A_{ij} + \partial_i\lambda_j + \partial_i\lambda_j. \tag{6.8}$$

Similarly, the traceless condition

$$\exp\left[-i\gamma\delta_{ij}E_{ij}\right]|\Psi(\mathbf{A})\rangle = 0. \tag{6.9}$$

can be used to derive to another gauge symmetry

$$A_{ij} \to A_{ij} + \gamma\delta_{ij}. \tag{6.10}$$

The magnetic field is obtained by finding the simplest gauge-invariant quantity by combing partial derivatives and the gauge fields, as explained in Sec. 1.4 of Chapter 1. In this case, it is found to have three derivatives acting on the gauge field, as we explained in Eq. (1.26):

$$\begin{aligned} B_{ij} =& \frac{1}{2}[\epsilon_{jab}(\partial_a\partial_k\partial_i A_{bk} - \partial_a\partial^2 A_{bi}) \\ &+ \epsilon_{iab}(\partial_a\partial_k\partial_j A_{bk} - \partial_a\partial^2 A_{bj})]. \end{aligned} \tag{6.11}$$

Finally, the Gauss's law, the traceless and symmetric conditions of the electric field can be used to derive the charge and multipole conservation laws:

$$\int dv\,\vec{\rho} = 0 \tag{6.12}$$

$$\int dv\,\vec{x}\times\vec{\rho} = -\int dv\,\epsilon_{ijk}E_{jk} = 0 \tag{6.13}$$

$$\int dv\,\vec{x}\cdot\vec{\rho} = -\int dv\,E_{ii} = 0 \tag{6.14}$$

$$\int dv\left[(\vec{x}\cdot\vec{\rho})\vec{x} - \frac{1}{2}x^2\vec{\rho}\right] = 0 \tag{6.15}$$

In this case, a vector charge excitation is fully fractonic, i.e., the Gauss's laws forbid any dynamics that moves the vector charge in the bulk. This comes from the second and third equations, in which both the "dipole" and "angular momentum" of the vector charge is conserved.

More details of the theory of R2–U1 phases are discussed in detail in Refs. [79, 81]. The quantum dynamics are not realized in our model.

6.3 Rank 2 U(1) Gauss's law on the breathing pyrochlore model

6.3.1 The breathing pyrochlore model

Our goal is to find a classical spin model that realizes the electrostatic sector of the R2-U1 theory [Eqs. (6.1,6.2)] as its low-energy effective action. The analytical approach of this work closely follows Refs. [178, 181, 228].

Here, we consider a spin system on a breathing pyrochlore lattice. "Breathing" means the A– and B–sublattice tetrahedra have different sizes, and consequently the spins have different interactions [Fig. 6.1].

Breathing–pyrochlore magnets were first studied as a tractable limit of the pyrochlore HAF [229–232], but have since been realised in several families of materials [233–240], which motivates us to use this model. To date, most theoretical work has concentrated on spin-rotation $SU(2)$–invariant models [229–232, 241–243]. However, spin–orbit coupling can reduce the symmetry of the lattice, and permits anisotropic exchange [237, 238, 244, 245]. Here we will consider the effects of strong HAF interactions and weak DM interactions. The Hamiltonian is

$$\begin{aligned}\mathcal{H} = &\sum_{\langle ij\rangle\in \mathrm{A}} \left[J_A \mathbf{S}_i\cdot\mathbf{S}_j + D_A \hat{\mathbf{d}}_{ij}\cdot(\mathbf{S}_i\times\mathbf{S}_j)\right] \\ &+ \sum_{\langle ij\rangle\in \mathrm{B}} \left[J_B \mathbf{S}_i\cdot\mathbf{S}_j + D_B \hat{\mathbf{d}}_{ij}\cdot(\mathbf{S}_i\times\mathbf{S}_j)\right] ,\end{aligned} \tag{6.16}$$

where $\langle ij\rangle \in$ A(B) denotes nearest neightbour bonds belonging to the A(B)-tetrahedra. The sites 0, 1, 2, 3 are at positions relative to the center of an A-tetrahedron

$$\mathbf{r}_0 = \frac{a}{8}(1,1,1),\ \mathbf{r}_1 = \frac{a}{8}(1,-1,-1),\ \mathbf{r}_2 = \frac{a}{8}(-1,1,-1),\ \mathbf{r}_3 = \frac{a}{8}(-1,-1,1), \tag{6.17}$$

where a is the length of the unit cell. Vectors $\hat{\mathbf{d}}_{ij}$ are bond dependent, defined in accordance with Ref [237, 246, 247]:

$$\begin{aligned}\hat{\mathbf{d}}_{01} &= \frac{(0,-1,1)}{\sqrt{2}},\ \hat{\mathbf{d}}_{02} = \frac{(1,0,-1)}{\sqrt{2}},\ \hat{\mathbf{d}}_{03} = \frac{(-1,1,0)}{\sqrt{2}}, \\ \hat{\mathbf{d}}_{12} &= \frac{(-1,-1,0)}{\sqrt{2}},\ \hat{\mathbf{d}}_{13} = \frac{(1,0,1)}{\sqrt{2}},\ \hat{\mathbf{d}}_{23} = \frac{(0,-1,-1)}{\sqrt{2}}.\end{aligned} \tag{6.18}$$

This model is experimentally motivated by Yb–based breathing pyrochlores, where experimental results and analysis suggest that the interactions on the A–tetrahedra are of exactly the form of Eq. (6.16), with $J_A > 0$, $D_A < 0$ [245]. And, while the form of interactions on the B–tetrahedra of these materials is currently unknown and negligible, we will see that as long as the anisotropic part of exchange is sufficiently

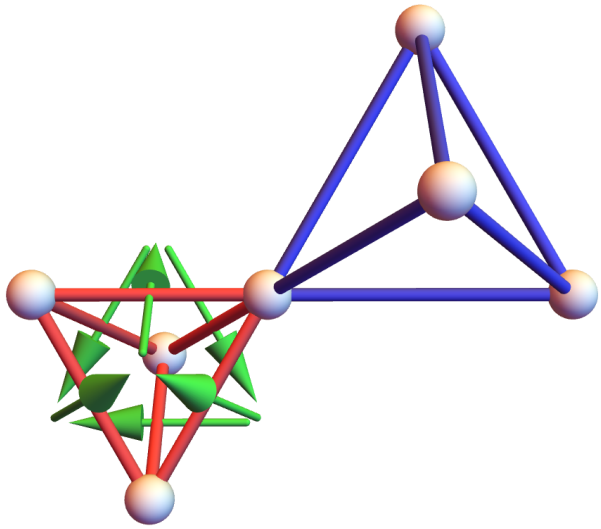

Figure 6.1: Breathing pyrochlore lattice of a magnet supporting a rank–2 U(1) [R2–U1] spin liquid. A– and B–sublattice tetrahedra are of unequal size, and have inequivalent exchange interactions. Vectors $\hat{\mathbf{d}}_{ij}$ associated with Dzyaloshinskii–Moriya (DM) interactions on the A–sublattice [Eq. (6.16)] are illustrated with green arrows . Figure reproduced from Ref. [180].

weak, this will give the conditions required to realize R2–U1 physics, which may be realized in similar compounds.

This model can be equivalently written in a standard matrix-exchange form we developed in the previous chapter. For a breathing-pyrochlore lattice model, it is

$$\mathcal{H} = \sum_{\langle ij \rangle \in \mathrm{A}} S_i^\alpha \mathcal{J}_{\mathrm{A,ij}}^{\alpha\beta} S_j^\beta + \sum_{\langle ij \rangle \in \mathrm{B}} S_i^\alpha \mathcal{J}_{\mathrm{B}}^{\alpha\beta} S_j^\beta, \tag{6.19}$$

where $\mathcal{J}_{\mathrm{A,ij}}$ is a three-by-three matrix that couples spins on sub-lattice sites i, j whose bond belongs to A-tetrahedra, and $\mathcal{J}_{\mathrm{B}}$ is the coupling matrix for B-tetrahedra. In the case of $D_B = 0$ that we are mostly interested in, $\mathcal{J}_{\mathrm{B}}$ is identical for any pair of i, j,

$$\mathcal{J}_{\mathrm{B}} = \begin{bmatrix} J_B & 0 & 0 \\ 0 & J_B & 0 \\ 0 & 0 & J_B \end{bmatrix}. \tag{6.20}$$

Matrices $\mathcal{J}_{\mathrm{A,ij}}$ are bond dependent and related to each other by the lattice symmetry.

Their explicit forms are

$$\mathcal{J}_{\mathrm{A},01} = \begin{bmatrix} J_A & D_A/\sqrt{2} & D_A/\sqrt{2} \\ -D_A/\sqrt{2} & J_A & 0 \\ -D_A/\sqrt{2} & 0 & J_A \end{bmatrix}, \ \mathcal{J}_{\mathrm{A},02} = \begin{bmatrix} J_A & -D_A/\sqrt{2} & 0 \\ D_A/\sqrt{2} & J_A & D_A/\sqrt{2} \\ 0 & -D_A/\sqrt{2} & J_A \end{bmatrix},$$
$$\mathcal{J}_{\mathrm{A},03} = \begin{bmatrix} J_A & 0 & -D_A/\sqrt{2} \\ 0 & J_A & -D_A/\sqrt{2} \\ D_A/\sqrt{2} & D_A/\sqrt{2} & J_A \end{bmatrix}, \ \mathcal{J}_{\mathrm{A},12} = \begin{bmatrix} J_A & 0 & D_A/\sqrt{2} \\ 0 & J_A & -D_A/\sqrt{2} \\ -D_A/\sqrt{2} & D_A/\sqrt{2} & J_A \end{bmatrix},$$
$$\mathcal{J}_{\mathrm{A},13} = \begin{bmatrix} J_A & D_A/\sqrt{2} & 0 \\ -D_A/\sqrt{2} & J_A & D_A/\sqrt{2} \\ 0 & -D_A/\sqrt{2} & J_A \end{bmatrix}, \ \mathcal{J}_{\mathrm{A},23} = \begin{bmatrix} J_A & -D_A/\sqrt{2} & D_A/\sqrt{2} \\ D_A/\sqrt{2} & J_A & 0 \\ -D_A/\sqrt{2} & 0 & J_A \end{bmatrix}. \tag{6.21}$$

As discussed in detail in previous chapter, the spin degrees of freedom on each tetrahedron can be rewritten in terms of fields forming the irreducible representations (irreps) of the lattice symmetry,

$$m_{\mathsf{A}_2}, \quad \mathbf{m}_{\mathsf{E}}, \quad \mathbf{m}_{\mathsf{T}_2}, \quad \mathbf{m}_{\mathsf{T}_{1+}}, \quad \mathbf{m}_{\mathsf{T}_{1-}}. \tag{6.22}$$

Their definitions can be found in Table 5.2. As linear combinations of the spin degrees of freedom, they leads to a fully diagonalized, quadratic Hamiltonian:

$$\mathcal{H} = \frac{1}{2}\sum_{\mathsf{X}} a_{\mathsf{X},\mathrm{A}} m^2_{\mathsf{X},\mathrm{A}} + \frac{1}{2}\sum_{\mathsf{X}} a_{\mathsf{X},\mathrm{B}} m^2_{\mathsf{X},\mathrm{B}}, \tag{6.23}$$

where X runs over irreps of the group T_d, i.e. $\{\mathsf{A}_2, \mathsf{E}, \mathsf{T}_2, \mathsf{T}_{1+}, \mathsf{T}_{1-}\}$ as listed in Eq. (6.22), and the subscript A,B denotes on which type of tetrahedra they are defined. We have on A-tetrahedra

$$a_{\mathsf{A}_2,\mathrm{A}} = -J_A - 4D_A/\sqrt{2}\,, \tag{6.24}$$
$$a_{\mathsf{T}_2,\mathrm{A}} = -J_A - 2D_A/\sqrt{2}\,, \tag{6.25}$$
$$a_{\mathsf{T}_{1+},\mathrm{A}} = 3J_A\,, \tag{6.26}$$
$$a_{\mathsf{T}_{1-},\mathrm{A}} = a_{\mathsf{E},\mathrm{A}} = -J_A + 2D_A/\sqrt{2}, \tag{6.27}$$

and on B-tetrahedra

$$a_{\mathsf{A}_2,\mathrm{B}} = a_{\mathsf{E},\mathrm{B}} = a_{\mathsf{T}_2,\mathrm{B}} = a_{\mathsf{T}_{1-},\mathrm{B}} = -J_B, \tag{6.28}$$
$$a_{\mathsf{T}_{1+},\mathrm{B}} = 3J_B. \tag{6.29}$$

6.3.2 The HAF point

Before considering the effect of DM interactions, it is helpful to understand how this approach works in the case of a known spin liquid: the HAF on a pyrochlore lattice [248–253]. By setting DM interactions to zero, leaving only HAF interactions finite,

$$J_A = J_B\,,\ D_A = D_B = 0\,, \tag{6.30}$$

we find the coupling coefficients are in order

$$0 < a_{\mathsf{A}_2} = a_{\mathsf{E}} = a_{\mathsf{T}_2} = a_{\mathsf{T}_{1-}} < a_{\mathsf{T}_{1+}} \,. \tag{6.31}$$

The degeneracy of a_{A_2}, a_{E}, a_{T_2}, $a_{\mathsf{T}_{1-}}$ reflects the fact that the HAF point is a highly fine-tuned point in the parameter space, where four different forms of order meet.

Because $a_{\mathsf{T}_{1+}}$ is the largest coefficient, excitation of $\mathbf{m}_{\mathsf{T}_{1+}}$ costs energy, while fluctuations of other irrep fields $\mathbf{m}_{\mathsf{X}\neq\mathsf{T}_{1+}}$ do not. Therefore on a single tetrahedron the ground states are those satisfying

- the fields $m_{\mathsf{A}_2}, \mathbf{m}_{\mathsf{E}}, \mathbf{m}_{\mathsf{T}_2}, \mathbf{m}_{\mathsf{T}_{1-}}$ are all free to fluctuate ;
- the field $\mathbf{m}_{\mathsf{T}_{1+}} = 0$.

We can conveniently merge all of the fluctuating fields into a rank–2 tensor

$$\mathbf{E}^{\mathsf{HAF}} = \mathbf{E}^{\mathsf{HAF}}_{\mathsf{sym.}} + \mathbf{E}^{\mathsf{HAF}}_{\mathsf{antisym.}} + \mathbf{E}^{\mathsf{HAF}}_{\mathsf{trace}} \tag{6.32}$$

where

$$\mathbf{E}^{\mathsf{HAF}}_{\mathsf{sym.}} = \begin{bmatrix} \frac{2}{\sqrt{3}} m^1_{\mathsf{E}} & m^z_{\mathsf{T}_{1-}} & m^y_{\mathsf{T}_{1-}} \\ m^z_{\mathsf{T}_{1-}} & -\frac{1}{\sqrt{3}} m^1_{\mathsf{E}} - m^2_{\mathsf{E}} & m^x_{\mathsf{T}_{1-}} \\ m^y_{\mathsf{T}_{1-}} & m^x_{\mathsf{T}_{1-}} & -\frac{1}{\sqrt{3}} m^1_{\mathsf{E}} + m^2_{\mathsf{E}} \end{bmatrix}, \tag{6.33}$$

$$(E^{\mathsf{HAF}}_{\mathsf{antisym.}})_{ij} = -\epsilon_{ijk} m^k_{\mathsf{T}_2}, \quad (E^{\mathsf{HAF}}_{\mathsf{trace}})_{ij} = -\delta_{ij}\sqrt{\frac{2}{3}} m_{\mathsf{A}_2}. \tag{6.34}$$

In matrix forms, Eq. (6.34) are written as

$$\mathbf{E}^{\mathsf{HAF}}_{\mathsf{antisym.}} = \begin{bmatrix} 0 & m^z_{\mathsf{T}_2} & -m^y_{\mathsf{T}_2} \\ -m^z_{\mathsf{T}_2} & 0 & m^x_{\mathsf{T}_2} \\ m^y_{\mathsf{T}_2} & -m^x_{\mathsf{T}_2} & 0 \end{bmatrix}, \tag{6.35}$$

$$\mathbf{E}^{\mathsf{HAF}}_{\mathsf{trace}} = \begin{bmatrix} -\sqrt{\frac{2}{3}} m_{\mathsf{A}_2} & 0 & 0 \\ 0 & -\sqrt{\frac{2}{3}} m_{\mathsf{A}_2} & 0 \\ 0 & 0 & -\sqrt{\frac{2}{3}} m_{\mathsf{A}_2} \end{bmatrix}. \tag{6.36}$$

And we have

$$\mathbf{E}^{\mathsf{HAF}} = \begin{bmatrix} \frac{2}{\sqrt{3}} m^1_{\mathsf{E}} - \sqrt{\frac{2}{3}} m_{\mathsf{A}_2} & m^z_{\mathsf{T}_{1,-}} + m^z_{\mathsf{T}_2} & m^y_{\mathsf{T}_{1,-}} - m^y_{\mathsf{T}_2} \\ m^z_{\mathsf{T}_{1,-}} - m^z_{\mathsf{T}_2} & -\frac{1}{\sqrt{3}} m^1_{\mathsf{E}} - m^2_{\mathsf{E}} - \sqrt{\frac{2}{3}} m_{\mathsf{A}_2} & m^x_{\mathsf{T}_{1,-}} + m^x_{\mathsf{T}_2} \\ m^y_{\mathsf{T}_{1,-}} + m^y_{\mathsf{T}_2} & m^x_{\mathsf{T}_{1,-}} - m^x_{\mathsf{T}_2} & -\frac{1}{\sqrt{3}} m^1_{\mathsf{E}} + m^2_{\mathsf{E}} - \sqrt{\frac{2}{3}} m_{\mathsf{A}_2} \end{bmatrix}, \tag{6.37}$$

which has all its 9 degrees of freedom.

Consider the pyrochlore lattice as connected tetrahedra, the requirement on one tetrahedron that

$$\mathbf{m}_{\mathsf{T}_{1+}} = 0 \tag{6.38}$$

imposes the conditions on the irreps on neighboring tetrahedra [181]. In this case, they are

$$\frac{2}{\sqrt{3}}\begin{bmatrix} \partial_x m^1_{\mathsf{E}} \\ -\frac{1}{2}\partial_y m^1_{\mathsf{E}} - \frac{\sqrt{3}}{2}\partial_y m^2_{\mathsf{E}} \\ -\frac{1}{2}\partial_y m^1_{\mathsf{E}} + \frac{\sqrt{3}}{2}\partial_y m^2_{\mathsf{E}} \end{bmatrix} - \begin{bmatrix} \partial_y m^z_{\mathsf{T}_{1-}} + \partial_z m^y_{\mathsf{T}_{1-}} \\ \partial_z m^x_{\mathsf{T}_{1-}} + \partial_x m^z_{\mathsf{T}_{1-}} \\ \partial_x m^y_{\mathsf{T}_{1-}} + \partial_y m^x_{\mathsf{T}_{1-}} \end{bmatrix}$$
$$-\sqrt{\frac{2}{3}}\boldsymbol{\nabla} m_{\mathsf{A}_2} + \boldsymbol{\nabla} \times \mathbf{m}_{\mathsf{T}_2} = 0\,. \tag{6.39}$$

Written in the matrix form we wrote down, these conditions are in an elegant form

$$\partial^i E^{\mathsf{HAF}}_{ij} = 0. \tag{6.40}$$

This system of equations can also be viewed as three independent copies of a U(1) gauge theory [252], one for each $j-$component,

Note that it is exactly the form of charge-free condition of the R2-U1 spin liquid in Eq. (6.2). However, the matrix electric field has the trace and anti-symmetric degrees of freedom activated, in contrast to the R2-U1 theory where the electric field matrix is symmetric and traceless.

6.3.3 From HAF to R2-U1

The Heisenberg antiferromagnet (HAF) point on a pyrochlore lattice hosts a spin liquid, but one described by a U(1)× U(1)×U(1) gauge theory [254]. These three copies of U(1) originate in the separate Gauss's laws for the three components of O(3) spins and, as noted by Henley [253]. The three conservation laws can be collected into a single rank–2 tensor field . The three independent Gauss's laws impose a condition of zero vector charge, Eq. (6.48), one of the requirements for a rank–2 U(1) theory. However they do not enforce the other requirement, that is, the tensor field must be symmetric and traceless, Eq. (6.49).

Let us emphasis the three different contributions to $\mathbf{E}^{\mathsf{HAF}}$ as

$$\mathbf{E}^{\mathsf{HAF}} = \mathbf{E}^{\mathsf{HAF}}_{\mathsf{sym.}} + \mathbf{E}^{\mathsf{HAF}}_{\mathsf{antisym.}} + \mathbf{E}^{\mathsf{HAF}}_{\mathsf{trace}} \tag{6.41}$$

The components of $\mathbf{E}^{\mathsf{HAF}}_{\mathsf{sym.}}$ are identical to the symmetric, traceless rank–2 electric field $\mathbf{E}$ found in the R2–U1 theory [Eq. (6.47)]. The components $\mathbf{E}^{\mathsf{HAF}}_{\mathsf{antisym.}}$ and $\mathbf{E}^{\mathsf{HAF}}_{\mathsf{trace}}$ are fluctuating for the HAF spin liquid but undesired for the R2-U1.

From Eqs. (6.36, 6.35), we notice that the origin of the finite antisymmetric part [Eq. (6.35)], and the finite trace [Eq. (6.36)], are the fluctuations of the irreps $\mathbf{m}_{\mathsf{T}_2}$ and m_{A_2}, respectively.

To convert the HAF into an R2–U1 spin liquid, we need to make the electric field symmetric and traceless to satisfy Eq. (6.1). This means suppressing fluctuations of $\mathbf{E}^{\mathsf{HAF}}_{\mathsf{antisym.}}$ and $\mathbf{E}^{\mathsf{HAF}}_{\mathsf{trace}}$ from the ground state. This can be accomplished by opening gaps to the fluctuations of irreps m_{T_2} and m_{A_2}.

For the breathing pyrochlore model, Eq. (6.16), this is achieved exactly by turning on the DM interactions of the appropriate form $D_A < D_B = 0$. It introduces an energy cost for the fluctuations of $\mathbf{m}_{\mathsf{T}_2}$ and m_{A_2}, and enforces the "missing" constraint, Eq. (6.49). This converts the $U(1) \times U(1) \times U(1)$ spin liquid of the HAF into the R2–U1 spin liquid of the breathing–pyrochlore model. The technical details will be shown in the next section.

6.3.4 R2-U1

For the breathing pyrochlore model, Eq. (6.16), we are interested in the parameter set

$$J_A\,,\ J_B > 0\,,\ D_A < 0\,,\ D_B = 0\,. \tag{6.42}$$

In this case the coefficients for the diagonalized Hamiltonian are in order

$$\text{on A-tetrahedra:} \qquad a_{\mathsf{E},\mathrm{A}} = a_{\mathsf{T}_{1-},\mathrm{A}} < a_{\mathsf{A}_2,\mathrm{A}},\ a_{\mathsf{T}_2,\mathrm{A}},\ a_{\mathsf{T}_{1+},\mathrm{A}}, \tag{6.43}$$

$$\text{on B-tetrahedra:} \qquad a_{\mathsf{A}_2,\mathrm{B}} = a_{\mathsf{E},\mathrm{B}} = a_{\mathsf{T}_2,\mathrm{B}} = a_{\mathsf{T}_{1-},\mathrm{B}} < a_{\mathsf{T}_{1+},\mathrm{B}}, \tag{6.44}$$

which play the central role of dictating the low energy physics.

The irrep fields are subject to a more complex set of constraints for ground states.

- On A-tetrahedra, the fields $\mathbf{m}_{\mathsf{E}}$ and $\mathbf{m}_{\mathsf{T}_{1-}}$ can fluctuate;
- On A-tetrahedra, the fields $\mathbf{m}_{\mathsf{T}_{1+}} = \mathbf{m}_{\mathsf{T}_2} = m_{\mathsf{A}_2} = 0$;
- On B-tetrahedra, the fields m_{A_2}, $\mathbf{m}_{\mathsf{E}}$, $\mathbf{m}_{\mathsf{T}_2}$, $\mathbf{m}_{\mathsf{T}_{1-}}$ can fluctuate;
- On B-tetrahedra,

$$\mathbf{m}_{\mathsf{T}_{1+}} = 0 \tag{6.45}$$

Since every spin is shared by an A- and a B-tetrahedron, the fluctuating fields $\mathbf{m}_{\mathsf{E}}$ and $\mathbf{m}_{\mathsf{T}_{1-}}$ on A-tetrahedra must obey additional constraints to respect the the low-energy sector condition on B-tetrahedron imposed by Eq. (6.45). Assuming slowly varying

fields in the continuous limit, $\mathbf{m}_{\mathsf{T}_{1,+}}$ on a B-tetrahedron can be expressed as a function of fields on the surrounding A-tetrahedra,

$$\begin{aligned}\mathbf{m}_{\mathsf{T}_{1,+}}(\mathbf{R}_B) =& \overline{\mathbf{m}}_{\mathsf{T}_{1,+}} + \frac{a_d}{\sqrt{6}}\nabla\times\mathbf{m}_{\mathsf{T}_2} - \frac{a_d}{3}\nabla m_{\mathsf{A}_2} \\ &+ \frac{\sqrt{2}a_d}{3}\begin{bmatrix}\partial_x m^1_{\mathsf{E}} \\ -\frac{1}{2}\partial_y m^1_{\mathsf{E}} - \frac{\sqrt{3}}{2}\partial_y m^2_{\mathsf{E}} \\ -\frac{1}{2}\partial_y m^1_{\mathsf{E}} + \frac{\sqrt{3}}{2}\partial_y m^2_{\mathsf{E}}\end{bmatrix} - \frac{a_d}{3\sqrt{2}}\begin{bmatrix}\partial_y m^z_{\mathsf{T}_{1,-}} + \partial_z m^y_{\mathsf{T}_{1,-}} \\ \partial_z m^x_{\mathsf{T}_{1,-}} + \partial_x m^z_{\mathsf{T}_{1,-}} \\ \partial_x m^y_{\mathsf{T}_{1,-}} + \partial_y m^x_{\mathsf{T}_{1,-}}\end{bmatrix},\end{aligned}$$

where $\overline{\mathbf{m}}_{\mathsf{T}_{1,+}}$ is the average of $\mathbf{m}_{\mathsf{T}_{1,+}}$ on the A-tetrahedra. Coming back to our case, since $\mathbf{m}_{\mathsf{T}_{1,+}}, \mathbf{m}_{\mathsf{T}_2}, m_{\mathsf{A}_2}$ are already zero on the A-tetrahedra, the constraint Eq. (6.45) can be expressed in terms of fields living on A-tetrahedra as [181],

$$\frac{2}{\sqrt{3}}\begin{bmatrix}\partial_x m^1_{\mathsf{E}} \\ -\frac{1}{2}\partial_y m^1_{\mathsf{E}} - \frac{\sqrt{3}}{2}\partial_y m^2_{\mathsf{E}} \\ -\frac{1}{2}\partial_y m^1_{\mathsf{E}} + \frac{\sqrt{3}}{2}\partial_y m^2_{\mathsf{E}}\end{bmatrix} - \begin{bmatrix}\partial_y m^z_{\mathsf{T}_{1-}} + \partial_z m^y_{\mathsf{T}_{1-}} \\ \partial_z m^x_{\mathsf{T}_{1-}} + \partial_x m^z_{\mathsf{T}_{1-}} \\ \partial_x m^y_{\mathsf{T}_{1-}} + \partial_y m^x_{\mathsf{T}_{1-}}\end{bmatrix} = 0. \tag{6.46}$$

From these constraints we can build the required symmetric, traceless, rank-two electric field E_{ij} as

$$E_{ij} = \begin{bmatrix}\frac{2}{\sqrt{3}}m^1_{\mathsf{E}} & m^z_{\mathsf{T}_{1-}} & m^y_{\mathsf{T}_{1-}} \\ m^z_{\mathsf{T}_{1-}} & -\frac{1}{\sqrt{3}}m^1_{\mathsf{E}} - m^2_{\mathsf{E}} & m^x_{\mathsf{T}_{1-}} \\ m^y_{\mathsf{T}_{1-}} & m^x_{\mathsf{T}_{1-}} & -\frac{1}{\sqrt{3}}m^1_{\mathsf{E}} + m^2_{\mathsf{E}}\end{bmatrix}, \tag{6.47}$$

which is exactly $\mathbf{E}^{\mathsf{HAF}}_{\mathsf{sym.}}$ [Eq. (6.33)] as we expected. Now Eq. (6.46) becomes

$$\partial_i E_{ij} = 0\,, \tag{6.48}$$

with symmetric and traceless conditions

$$E_{ji} = E_{ji}, \qquad E_{ii} = 0 \tag{6.49}$$

by the definition of E_{ij}.

Hence a rank-2, traceless, vector-charged magnetic field emerges at the low-energy sector from the microscopic model of Eq. (6.16), with exchange parameters from Eq. (6.42).

6.4 Experimental signatures

After constructing the model via analytical approach, we now turn to the question of how the R2–U1 spin liquid can be identified in simulation and experiment. Just as the zero–divergence condition in spin ice manifests itself in a pinch–point singularity [252], the constraints associated with an R2–U1 gauge theory dictate a characteristic singularity in correlations of the tensor electric field E_{ij} [227].

6.4.1 Four fold pinch points

Equation (6.49) constrains the form of correlations functions of $\langle E_{ij}(\mathbf{q})E_{kl}(-\mathbf{q})\rangle$, in the same spirit as how the two-in-two-out condition constrains the spin-spin correlation of spin ice. It is, however, in a more complicated form. Defining

$$S_{ijkl}(\mathbf{q}) \equiv \langle E_{ij}(\mathbf{q})E_{kl}(-\mathbf{q})\rangle, \tag{6.50}$$

it has to obey the constraints from all the Gauss's laws, i.e.,

$$\begin{aligned} S_{iikl}(\mathbf{q}) &= 0 \\ S_{ijkl}(\mathbf{q}) &= S_{jikl}(\mathbf{q}) \\ q^i S_{ijkl}(\mathbf{q}) &= 0 \end{aligned} \tag{6.51}$$

These constraints require that for small $\mathbf{q}$, the correlation function has to have the structure

$$\begin{aligned} \langle E_{ij}(\mathbf{q})E_{kl}(-\mathbf{q})\rangle \propto & \frac{1}{2}(\delta_{ik}\delta_{jl} + \delta_{il}\delta_{jk}) + \frac{q_i q_j q_k q_l}{q^4} \\ & - \frac{1}{2}\left(\delta_{ik}\frac{q_i q_l}{q^2} + \delta_{jk}\frac{q_i q_l}{q^2} + \delta_{il}\frac{q_j q_k}{q^2} + \delta_{jl}\frac{q_i q_k}{q^2}\right) \\ & - \frac{1}{2}\left(\delta_{ij} - \frac{q_i q_j}{q^2}\right)\left(\delta_{kl} - \frac{q_k q_l}{q^2}\right), \end{aligned} \tag{6.52}$$

which encodes a singularity at $\mathbf{q} \to 0$. Different choices of the components E_{ij} and E_{kl} have different patterns. A few representative ones are shown in Figs. 6.2,6.3.

The three–dimensional structure of the correlation $\langle E_{\mathrm{xy}}(\mathbf{q})E_{\mathrm{xy}}(-\mathbf{q})\rangle$ on a surface of fixed $|\mathbf{q}|$, is plotted in Fig. 6.2(a). In the $[0kl]$ plane, the correlations exhibit a conventional 2–fold pinch point, similar to what was found in spin ice [Fig. 6.2(b)]. However on the perpendicular $[hk0]$ plane, there is a 4–fold pinch point [Fig. 6.2(c)], which unambiguously distinguishes R2–U1 electrodynamics from conventional U(1) theories [227]. It is also observed in Fig. 6.3b,6.3c. It is the key signature to be looked for in experiments.

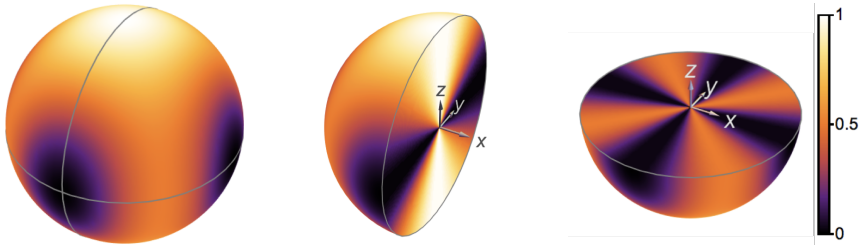

(a) (b) (c)

Figure 6.2: Structure of the 4–fold pinch point (4FPP) associated with rank–2 U(1) [R2–U1] gauge theory. (a) Prediction of R2–U1 theory for the correlation function $\langle E_{\rm xy}(\mathbf{q})E_{\rm xy}(-\mathbf{q})\rangle$, on a surface of fixed $|\mathbf{q}|$ near to a Brillouin zone center. (b) Exploded view, showing a 2–fold pinch point in the [0kl] plane. (c) Perpendicular cut, showing a 4FPP in the [hk0] plane.

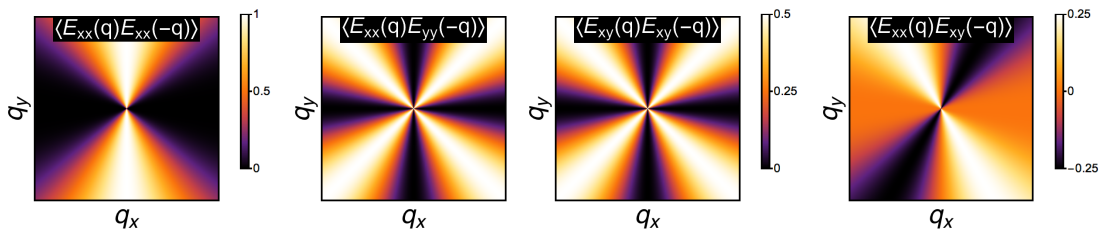

(a) (b) (c) (d)

Figure 6.3: Different components of correlation function $\langle E_{ij}(\mathbf{q})E_{kl}(-\mathbf{q})\rangle$ in $q_x - q_y$ plane, calculated from Eq. (6.52). Figure reproduced from Ref. [180].

Fig. 6.3b,6.3c have the four-fold pinch-point (4FPP) singularity, which differentiates the rank-2 gauge theories uniquely from the conventional U(1) gauge theory.

6.4.2 Neutron Scattering Results

We can use this singular feature as a test for the R2–U1 spin liquid in Monte Carlo simulation. We have carried out classical Monte Carlo simulations of Eq. (6.16), for the parameter–set

$$J_A = J_B = 1\ ,\ D_A = -0.01\ ,\ D_B = 0\ . \tag{6.53}$$

where the rank-2 U(1) physics is expected to be seen in the low energy limit. The resulting correlations of $\langle E_{xy}(\mathbf{q})E_{xy}(-\mathbf{q})\rangle$, at the temperature $T = 2.5 \times 10^{-3}\ J_A$, are shown in Fig. 6.4. For $\mathbf{q} \to 0$, they are identical to the predictions of Eq. (6.52), confirming that the model has realized an R2–U1 spin liquid.

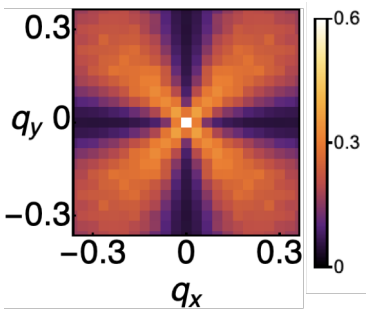

Figure 6.4: Correlation function $\langle E_{xy}(\mathbf{q})E_{xy}(-\mathbf{q})\rangle$ in $q_x - q_y$ plane, calculated from Monte-Carlo simulations. Figure reproduced from Ref. [180].

We now consider what this singularity will mean for experiments of neutron scattering. Neutron scattering does do not measure each component of correlations $\langle E_{ij}(\mathbf{q})E_{kl}(-\mathbf{q})\rangle$ directly, but rather the spin structure factor

$$S_{ij}^{\alpha\beta}(\mathbf{q}) = \langle S_i^\alpha(\mathbf{q})S_j^\beta(-\mathbf{q})\rangle \tag{6.54}$$

To be more exact, it measures the spin-spin correlation of the form

$$S(\mathbf{q}) = \sum_{\alpha,\beta,i,j}\left(\delta_{\alpha\beta} - \frac{q^\alpha q^\beta}{q^2}\right)\langle S_i^\alpha(\mathbf{q})S_j^\beta(-\mathbf{q})\rangle \tag{6.55}$$

where $\alpha,\beta = x,y,z$ are spin-component indices and $i,j = 0,1,2,3$ are sub-lattice site indices.

Furthermore, with neutrons polarized in direction of unit vector $\hat{\mathbf{v}}$ perpendicular to the scattering plane, one can measure the spin-flip (SF) channel neutron scattering defined by

$$S(\mathbf{q})_{\mathrm{SF}} = \sum_{\alpha,\beta,i,j}(v_\perp^\alpha v_\perp^\beta)\langle S_i^\alpha(\mathbf{q})S_j^\beta(-\mathbf{q})\rangle, \tag{6.56}$$

where

$$\hat{\mathbf{v}}_\perp = \frac{\hat{\mathbf{v}}\times\mathbf{q}}{|\hat{\mathbf{v}}\times\mathbf{q}|}. \tag{6.57}$$

Similarly one can also measure the non-spin-flip (NSF) channel defined by

$$S(\mathbf{q})_{\mathrm{NSF}} = \sum_{\alpha,\beta,i,j}(v^\alpha v^\beta)\langle S_i^\alpha(\mathbf{q})S_j^\beta(-\mathbf{q})\rangle \tag{6.58}$$

The structure factors $S(\mathbf{q})_{\mathrm{SF}}$ and $S(\mathbf{q})_{\mathrm{NSF}}$ measured by neutron scattering may inherit the four-fold pinch points. This is because they are measuring the spin-spin correlation $S_{ij}^{\alpha\beta}(\mathbf{q})$, which is in fact a certain linear combination of $\langle E_{ij}(\mathbf{q})E_{kl}(-\mathbf{q})\rangle$,

$$S_{mn}^{\alpha\beta}(\mathbf{q}) = \sum_{i,j,k,l} D_{mn\alpha\beta,ijkl}\langle E_{ij}(\mathbf{q})E_{kl}(-\mathbf{q})\rangle. \tag{6.59}$$

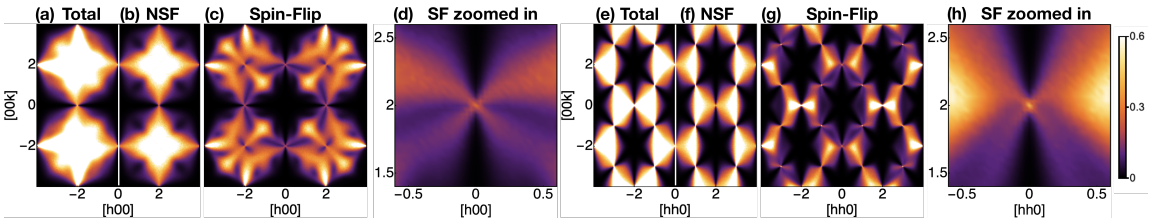

Figure 6.5: 4-Fold Pinch Points (4FPPs) in spin structure factor in the $[h0k]$ and $[hhk]$ plane of momentum space of the model [Eq. (6)] from MC simulations. The exchange parameters are from the idealized theoretical case $J_A = J_B = 1.0$, $D_A = -0.01$, $D_B = 0.0$, at $T = 2.5 \times 10^{-3}\ J_A$. (a) Total structure factor in $[h0k]$ plane. (b) Non-spin-flip (NSF) channel in $[h0k]$ plane. (c) Spin-flip (SF) channel in $[h0k]$ plane. (d) Enlarged 4FPP in $[h0k]$ plane. (a) Total structure factor in $[hhk]$ plane. (b) Non-spin-flip (NSF) channel in $[hhk]$ plane. (c) Spin-flip (SF) channel in $[hhk]$ plane. (d) Enlarged 4FPP in $[hhk]$ plane. The 4FPPs can be clearly observed in the SF channel, centered on [0, 0, 2] (and points related by symmetry), but weaker than in the $[h0k]$ plane. Figure reproduced from Ref. [180].

As some components of $\langle E_{ij}(\mathbf{q})E_{kl}(-\mathbf{q})\rangle$ contain the four-fold pinch points, they may present in $S(\mathbf{q})_{\mathrm{SF}}$ and $S(\mathbf{q})_{\mathrm{NSF}}$. The unspecified coefficients $D_{mn\alpha\beta,ijkl}$ can be calculated in principle. An example of this type of calculation, for the simpler case of spin ice, is discussed in Refs. [63, 181].

It is actually easier to calculate the inverse relation, that is, $\langle E_{ij}(\mathbf{q})E_{kl}(-\mathbf{q})\rangle$ as a linear combination of $S^{\alpha\beta}_{mn}(\mathbf{q})$,

$$\langle E_{ij}(\mathbf{q})E_{kl}(-\mathbf{q})\rangle = \sum_{m,n,\alpha,\beta} C_{ijkl,mn\alpha\beta} S^{\alpha\beta}_{mn}(\mathbf{q}). \tag{6.60}$$

The coefficients $C_{ijkl,mn\alpha\beta}$ can be calculated by noticing that each component of E_{ij} is defined in terms of m_{X} via Eq. (6.37), which is then written in terms of spin components S^{α}_{m} in Table 5.2. $D_{mn\alpha\beta,ijkl}$ is the inverse of $C_{ijkl,mn\alpha\beta}$.

To calculate every coefficient $C_{ijkl,mn\alpha\beta}$ is a lengthy exercise. For the purpose of demonstration, here we show an example of the calculation of $\langle E_{xy}(\mathbf{q})E_{xy}(-\mathbf{q})\rangle$ in the breathing-pyrochlore model considered in this chapter.

Note that

$$E_{xy} = m^{z}_{\mathrm{T}_{1-}} = \frac{-1}{2\sqrt{2}}(S^{x}_{0} + S^{y}_{0} - S^{x}_{1} + S^{y}_{1} + S^{x}_{2} - S^{y}_{2} - S^{x}_{3} - S^{y}_{3}), \tag{6.61}$$

we have

$$
\begin{aligned}
\langle E_{xy}(\mathbf{q})E_{xy}(-\mathbf{q})\rangle =& \langle m^z_{\mathrm{T}_{1-}}(\mathbf{q})m^z_{\mathrm{T}_{1-}}(-\mathbf{q})\rangle \\
=& \frac{1}{8}\langle \left[S^x_0 + S^y_0 - S^x_1 + S^y_1 + S^x_2 - S^y_2 - S^x_3 - S^y_3\right](\mathbf{q}) \\
& \qquad \left[S^x_0 + S^y_0 - S^x_1 + S^y_1 + S^x_2 - S^y_2 - S^x_3 - S^y_3\right](-\mathbf{q})\rangle \\
=& \frac{1}{8}(S^{xx}_{00}(\mathbf{q}) + S^{xy}_{00}(\mathbf{q}) - S^{xx}_{01}(\mathbf{q}) + S^{xy}_{01}(\mathbf{q}) + S^{xx}_{02}(\mathbf{q}) - S^{xy}_{02}(\mathbf{q}) \\
& - S^{xx}_{03}(\mathbf{q}) - S^{xy}_{03}(\mathbf{q}) + 56 \text{ terms}) \\
=& \sum_{m,n,\alpha,\beta} C_{xyxy,mn\alpha\beta} S^{\alpha\beta}_{mn}(\mathbf{q}).
\end{aligned}
\tag{6.62}
$$

Here, $C_{xyxy,mn\alpha\beta}$ can be written in a compact form as

$$
C_{xyxy,mn\alpha\beta} = Z^{\alpha}_{m} Z^{\beta}_{n}, \tag{6.63}
$$

where Z^{α}_{m} is defined as

$$
Z^{\alpha}_{m} = \begin{bmatrix} 1 & 1 & 0 \\ -1 & 1 & 0 \\ 1 & -1 & 0 \\ -1 & -1 & 0 \end{bmatrix}. \tag{6.64}
$$

Here the rows correspond to $m = 0, 1, 2, 3$ and the columns correspond to $\alpha = x, y, z$. Other components of $C_{ijkl,mn\alpha\beta}$ can be obtained following the same recipe, and then $D_{mn\alpha\beta,ijkl}$ can be derived as its inverse.

The spin-spin correlations are expected to show the 4FPP singularity in Eq. (6.52). But exactly how 4FPPs would manifest themselves in experiment remains to be confirmed numerically. Therefore, in Fig. 6.5 we present simulation results for $S^{\alpha\beta}(\mathbf{q})$ for the parameter set of Eq. (6.53). We find that the 4FPP is *not* observed in the structure factor from unpolarised neutron scattering; However, it *can* is revealed in polarised neutrons scattering. In this case, it manifests itself in the spin–flip (SF) channel for neutrons polarised perpendicular to the scattering plane [255] as shown in Figs. 6.5(b,d,g,h)]. In particular, the 4FPP is most pronounced in the $[hk0]$ plane.

6.4.3 Phase diagram

We then explored the phase diagram of the model. We simulated a range of values of D_A and temperatures T, and collected the results in Fig. 6.6. At finite temperature, a finite value of $D_A < 0$ is required to achieve a crossover from the U(1)×U(1)×U(1) spin liquid of the pyrochlore HAF, with only 2–fold pinch points, into an R2–U1 spin liquid, with 4FPP. Meanwhile, at low temperatures, sufficiently negative values of D_A drive a first–order phase transition into an ordered state with a characteristic wavevector $\mathbf{q} = \mathbf{W}$ (i.e. corners of the Brillouin zone). However, a more complex, multiple–$\mathbf{q}$ ground state is hard to rule out categorically, because of the difficulty of thermalisation at the lowest temperatures. In contrast, a finite value of $D_A > 0$ leads to a continuous phase transition into a state with $\mathbf{q} = 0$, all–out (AIAO) order.

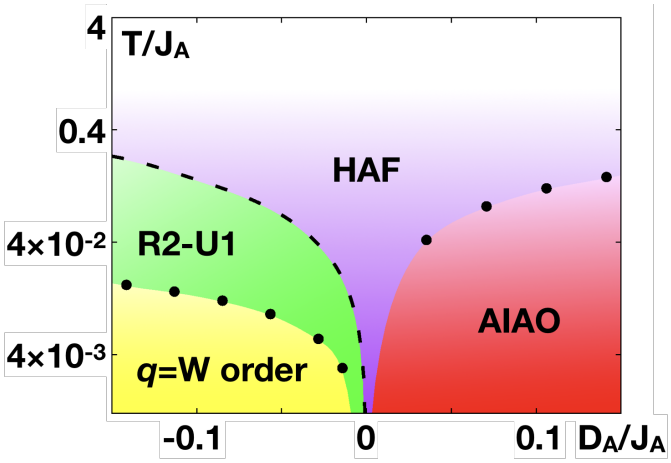

Figure 6.6: Finite–temperature phase diagram of breathing pyrochlore lattice model as a function of Dzyaloshinskii–Moriya (DM) interaction D_A, showing relationship between rank–2 U(1) spin liquid (R2–U1) [green shaded region], and the $U(1) \times U(1) \times U(1)$ spin liquid associated with the Heisenberg antiferromagnet (HAF) [purple shaded region]. The crossover from the HAF into the R2–U1 spin liquid is shown with a dashed line. The solid line indicates a continuous transition into all–in all–out order (AIAO), while the double line denotes a first order phase transition into a complex ordered state with $\mathbf{q} = W$. Results are taken from Monte Carlo simulation of Eq. (6.16) for $J_A = J_B = 1$, $D_B = 0$. Figure reproduced from Ref. [180].

6.5 Application to materials.

Breathing–pyrochlore magnetism find material realization is a number of transition–metals [233, 234, 236, 239, 240] , rare–earth ions [235, 238]., and also lacunar spinels [256, 257]. Here "breathing" refers to the feature that the two types of tetrahedra in the lattice have different sizes [Fig. 6.1]. This type of distortion of the pyrochlore lattice is termed "breathing", as it is a static limit of breathing phonon modes. As a consequence of their different sizes and associated changes in bond angles, the two types of tetrahedra will have different interactions. And, with respect to our model for the higher–rank gauge theories, a promising class of candidates are Yb–based materials, where the required exchanges appear to dominate.

One concrete example is $Ba_3Yb_2Zn_5O_{11}$ [235, 237, 238, 245], where A–tetrahedra are estimated to have the coupling parameters $J_A \approx 0.57$ meV, $D_A \approx -0.16$ meV, with other interactions negligible. This is *exactly* the type of interactions required for an R2–U1 spin liquid in our model, It is expected to be robust [245], since it holds for a wide range of Slater–Koster overlap ratios [258]. Meanwhile, exchange interactions on the much larger B–tetrahedra of $Ba_3Yb_2Zn_5O_{11}$, while less well understood, appear to be orders of magnitude smaller [237, 238], hence negligible. Thus, while it seems plausible that $Ba_3Yb_2Zn_5O_{11}$ could realise a R2–U1 spin liquid, this will occur at temperatures too low to measure. Nevertheless, it is likely that a similar compound can have a smaller B–tetrahedra with the desired HAF interactions, and realize the R2-U1 we analyzed in

this Chapter.

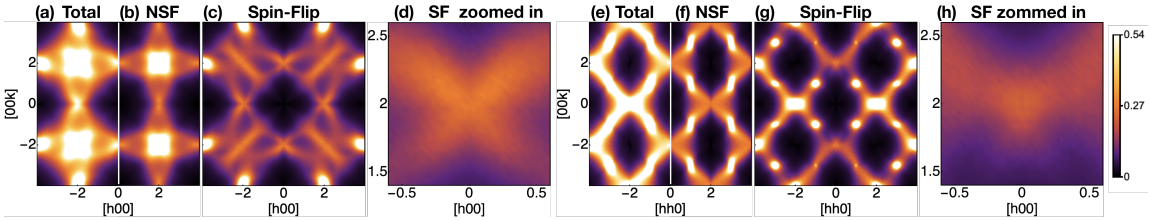

Figure 6.7: Spin structure factor found in classical Monte Carlo simulation of the breathing pyrochlore lattice model Eq. (6.16), showing 4–fold pinch points (4FPPs) characteristic of a rank–2 U(1) [R2–U1] spin liquid. The exchange parameters are from the experimental case Eq. (6.65) at $T = 252$ mK. (a) Total structure factor in $[h0k]$ plane. (b) Non-spin-flip (NSF) channel in $[h0k]$ plane. (c) Spin-flip (SF) channel in $[h0k]$ plane. (d) Enlarged 4FPP in $[h0k]$ plane. (a) Total structure factor in $[hhk]$ plane. (b) Non-spin-flip (NSF) channel in $[hhk]$ plane. (c) Spin-flip (SF) channel in $[hhk]$ plane. (d) Enlarged 4FPP in $[hhk]$ plane. The 4FPPs can be observed in the SF channel, centered on [0, 0, 2] (and points related by symmetry), but weaker than in the $[h0k]$ plane. Figure reproduced from Ref. [180].

The encouraging example of $Ba_3Yb_2Zn_5O_{11}$ motivates us to consider the possibility of materials with similar structures, but smaller B–tetrahedra, such that the interactions on the B–sublattice become non–negligible. For concreteness, we consider the parameter set:

$$\begin{aligned} J_A &= 0.57 \text{ meV}, \; J_B = 0.028 \text{ meV} \,, \\ D_A &= -0.16 \text{ meV}, \; D_B = -0.007 \text{ meV} \,, \end{aligned} \tag{6.65}$$

where we assume that the interactions on the B–sublattice are of the same type as on the A–sublattice, but substantially weaker, $J_A/J_B = D_A/D_B \approx 20$. The difference from the ideal case is a finite D_B here. To demonstrate that the R2–U1 physics persists in the presence of finite D_B, we have used MC simulation to calculate the spin structure factor. Once again, the 4FPP associated with the R2–U1 spin liquid remains visible for a range of temperatures [Fig. 6.7].

The same will hold for a more general choice of interactions, as long as the anisotropic part of the exchange on the B–sublattice is sufficiently weak.

6.6 Summary

In this chapter, we have used a combination of analytic field theory and classical Monte Carlo simulation techniques to show how a rank–2 U(1) [R2–U1] spin liquid, a system described by a higher–rank generalisation of electrodynamics, can arise in a

pyrochlore magnet with breathing anisotropy (i.e., one where the two types of tetrahedra have different sizes and therefore different interactions) and Heisenberg antiferromagnetic and Dzyaloshinskii–Moriya interactions [Fig. 6.1]. These results provide a concrete, realistic starting point for the experimental search for higher–rank gauge theories, which support fracton excitations. They also clarify the type of neutron scattering experiment needed to resolve the 4–fold pinch points (4FPP) of such a R2–U1 spin liquid.

This work opens a number of interesting perspectives. On the experimental side, we identify Yb based breathing–pyrochlore materials as potential candidates for a R2–U1 spin liquid state. In particular, the material $Ba_3Yb_2Zn_5O_{11}$already has interactions very close to the desired case. On the theoretical side, determining the quantum ground state of Eq. (6.16) is an interesting question. It should ultimately prove tractable, since breathing anisotropy provides a natural control parameter for both perturbative [230, 231] and variational approaches [259].

Finally, the theoretical framework of partial–confinement mechanism used to eliminate selected components of the tensorial electric field is very versatile, and easily adapted to generate other versions of R2–U1 theory or gapped fracton matters.

Chapter 7

Conclusion and Outlook

Modern physics has entered an exciting era of intertwined influences between quantum many-body systems, quantum gravity, and quantum information. The interdisciplinary study of these topics is an enchanting long term program to which I hope to devote my effort. This thesis is my contribution to this theme. It is the initial step to understand the connection between fracton states of matter and gravity, and also explores concrete routes to realize such exotic states in experiments.

7.1 Fracton states of matter and holography

It is well-established that gauge theories can emerge as collective phenomena in many-body systems. However, much less is known about how they can mimic gravity, except for some early works on building graviton-like gauge bosons. On the other hand, the developments in holography and AdS/CFT have taught us that the informational properties constitute another profound side of gravity. As practitioners of the idea "emergence," it is natural to ask: what kind of many-body systems captures such physics?

In Chapters 2,3, we studied a very simple classical fracton model on the hyperbolic lattice. We showed that it satisfies a few major informational properties of gravity in the context of holography. These properties include the correspondence between the boundary entanglement and the bulk geometry, the boundary-bulk reconstruction rule, and the micro-states encoding of black holes. Furthermore, we reveal that the hyperbolic fracton model is equivalent to a fixed distribution to bit threads.

In Chapter 4, we push our understanding from the toy models to the field theory. We reason that since all local dynamics of rank-2 U(1) theory do not respect gauge invariance, the simplest viable dynamics object are electric field lines on the geodesics. Their gauge invariance is due to the vector charge's mobility in the direction it points at. We argue that this geodesics string condensation picture is exactly the continuous limit of the bit-thread picture. In this sense, the leading order perturbative limit of general

relativity, i.e., the rank-2 U(1) gauge theory, gives rise to the leading order approximation to its holographic entanglement structure. At this level, the investigation is fairly complete.

Along this direction, there are still several profound problems to solve.

First, these advances imply a unifying picture of several different holographic toy models from bit-thread/tensor-network/fracton constructions. The discovery of fracton toy models provides the bulk theory to explain all of them: the Lifshitz gravity or rank-2 U(1) gauge theory. Our preliminary theoretical considerations show that the geodesic bit-threads emerge at the low energy sector of the Lifshitz gravity. It is interesting to ask if such results can be pushed further than the leading order and help us understand the holographic entanglement deeper.

In addition, so far all the fracton models, including those on a flat lattice, relies on the procedure of foliation [96, 101, 113, 260]. In the two-dimensional models we discussed, the geodesics must be well-defined in the lattice structure to induce bit-threads. It is curious to ask if there can actually be any fracton models defined on more generic lattices/graphs like toric code or conventional lattice gauge theory in general.

Also, how to describe fracton states of matter in terms of field theory is an intriguing topic. Various observations suggest that examining gravitational theories with symmetry breaking and foliation preserving diffeomorphism is a promising direction [95]. In particular, the consequences of the latter case are much under-explored. They may give rise to new zoology of "geometric orders," including the fracton topological orders and perhaps many more unexpected.

Finally, we can gain insight into the origin of the entanglement structure of gravity by comparing the gapless fracton states and the full-fledged general relativity. For example, information scrambling seems to be closely related to the Ryu-Takayanagi entanglement entropy formula for a disconnected boundary subregion, which is not the case for the fracton theory [17]. Hence it is interesting to ask which effect in gravity makes the scrambling happen. Besides, I will explore if the fracton models can inspire new concrete examples of AdS/CFT correspondence.

7.2 Experimental Routes toward fracton states of matter

Coming from fantasies back to realities, a crucial progress in the field of fractons is still missing: its experimental realization. The gapless rank-2 U(1) theories were originally proposed as effective theories of spin liquid/boson liquid [36]. Therefore we would like to look for its spin liquid realization.

This is in particular difficult for fracton states of matter, since the prototype models often require complicated interactions between more than two degrees of freedom. Hence it is a non-trivial task to find out experimentally more realistic routes to realize

them. These routes not only provide guidelines for experimentalists, but may also deepen our understanding of the physics of fractons.

Along this line, in Chapters 5,6 we have constructed a relatively simple frustrated spin model on breathing pyrochlore lattice, and shown that its low energy effective physics is the classical section of rank-2 U(1) gauge theory.

In Chapter 5, we performed the symmetry analysis for the spin systems on a tetrahedron and the pyrochlore lattice. The irreducible representation fields is very useful in determining the ground states in different phases, and also finding out the enlarged ground state manifolds on the phase boundary. Such analysis is already useful in understanding the properties of several materials.

In Chapter 6, we apply the tool developed on the breathing pyrochlore lattice, and show that the enlarged ground state manifold is exactly that of the classical sector of the rank-2 U(1) spin liquid. The advantage of this model is that it is experimentally highly realistic, and has already some materials with part of the desired interactions. This study also highlights the generic recipe of partial confining several copies of conventional U(1) gauge theory to obtain rank-2 U(1) gauge theory.

There are many future problems for us to consider.

First, the model proposed in this thesis is classical. Its generalization to a quantum model is not so straightforward. If one simply promote the classical spins to quantum spin half operators, than the different components of the electric tensor do not commute, hence one cannot simply introduce the dynamics section to the model. It is thus an interesting question to ask what is the nature of the quantum model, and if it is possible to refine it to introduce proper quantum dynamics.

Second, models based on other types of systems also have potential to bear rank-2 U(1) physics. A known example is the elasticity-fracton duality [100, 261]. In fact, it inspires us to think that any physical objects that has a tensorial nature can be a candidate to build fracton states of matter. Such considerations motivate us to think of nematic states of matter, and also higher spin frustrated models, which share essentially the same mathematical framework.

We hope, in collaboration with experimentalists, fracton states of matter can be realized in laboratory in the near future. Theoretically, they are novel quantum phases beyond our conventional wisdom, and also some of them can be viewed as laboratory toy model of gravity. Practically, they have great potential in quantum computation. The laboratory creation of fracton matters will be ground breaking for both science and technology.

Bibliography

[1] S. Weinberg, in *General Relativity: An Einstein centenary survey*, edited by S. W. Hawking and W. Israel (1979) pp. 790–831.

[2] G. Hooft, Nucl. Phys. B **72**, 461 (1974).

[3] L. Susskind, J. Math. Phys. **36**, 6377 (1995).

[4] J. Maldacena, Int. J. Theor. Phys. **38**, 1113 (1999).

[5] E. Witten, Adv. Theor. Math. Phys. **2**, 253 (1998).

[6] S. S. Gubser, I. R. Klebanov, and A. M. Polyakov, Phys. Lett. B **428**, 105 (1998).

[7] O. Aharony, S. S. Gubser, J. Maldacena, H. Ooguri, and Y. Oz, Phys. Rep. **323**, 183 (2000).

[8] O. Aharony, O. Bergman, D. L. Jafferis, and J. Maldacena, JHEP **2008** (10), 091.

[9] I. Klebanov and A. Polyakov, Phys. Lett. B **550**, 213 (2002).

[10] S. W. Hawking, Phys. Rev. D **72**, 084013 (2005).

[11] M. Guica, T. Hartman, W. Song, and A. Strominger, Phys. Rev. D **80**, 124008 (2009).

[12] B. Swingle, Phys. Rev. D **86**, 065007 (2012).

[13] F. Pastawski, B. Yoshida, D. Harlow, and J. Preskill, JHEP **2015** (6), 149.

[14] A. Almheiri, X. Dong, and D. Harlow, JHEP **2015** (4), 163.

[15] Z. Yang, P. Hayden, and X.-L. Qi, JHEP **2016** (1), 175.

[16] P. Hayden, S. Nezami, X.-L. Qi, N. Thomas, M. Walter, and Z. Yang, JHEP **2016** (11), 9.

[17] P. Hayden, S. Nezami, X.-L. Qi, N. Thomas, M. Walter, and Z. Yang, arXiv:1801.05289 [hep-th] .

[18] D. Harlow, Communications in Mathematical Physics **354**, 865 (2017).

[19] M. Freedman and M. Headrick, Communications in Mathematical Physics **352**, 407 (2017).

[20] M. Headrick and V. E. Hubeny, Classical and Quantum Gravity **35**, 105012 (2018).

[21] C.-B. Chen, F.-W. Shu, and M.-H. Wu, arXiv:1804.00441 [hep-th] .

[22] S. Ryu and T. Takayanagi, JHEP **2006** (08), 045.

[23] S. Ryu and T. Takayanagi, Phys. Rev. Lett. **96**, 181602 (2006).

[24] J. M. Kosterlitz and D. J. Thouless, Journal of Physics C: Solid State Physics **6**, 1181 (1973).

[25] X. Chen, Z.-C. Gu, and X.-G. Wen, Phys. Rev. B **82**, 155138 (2010).

[26] C. Chamon, Phys. Rev. Lett. **94**, 040402 (2005).

[27] B. Yoshida, Phys. Rev. B **88**, 125122 (2013).

[28] S. Bravyi, B. Leemhuis, and B. M. Terhal, Annals of Physics **326**, 839 (2011).

[29] J. Haah, Phys. Rev. A **83**, 042330 (2011).

[30] S. Vijay, J. Haah, and L. Fu, Phys. Rev. B **92**, 235136 (2015).

[31] S. Vijay, J. Haah, and L. Fu, Phys. Rev. B **94**, 235157 (2016).

[32] M. Pretko, Phys. Rev. B **96**, 035119 (2017).

[33] M. Pretko, Phys. Rev. B **95**, 115139 (2017).

[34] R. M. Nandkishore and M. Hermele, Annual Review of Condensed Matter Physics **10**, 295 (2019).

[35] M. Pretko, Phys. Rev. D **96**, 024051 (2017).

[36] C. Xu, Phys. Rev. B **74**, 224433 (2006).

[37] C. Xu and P. Hořava, Phys. Rev. D **81**, 104033 (2010).

[38] P. Anderson, Materials Research Bulletin **8**, 153 (1973).

[39] L. Balents, Nature **464**, 199 (2010).

[40] L. Savary and L. Balents, Reports on Progress in Physics **80**, 016502 (2017).

[41] Y. Zhou, K. Kanoda, and T.-K. Ng, Rev. Mod. Phys. **89**, 025003 (2017).

[42] J. Polchinski, arXiv:1010.6134 [hep-th] .

[43] H. Nastase, arXiv:0712.0689 [hep-th] .

[44] I. R. Klebanov, *Strings, Branes, and Gravity TASI 99*, edited by J. A. Harvey, S. Kachru, and E. Silverstein (World Scientific, Singapore, 2001) pp. 615–650.

[45] J. M. Maldacena, arXiv:hep-th/0309246 .

[46] J. D. Bekenstein, Phys. Rev. D **7**, 2333 (1973).

[47] S. W. Hawking, Commun. Math. Phys. **43**, 199 (1975).

[48] H. Yan, Phys. Rev. B **99**, 155126 (2019).

[49] L. D. L. E. Lifshitz, *Statistical Physics*, 3rd ed., Vol. 5 (Elsevier, 2013).

[50] X. G. Wen, International Journal of Modern Physics B **04**, 239 (1990).

[51] A. Kitaev and C. Laumann, arXiv:0904.2771 [cond-mat.mes-hall] .

[52] H. D. Zhou, C. R. Wiebe, J. A. Janik, L. Balicas, Y. J. Yo, Y. Qiu, J. R. D. Copley, and J. S. Gardner, Phys. Rev. Lett. **101**, 227204 (2008).

[53] K. A. Ross, L. Savary, B. D. Gaulin, and L. Balents, Phys. Rev. X **1**, 021002 (2011).

[54] T. Fennell, M. Kenzelmann, B. Roessli, M. K. Haas, and R. J. Cava, Phys. Rev. Lett. **109**, 017201 (2012).

[55] K. Kimura, S. Nakatsuji, J.-J. Wen, C. Broholm, M. B. Stone, E. Nishibori, and H. Sawa, Nature Communications **4**, 1934 (2013).

[56] R. Sibille, E. Lhotel, V. Pomjakushin, C. Baines, T. Fennell, and M. Kenzelmann, Phys. Rev. Lett. **115**, 097202 (2015).

[57] J.-J. Wen, S. M. Koohpayeh, K. A. Ross, B. A. Trump, T. M. McQueen, K. Kimura, S. Nakatsuji, Y. Qiu, D. M. Pajerowski, J. R. D. Copley, and C. L. Broholm, Phys. Rev. Lett. **118**, 107206 (2017).

[58] J. D. Thompson, P. A. McClarty, D. Prabhakaran, I. Cabrera, T. Guidi, and R. Coldea, Phys. Rev. Lett. **119**, 057203 (2017).

[59] R. Sibille, N. Gauthier, H. Yan, M. Ciomaga Hatnean, J. Ollivier, B. Winn, U. Filges, G. Balakrishnan, M. Kenzelmann, N. Shannon, and T. Fennell, Nature Physics **14**, 711715 (2018).

[60] B. Gao, T. Chen, D. W. Tam, C.-L. Huang, K. Sasmal, D. T. Adroja, F. Ye, H. Cao, G. Sala, M. B. Stone, C. Baines, J. A. T. Verezhak, H. Hu, J.-H. Chung, X. Xu, S.-W. Cheong, M. Nallaiyan, S. Spagna, M. B. Maple, A. H. Nevidomskyy, E. Morosan, G. Chen, and P. Dai, Nature Physics **15**, 1052 (2019).

[61] M. Hermele, M. P. A. Fisher, and L. Balents, Phys. Rev. B **69**, 064404 (2004).

[62] A. Banerjee, S. V. Isakov, K. Damle, and Y. B. Kim, Phys. Rev. Lett. **100**, 047208 (2008).

[63] O. Benton, O. Sikora, and N. Shannon, Phys. Rev. B **86**, 075154 (2012).

[64] L. Savary and L. Balents, Phys. Rev. Lett. **108**, 037202 (2012).

[65] N. Shannon, O. Sikora, F. Pollmann, K. Penc, and P. Fulde, Phys. Rev. Lett. **108**, 067204 (2012).

[66] Z. Hao, A. G. R. Day, and M. J. P. Gingras, Phys. Rev. B **90**, 214430 (2014).

[67] M. J. P. Gingras and P. A. McClarty, Reports on Progress in Physics **77**, 056501 (2014).

[68] Y. Kato and S. Onoda, Phys. Rev. Lett. **115**, 077202 (2015).

[69] G. Chen, Phys. Rev. B **96**, 195127 (2017).

[70] C.-J. Huang, Y. Deng, Y. Wan, and Z. Y. Meng, Phys. Rev. Lett. **120**, 167202 (2018).

[71] L. Pauling, J. Am. Chem. Soc. **57**, 2680 (1935).

[72] C. L. Henley, Phys. Rev. B **80**, 180401 (2009).

[73] L. D. C. Jaubert and P. C. W. Holdsworth, Nature Physics **5**, 258 (2009).

[74] D. S. Rokhsar and S. A. Kivelson, Phys. Rev. Lett. **61**, 2376 (1988).

[75] M. Hermele, M. P. A. Fisher, and L. Balents, Phys. Rev. B **69**, 064404 (2004).

[76] F. J. Wegner, Journal of Mathematical Physics **12**, 2259 (1971).

[77] J. B. Kogut, Rev. Mod. Phys. **51**, 659 (1979).

[78] P. A. M. Dirac, Proc. Roy. Soc. Lond. **A133**, 60 (1931).

[79] M. Pretko, Phys. Rev. B **96**, 035119 (2017).

[80] A. Rasmussen, Y.-Z. You, and C. Xu, arXiv:1601.08235 [cond-mat.str-el] .

[81] M. Pretko, Phys. Rev. B **95**, 115139 (2017).

[82] C. Xu and P. Hořava, Phys. Rev. D **81**, 104033 (2010).

[83] C. Chamon, Phys. Rev. Lett. **94**, 040402 (2005).

[84] J. Haah, Phys. Rev. A **83**, 042330 (2011).

[85] S. Vijay, J. Haah, and L. Fu, Phys. Rev. B **92**, 235136 (2015).

[86] S. Vijay, J. Haah, and L. Fu, Phys. Rev. B **94**, 235157 (2016).

[87] D. Bulmash and M. Barkeshli, Phys. Rev. B **97**, 235112 (2018).

[88] H. Ma, M. Hermele, and X. Chen, Phys. Rev. B **98**, 035111 (2018).

[89] S. Hartnoll, A. Lucas, and S. Sachdev, *Holographic quantum matter* (The MIT Press, Cambridge, 2016).

[90] R. Bousso, Rev. Mod. Phys. **74**, 825 (2002).

[91] X.-L. Qi, arXiv:1309.6282 [hep-th] .

[92] Y. Gu, C. H. Lee, X. Wen, G. Y. Cho, S. Ryu, and X.-L. Qi, Phys. Rev. B **94**, 125107 (2016).

[93] C. H. Lee and X.-L. Qi, Phys. Rev. B **93**, 035112 (2016).

[94] G. B. Halász, T. H. Hsieh, and L. Balents, Phys. Rev. Lett. **119**, 257202 (2017).

[95] W. Shirley, K. Slagle, Z. Wang, and X. Chen, Phys. Rev. X **8**, 031051 (2018).

[96] W. Shirley, K. Slagle, and X. Chen, SciPost Phys. **6**, 15 (2019).

[97] A. T. Schmitz, H. Ma, R. M. Nandkishore, and S. A. Parameswaran, Phys. Rev. B **97**, 134426 (2018).

[98] H. Ma, E. Lake, X. Chen, and M. Hermele, Phys. Rev. B **95**, 245126 (2017).

[99] H. Ma, A. T. Schmitz, S. A. Parameswaran, M. Hermele, and R. M. Nandkishore, Phys. Rev. B **97**, 125101 (2018).

[100] M. Pretko and L. Radzihovsky, Phys. Rev. Lett. **120**, 195301 (2018).

[101] W. Shirley, K. Slagle, and X. Chen, SciPost Phys. **6**, 41 (2019).

[102] T. Devakul, D. J. Williamson, and Y. You, Phys. Rev. B **98**, 235121 (2018).

[103] Y. You, T. Devakul, F. J. Burnell, and S. L. Sondhi, Phys. Rev. B **98**, 035112 (2018).

[104] R. L. Jack, L. Berthier, and J. P. Garrahan, Phys. Rev. E **72**, 016103 (2005).

[105] J. P. Garrahan and M. E. J. Newman, Phys. Rev. E **62**, 7670 (2000).

[106] R. Baxter, *Exactly Solved Models in Statistical Mechanics*, Dover books on physics (Dover Publications, 2007).

[107] G. K. Savvidy and F. J. Wegner, Nuclear Physics B **413**, 605 (1994).

[108] G. K. Savvidy and K. G. Savvidy, Modern Physics Letters A **11**, 1379 (1996).

[109] R. Pietig and F. J. Wegner, Nuclear Physics B **525**, 549 (1998).

[110] G. 't Hooft, arXiv:gr-qc/9310026 [gr-qc] .

[111] M. Leclerc, arXiv:gr-qc/0612125 [gr-qc] .

[112] A. Rasmussen and A. S. Jermyn, Phys. Rev. B **97**, 165141 (2018).

[113] K. Slagle, D. Aasen, and D. Williamson, SciPost Phys. **6**, 43 (2019).

[114] K. Slagle, A. Prem, and M. Pretko, arXiv:1807.00827 [cond-mat.str-el] .

[115] K. Slagle and Y. B. Kim, Phys. Rev. B **97**, 165106 (2018).

[116] H. Yan, D. Williamson, and Z.-X. Luo, Preprint in preparation.

[117] X. Dong, Nature Communications **7**, 12472 (2016).

[118] T. Faulkner, A. Lewkowycz, and J. Maldacena, JHEP **2013**, 74.

[119] A. Kubica and B. Yoshida, arXiv:1805.01836 [quant-ph] .

[120] H. He, Y. Zheng, B. A. Bernevig, and N. Regnault, Phys. Rev. B **97**, 125102 (2018).

[121] A. Gromov, Phys. Rev. Lett. **122**, 076403 (2019).

[122] M. Van Raamsdonk, arXiv:0907.2939 [hep-th] .

[123] S. X. Cui, P. Hayden, T. He, M. Headrick, B. Stoica, and M. Walter, arXiv:1808.05234 [hep-th] .

[124] J. Harper, M. Headrick, and A. Rolph, arXiv:1807.04294 [hep-th] .

[125] N. Bao and H. Ooguri, Phys. Rev. D **96**, 066017 (2017).

[126] M. Pretko and L. Radzihovsky, Phys. Rev. Lett. **121**, 235301 (2018).

[127] B. Sutherland, Journal of Mathematical Physics **11**, 3183 (1970).

[128] C. Fan and F. Y. Wu, Phys. Rev. B **2**, 723 (1970).

[129] R. J. Baxter, Phys. Rev. Lett. **26**, 832 (1971).

[130] L. P. Kadanoff and F. J. Wegner, Phys. Rev. B **4**, 3989 (1971).

[131] H. Yan, Phys. Rev. B **100**, 245138 (2019).

[132] A. J. Beekman, J. Nissinen, K. Wu, K. Liu, R.-J. Slager, Z. Nussinov, V. Cvetkovic, and J. Zaanen, Physics Reports **683**, 1 (2017).

[133] Q. Wen, Phys. Rev. D **98**, 106004 (2018).

[134] C. Xu and P. Hořava, Phys. Rev. D **81**, 104033 (2010).

[135] A. Jahn, M. Gluza, F. Pastawski, and J. Eisert, arXiv:1905.03268 [hep-th] .

[136] H. Yan, (2019), arXiv:1911.01007 [cond-mat.str-el] .

[137] A. Jahn, M. Gluza, F. Pastawski, and J. Eisert, Science Advances **5**, 8 (2019).

[138] X. Dong, D. Harlow, and A. C. Wall, Phys. Rev. Lett. **117**, 021601 (2016).

[139] X. Dong, Nature Communications **7**, 12472 (2016).

[140] P. Hořava, Phys. Rev. D **79**, 084008 (2009).

[141] T. P. Sotiriou, Journal of Physics: Conference Series **283**, 012034 (2011).

[142] M. A. Levin and X.-G. Wen, Phys. Rev. B **71**, 045110 (2005).

[143] M. Levin and X.-G. Wen, Phys. Rev. Lett. **96**, 110405 (2006).

[144] A. Kitaev and J. Preskill, Phys. Rev. Lett. **96**, 110404 (2006).

[145] M. Pretko and T. Senthil, Phys. Rev. B **94**, 125112 (2016).

[146] C. Castelnovo, R. Moessner, and S. Sondhi, Annual Review of Condensed Matter Physics **3**, 35 (2012).

[147] A. Banerjee, S. V. Isakov, K. Damle, and Y. B. Kim, Phys. Rev. Lett. **100**, 047208 (2008).

[148] L. Savary and L. Balents, Phys. Rev. Lett. **108**, 037202 (2012).

[149] N. Shannon, O. Sikora, F. Pollmann, K. Penc, and P. Fulde, Phys. Rev. Lett. **108**, 067204 (2012).

[150] S. B. Lee, S. Onoda, and L. Balents, Phys. Rev. B **86**, 104412 (2012).

[151] O. Benton, O. Sikora, and N. Shannon, Phys. Rev. B **86**, 075154 (2012).

[152] L. Savary and L. Balents, Phys. Rev. B **87**, 205130 (2013).

[153] M. J. P. Gingras and P. A. McClarty, Reports on Progress in Physics **77**, 056501 (2014).

[154] L. Pan, S. K. Kim, A. Ghosh, C. M. Morris, K. A. Ross, E. Kermarrec, B. D. Gaulin, S. M. Koohpayeh, O. Tchernyshyov, and N. P. Armitage, Nature Communications **5**, 4970 (2014).

[155] L. Pan, N. J. Laurita, K. A. Ross, B. D. Gaulin, and N. P. Armitage, Nature Physics **12**, 361 (2016).

[156] Y. Tokiwa, T. Yamashita, M. Udagawa, S. Kittaka, T. Sakakibara, D. Terazawa, Y. Shimoyama, T. Terashima, Y. Yasui, T. Shibauchi, and Y. Matsuda, Nature Communications **7**, 10807 (2016).

[157] M. J. Harris, S. T. Bramwell, D. F. McMorrow, T. Zeiske, and K. W. Godfrey, Phys. Rev. Lett. **79**, 2554 (1997).

[158] R. Moessner, Phys. Rev. B **57**, R5587 (1998).

[159] J. S. Gardner, M. J. P. Gingras, and J. E. Greedan, Rev. Mod. Phys. **82**, 53 (2010).

[160] G.-W. Chern, SPIN **05**, 1540006 (2015).

[161] K. A. Ross, J. P. C. Ruff, C. P. Adams, J. S. Gardner, H. A. Dabkowska, Y. Qiu, J. R. D. Copley, and B. D. Gaulin, Phys. Rev. Lett. **103**, 227202 (2009).

[162] K. A. Ross, L. R. Yaraskavitch, M. Laver, J. S. Gardner, J. A. Quilliam, S. Meng, J. B. Kycia, D. K. Singh, T. Proffen, H. A. Dabkowska, and B. D. Gaulin, Phys. Rev. B **84**, 174442 (2011).

[163] J. D. Thompson, P. A. McClarty, H. M. Rønnow, L. P. Regnault, A. Sorge, and M. J. P. Gingras, Phys. Rev. Lett. **106**, 187202 (2011).

[164] L.-J. Chang, S. Onoda, Y. Su, Y.-J. Kao, K.-D. Tsuei, Y. Yasui, K. Kakurai, and M. R. Lees, Nature Communications **3**, 992 (2012).

[165] J. D. M. Champion, M. J. Harris, P. C. W. Holdsworth, A. S. Wills, G. Balakrishnan, S. T. Bramwell, E. Čižmár, T. Fennell, J. S. Gardner, J. Lago, D. F. McMorrow, M. Orendáč, A. Orendáčová, D. M. Paul, R. I. Smith, M. T. F. Telling, and A. Wildes, Phys. Rev. B **68**, 020401 (2003).

[166] L. Savary, K. A. Ross, B. D. Gaulin, J. P. C. Ruff, and L. Balents, Phys. Rev. Lett. **109**, 167201 (2012).

[167] M. E. Zhitomirsky, M. V. Gvozdikova, P. C. W. Holdsworth, and R. Moessner, Phys. Rev. Lett. **109**, 077204 (2012).

[168] J. Oitmaa, R. R. P. Singh, B. Javanparast, A. G. R. Day, B. V. Bagheri, and M. J. P. Gingras, Phys. Rev. B **88**, 220404 (2013).

[169] J. G. Rau, S. Petit, and M. J. P. Gingras, Phys. Rev. B **93**, 184408 (2016).

[170] K. Matsuhira, Y. Hinatsu, K. Tenya, H. Amitsuka, and T. Sakakibara, Journal of the Physical Society of Japan **71**, 1576 (2002).

[171] S. Guitteny, S. Petit, E. Lhotel, J. Robert, P. Bonville, A. Forget, and I. Mirebeau, Phys. Rev. B **88**, 134408 (2013).

[172] R. Sibille, N. Gauthier, H. Yan, M. Ciomaga Hatnean, J. Ollivier, B. Winn, U. Filges, G. Balakrishnan, M. Kenzelmann, N. Shannon, and et al., Nature Physics **14**, 711–715 (2018).

[173] Z. L. Dun, E. S. Choi, H. D. Zhou, A. M. Hallas, H. J. Silverstein, Y. Qiu, J. R. D. Copley, J. S. Gardner, and C. R. Wiebe, Phys. Rev. B **87**, 134408 (2013).

[174] A. Yaouanc, P. Dalmas de Réotier, P. Bonville, J. A. Hodges, V. Glazkov, L. Keller, V. Sikolenko, M. Bartkowiak, A. Amato, C. Baines, P. J. C. King, P. C. M. Gubbens, and A. Forget, Phys. Rev. Lett. **110**, 127207 (2013).

[175] X. Li, W. M. Li, K. Matsubayashi, Y. Sato, C. Q. Jin, Y. Uwatoko, T. Kawae, A. M. Hallas, C. R. Wiebe, A. M. Arevalo-Lopez, J. P. Attfield, J. S. Gardner, R. S. Freitas, H. D. Zhou, and J.-G. Cheng, Phys. Rev. B **89**, 064409 (2014).

[176] Z. L. Dun, X. Li, R. S. Freitas, E. Arrighi, C. R. Dela Cruz, M. Lee, E. S. Choi, H. B. Cao, H. J. Silverstein, C. R. Wiebe, J. G. Cheng, and H. D. Zhou, Phys. Rev. B **92**, 140407 (2015).

[177] Y. Q. Cai, Q. Cui, X. Li, Z. L. Dun, J. Ma, C. dela Cruz, Y. Y. Jiao, J. Liao, P. J. Sun, Y. Q. Li, J. S. Zhou, J. B. Goodenough, H. D. Zhou, and J.-G. Cheng, Phys. Rev. B **93**, 014443 (2016).

[178] O. Benton, L. D. C. Jaubert, H. Yan, and N. Shannon, Nature Communications **7**, 11572 (2016).

[179] M. Taillefumier, O. Benton, H. Yan, L. D. C. Jaubert, and N. Shannon, Phys. Rev. X **7**, 041057 (2017).

[180] H. Yan, O. Benton, L. D. C. Jaubert, and N. Shannon, Phys. Rev. Lett. **124**, 127203 (2020).

[181] O. Benton, *Classical and quantum spin liquids on the pyrochlore lattice*, Ph.D. thesis, University of Bristol (2015).

[182] H. Cao, A. Gukasov, I. Mirebeau, P. Bonville, C. Decorse, and G. Dhalenne, Phys. Rev. Lett. **103**, 056402 (2009).

[183] S. Onoda and Y. Tanaka, Phys. Rev. B **83**, 094411 (2011).

[184] J. G. Rau and M. J. P. Gingras, Phys. Rev. B **92**, 144417 (2015).

[185] Y.-P. Huang, G. Chen, and M. Hermele, Phys. Rev. Lett. **112**, 167203 (2014).

[186] Y.-D. Li and G. Chen, Phys. Rev. B **95**, 041106 (2017).

[187] H. R. Molavian, M. J. P. Gingras, and B. Canals, Phys. Rev. Lett. **98**, 157204 (2007).

[188] H. Yan, O. Benton, L. Jaubert, and N. Shannon, Phys. Rev. B **95**, 094422 (2017).

[189] S. H. Curnoe, Phys. Rev. B **75**, 212404 (2007).

[190] K. A. Ross, L. Savary, B. D. Gaulin, and L. Balents, Phys. Rev. X **1**, 021002 (2011).

[191] A. W. C. Wong, Z. Hao, and M. J. P. Gingras, Phys. Rev. B **88**, 144402 (2013).

[192] A. Poole, A. S. Wills, and E. Lelièvre-Berna, Journal of Physics Condensed Matter **19**, 452201 (2007).

[193] O. Kovalev, *Representations of the Crystallographic Space Groups* (Gordon and Breach Science Publishers, Switzerland, 1993).

[194] G. D. M. S. Dresselhaus and A. Jorio, *Group Theory: Application to the Physics of Condensed Matter* (Springer-Verlag, Berlin, 2010).

[195] Y. Yasui, M. Soda, S. Iikubo, M. Ito, M. Sato, N. Hamaguchi, T. Matsushita, N. Wada, T. Takeuchi, N. Aso, and K. Kakurai, Journal of the Physical Society of Japan **72**, 3014 (2003).

[196] L.-J. Chang, M. R. Lees, I. Watanabe, A. D. Hillier, Y. Yasui, and S. Onoda, Phys. Rev. B **89**, 184416 (2014).

[197] E. Lhotel, S. R. Giblin, M. R. Lees, G. Balakrishnan, L. J. Chang, and Y. Yasui, Phys. Rev. B **89**, 224419 (2014).

[198] L. D. C. Jaubert, O. Benton, J. G. Rau, J. Oitmaa, R. R. P. Singh, N. Shannon, and M. J. P. Gingras, Phys. Rev. Lett. **115**, 267208 (2015).

[199] J. Robert, E. Lhotel, G. Remenyi, S. Sahling, I. Mirebeau, C. Decorse, B. Canals, and S. Petit, Phys. Rev. B **92**, 064425 (2015).

[200] J. Gaudet, K. A. Ross, E. Kermarrec, N. P. Butch, G. Ehlers, H. A. Dabkowska, and B. D. Gaulin, Phys. Rev. B **93**, 064406 (2016).

[201] A. M. Hallas, J. Gaudet, N. P. Butch, M. Tachibana, R. S. Freitas, G. M. Luke, C. R. Wiebe, and B. D. Gaulin, Phys. Rev. B **93**, 100403 (2016).

[202] A. Yaouanc, P. Dalmas de Réotier, L. Keller, B. Roessli, and A. Forget, Journal of Physics Condensed Matter **28**, 426002 (2016).

[203] I. Mirebeau, A. Apetrei, J. Rodríguez-Carvajal, P. Bonville, A. Forget, D. Colson, V. Glazkov, J. P. Sanchez, O. Isnard, and E. Suard, Phys. Rev. Lett. **94**, 246402 (2005).

[204] S. Petit, P. Bonville, I. Mirebeau, H. Mutka, and J. Robert, Phys. Rev. B **85**, 054428 (2012).

[205] M. E. Zhitomirsky, P. C. W. Holdsworth, and R. Moessner, Phys. Rev. B **89**, 140403 (2014).

[206] V. S. Maryasin and M. E. Zhitomirsky, Phys. Rev. B **90**, 094412 (2014).

[207] A. Andreanov and P. A. McClarty, Phys. Rev. B **91**, 064401 (2015).

[208] G.-W. Chern, arXiv:1008.3038 [cond-mat.str-el] .

[209] B. Javanparast, A. G. R. Day, Z. Hao, and M. J. P. Gingras, Phys. Rev. B **91**, 174424 (2015).

[210] S. E. Palmer and J. T. Chalker, Phys. Rev. B **62**, 488 (2000).

[211] P. A. McClarty, P. Stasiak, and M. J. P. Gingras, Phys. Rev. B **89**, 024425 (2014).

[212] B. Canals, M. Elhajal, and C. Lacroix, Phys. Rev. B **78**, 214431 (2008).

[213] E. Lhotel, S. Petit, S. Guitteny, O. Florea, M. Ciomaga Hatnean, C. Colin, E. Ressouche, M. R. Lees, and G. Balakrishnan, Phys. Rev. Lett. **115**, 197202 (2015).

[214] R. Applegate, N. R. Hayre, R. R. P. Singh, T. Lin, A. G. R. Day, and M. J. P. Gingras, Phys. Rev. Lett. **109**, 097205 (2012).

[215] N. R. Hayre, K. A. Ross, R. Applegate, T. Lin, R. R. P. Singh, B. D. Gaulin, and M. J. P. Gingras, Phys. Rev. B **87**, 184423 (2013).

[216] P. Bonville, S. Petit, I. Mirebeau, J. Robert, E. Lhotel, and C. Paulsen, Journal of Physics: Condensed Matter **25**, 275601 (2013).

[217] N. Shannon, G. Misguich, and K. Penc, Phys. Rev. B **69**, 220403(R) (2004).

[218] D. Bulmash and M. Barkeshli, Phys. Rev. B **97**, 235112 (2018).

[219] H. Ma, M. Hermele, and X. Chen, Phys. Rev. B **98**, 035111 (2018).

[220] K. Slagle and Y. B. Kim, Phys. Rev. B **96**, 165106 (2017).

[221] G. B. Halász, T. H. Hsieh, and L. Balents, Phys. Rev. Lett. **119**, 257202 (2017).

[222] A. T. Schmitz, H. Ma, R. M. Nandkishore, and S. A. Parameswaran, Phys. Rev. B **97**, 134426 (2018).

[223] A. Gromov, Phys. Rev. Lett. **122**, 076403 (2019).

[224] G. B. Halász, T. H. Hsieh, and L. Balents, Phys. Rev. Lett. **119**, 257202 (2017).

[225] Y. You and F. von Oppen, arXiv:1812.06091 [cond-mat.str-el] .

[226] C. Xu and M. P. A. Fisher, Phys. Rev. B **75**, 104428 (2007).

[227] A. Prem, S. Vijay, Y.-Z. Chou, M. Pretko, and R. M. Nandkishore, Phys. Rev. B **98**, 165140 (2018).

[228] H. Yan, O. Benton, L. Jaubert, and N. Shannon, Phys. Rev. B **95**, 094422 (2017).

[229] A. Harris, A. Berlinsky, and B. C., J. Appl. Phys. **69**, 5200 (1991).

[230] B. Canals and C. Lacroix, Phys. Rev. Lett. **80**, 2933 (1998).

[231] B. Canals and C. Lacroix, Phys. Rev. B **61**, 1149 (2000).

[232] H. Tsunetsugu, Journal of the Physical Society of Japan **70**, 640 (2001).

[233] Y. Okamoto, G. J. Nilsen, J. P. Attfield, and Z. Hiroi, Phys. Rev. Lett. **110**, 097203 (2013).

[234] Y. Tanaka, M. Yoshida, M. Takigawa, Y. Okamoto, and Z. Hiroi, Phys. Rev. Lett. **113**, 227204 (2014).

[235] K. Kimura, S. Nakatsuji, and T. Kimura, Phys. Rev. B **90**, 060414(R) (2014).

[236] G. J. Nilsen, Y. Okamoto, T. Masuda, J. Rodriguez-Carvajal, H. Mutka, T. Hansen, and Z. Hiroi, Phys. Rev. B **91**, 174435 (2015).

[237] J. G. Rau, L. S. Wu, A. F. May, L. Poudel, B. Winn, V. O. Garlea, A. Huq, P. Whitfield, A. E. Taylor, M. D. Lumsden, M. J. P. Gingras, and A. D. Christianson, Phys. Rev. Lett. **116**, 257204 (2016).

[238] T. Haku, K. Kimura, Y. Matsumoto, M. Soda, M. Sera, D. Yu, R. A. Mole, T. Takeuchi, S. Nakatsuji, Y. Kono, T. Sakakibara, L.-J. Chang, and T. Masuda, Phys. Rev. B **93**, 220407(R) (2016).

[239] R. Wawrzyńczak, Y. Tanaka, M. Yoshida, Y. Okamoto, P. Manuel, N. Casati, Z. Hiroi, M. Takigawa, and G. J. Nilsen, Phys. Rev. Lett. **119**, 087201 (2017).

[240] Y. Okamoto, M. Mori, N. Katayama, A. Miyake, M. Tokunaga, A. Matsuo, K. Kindo, and K. Takenaka, Journal of the Physical Society of Japan **87**, 034709 (2018).

[241] O. Benton and N. Shannon, Journal of the Physical Society of Japan **84**, 104710 (2015).

[242] F.-Y. Li, Y.-D. Li, Y. B. Kim, L. Balents, Y. Yu, and G. Chen, Nature Communications **7**, 12691 EP (2016).

[243] K. Essafi, L. D. C. Jaubert, and M. Udagawa, J. Phys. Condens. Matter **29**, 315802 (2017).

[244] L. Savary, X. Wang, H.-Y. Kee, Y. B. Kim, Y. Yu, and G. Chen, Phys. Rev. B **94**, 075146 (2016).

[245] J. G. Rau and M. J. P. Gingras, Phys. Rev. B **98**, 054408 (2018).

[246] V. N. Kotov, M. Elhajal, M. E. Zhitomirsky, and F. Mila, Phys. Rev. B **72**, 014421 (2005).

[247] B. Canals, M. Elhajal, and C. Lacroix, Phys. Rev. B **78**, 214431 (2008).

[248] P. W. Anderson, Phys. Rev. **102**, 1008 (1956).

[249] J. N. Reimers, A. J. Berlinsky, and A.-C. Shi, Phys. Rev. B **43**, 865 (1991).

[250] R. Moessner and J. T. Chalker, Phys. Rev. Lett. **80**, 2929 (1998).

[251] R. Moessner and J. T. Chalker, Phys. Rev. B **58**, 12049 (1998).

[252] C. L. Henley, Phys. Rev. B **71**, 014424 (2005).

[253] C. L. Henley, Annual Review of Condensed Matter Physics **1**, 179 (2010).

[254] S. V. Isakov, K. Gregor, R. Moessner, and S. L. Sondhi, Phys. Rev. Lett. **93**, 167204 (2004).

[255] T. Fennell, P. P. Deen, A. R. Wildes, K. Schmalzl, D. Prabakharan, A. T. Boothroyd, R. J. Aldus, D. F. McMorrow, and S. T. Bramwell, Science **326**, 415 (2009).

[256] S. Widmann, A. Günther, E. Ruff, V. Tsurkan, H.-A. Krug von Nidda, P. Lunkenheimer, and A. Loidl, Phys. Rev. B **94**, 214421 (2016).

[257] M. Y. Jeong, S. H. Chang, B. H. Kim, J.-H. Sim, A. Said, D. Casa, T. Gog, E. Janod, L. Cario, S. Yunoki, M. J. Han, and J. Kim, Nature Communications **8**, 782 (2017).

[258] J. C. Slater and G. F. Koster, Phys. Rev. **94**, 1498 (1954).

[259] O. Benton, L. D. C. Jaubert, R. R. P. Singh, J. Oitmaa, and N. Shannon, Phys. Rev. Lett. **121**, 067201 (2018).

[260] T. Wang, W. Shirley, and X. Chen, arXiv:1904.01111 [cond-mat.str-el] .

[261] A. Gromov, Phys. Rev. Lett. **122**, 076403 (2019).